



Systematic analysis of long-period earthquakes : Gorely volcano, Kamchatka

Sergei Abramenkov

► To cite this version:

Sergei Abramenkov. Systematic analysis of long-period earthquakes : Gorely volcano, Kamchatka. Earth Sciences. Université Paris Cité, 2021. English. NNT : 2021UNIP7002 . tel-03788405

HAL Id: tel-03788405

<https://theses.hal.science/tel-03788405>

Submitted on 26 Sep 2022

HAL is a multi-disciplinary open access archive for the deposit and dissemination of scientific research documents, whether they are published or not. The documents may come from teaching and research institutions in France or abroad, or from public or private research centers.

L'archive ouverte pluridisciplinaire **HAL**, est destinée au dépôt et à la diffusion de documents scientifiques de niveau recherche, publiés ou non, émanant des établissements d'enseignement et de recherche français ou étrangers, des laboratoires publics ou privés.



Systematic Analysis of Long-Period Earthquakes: Gorely Volcano, Kamchatka

Par *Sergei* **ABRAMENKOV**

Thèse de doctorat de Géophysique

Préparée à l'équipe de **Sismologie**

Dirigée par *Nikolai M.* **SHAPIRO**

Présentée et soutenue publiquement
(Par visioconférence en raison de COVID-19)
Le 18 mars 2021

Devant un jury composé de :

PEDERSEN <i>Helle</i>	Physicienne-HDR (Université Grenoble Alpes)	Président du Jury
MARGERIN <i>Ludovic</i>	DR-HDR (Université Paul Sabatier, Toulouse)	Rapporteur
SENS-SCHONFELDER <i>Christoph</i>	Senior Scientist (GFZ, Potsdam, Germany)	Rapporteur
METAXIAN <i>Jean Philippe</i>	CR-HDR (IPGP, Université de Paris)	Examineur
FERRAZZINI <i>Valerie</i>	Physicienne (IPGP, Université de Paris)	Examinatrice
KOULAKOV <i>Ivan</i>	Professor-HDR (Novosibirsk State University, Russie)	Invité



Sergei S. Abramnikov:

Systematic Analysis of Long-Period Earthquakes: Gorely volcano, Kamchatka

© version 1.0 (sent to reviewers) – February 2021

© version 1.1 (minor corrections) – April 2021

LIEU DE TRAVAIL :

Équipe de Sismologie

Institut de Physique du Globe de Paris

1 rue Jussieu

75238 Paris, France



Except where otherwise noted, this work is licensed under
<https://creativecommons.org/licenses/by-nd/3.0/fr/>

Analyse systématique des tremblements de terre de longue-période sur le volcan Gorely, Kamchatka

Gorely, étant l'un des nombreux volcans actifs du Kamtchatka, se distingue par la riche histoire magmatique reflétée dans sa structure composite et son activité de dégazage persistante. En 2013-2014, un réseau temporaire de 20 stations sismiques a été installé sur le volcan pour collecter des données de manière autonome pendant près d'un an. Pendant les quatre mois de son taux de dégazage élevé, l'activité sismique s'est principalement exprimée sous la forme d'un tremor sismique de longue période. Dans cette étude, un flux de travail basé sur la combinaison de méthodes de rétroprojection, d'analyse de grappes et de correspondance de modèles a été développé pour inspecter la signature sismique observée. Le traitement des enregistrements sismiques continus a donné un catalogue de tremblements de terre individuels de longue période qui se confondent pour constituer des signaux de type tremor observés. Un catalogue obtenu à l'aide de l'algorithme de détection par rétroprojection est constitué de 1741 événements à haute énergie. L'analyse des grappes a révélé qu'une partie importante des tremblements de terre de ce catalogue pourrait être regroupée en cinq familles, qui sont organisées séquentiellement dans le temps. L'utilisation de formes d'ondes empilées pour chaque famille dans la détection d'appariement de modèles a abouti au catalogue complémentaire de 80 615 événements à faible énergie. Une telle occurrence à long terme de séismes très répétitifs de longue période suggère un mécanisme non destructif qui peut correspondre à plusieurs modèles physiques. En fin de compte, les tremblements de terre de longue période sur Gorely représentent une signature sismique du système magmatique se comportant en réponse aux gaz à haute pression s'écoulant de la chambre magmatique décomprimée jusqu'au cratère du volcan.

Mots clefs : analyse typologique, sismicité de longue période, dégazage, volcan Gorely, Kamchatka

Systematic Analysis of Long-Period Earthquakes: Gorely Volcano, Kamchatka

Gorely, being one of many active volcanoes in Kamchatka, stands out due to the rich magmatic history reflected in its composite structure and persistent degassing activity. In 2013-2014, a temporary network of 20 seismic stations was installed on the volcano to gather data autonomously for almost a year. During the four months of its high degassing rate, seismic activity was mostly expressed in the form of a long-period seismic tremor. In this study, a workflow based on the combination of back-projection, cluster analysis, and template-matching methods was developed to inspect the observed seismic signature. The processing of continuous seismic records yielded a catalog of individual long-period earthquakes that merges to constitute observed tremor-like signals. A catalog obtained using the back-projection detection algorithm consist of 1741 high-energy events. Cluster analysis revealed that a significant part of earthquakes in this catalog could be grouped into five families, which are sequentially organized in time. Utilizing stacked waveforms for each family in the template-matching detection resulted in the complementary catalog of 80,615 low-energy events. Such long-term occurrence of highly repetitive long-period earthquakes suggests a non-destructive mechanism that may correspond to several physical models. Ultimately, long-period earthquakes on Gorely represent a seismic signature of the magmatic system behaving in response to the high-pressure gases flowing from the decompressed magma chamber up to the volcano's crater.

Keywords: cluster analysis, long-period seismicity, degassing, Gorely volcano, Kamchatka

*Моим родителям - Теологам,
встретившим друг друга в экспедиции
три с половиной десятилетия назад...*

*To my Muse, Viktoria 'Ugeg-žh', whose pure image has
saved my mind's wholeness from the depths of insanity
in the darkest hour of this postgraduate study...*

*À la mémoire de Docteur Kairly Jaxibulatov
(1990/3/17 - 2018/6/17)
brillant jeune scientifique et cher ami...*

Acknowledgements

First, I would like to express sincere gratitude to my supervisor, Nikolai Mikhailovich Shapiro, the person I admire as a researcher as well as a person. Nikolai's wisdom really shaped my character during these five years of a complicated PhD project, and I will never forget his commitment and the support he gave me on the way to become a fully responsible scientist. I would like to thank Ivan Yurievich Koulakov – my unofficial co-advisor from Novosibirsk, who was also my supervisor in undergraduate studies. Ivan actually gave me unique opportunities for fieldwork in Kamchatka.

I want to thank Institut de Physique du Globe de Paris and so many people I met there for this fantastic experience. It goes without saying that I'm already missing you all. My officemates and good friends: Piere, Jean, Sandro, Alister – hope we will meet again to discuss more science and life. Our great seismology student team: William, Leonard, Matthias, Vincent, Martha, Kevin, Florent, Marina, Thijs, John, Julian and Julien, Kurama, Miao, Hugo, Tristan, Shipra, Mathurin, Agnes, Anaïs and Pauline – you guys are rock solid! Awesome people from other departments of IPGP, I won't forget you either: Ekeabino, Manon, Oceane, Gino, Shihao, Aline, Marie, Delphine, Chizu, and of course dear Stasya and Tanya – it was a pleasure to meet you all! I'm deeply in debt for the help and understanding you gave me during my burnout phase in the second year of this project... I'm sorry that I wasn't quite responsive or supportive in return, at least not to the degree you guys deserve it. Thank you for all conversations and the hardcore-emotional experience of education we shared together these years!

From a more professional perspective, I genuinely appreciate all discussions with my more experienced colleagues: Natalia Poiata, Nobuaki Fuji, Claudio Satriano, Paskal Bernard, Martin Vallee, Jean-Paul Montagner, Jean-Pierre Vilotte and Jean Philippe Metaxian. My deepest gratitude to Eleonore Stutzmann, Clement Narteau and Sylvie Contamina for their strong support in few incidents that happened during my work in the institute and for all the official protection and paperwork required. My deepest respect is reserved for people who made this research possible – our field experiment team on Gorely and in many further expeditions: Ilyas Abkadyrov, Andrey Jakovlev, Evgeniy V. Deev, Pavel Kuznetsov, Arseniy Ivanov and Alehjandro Diaz Moreno.

Finally, I wish to thank the Russian government fund "Global Education Program" – my primary financial source that made this study abroad possible. Personal gratitude to Elena Zaytseva for her constant support and patience. Big thanks to Ekaterina Gulyaeva, who helped with the manuscript proofreading, to Ivan Karpov, who motivated me by example and to my friends in Russia, who believed in me even when I almost gave up (twice). For you all, this is proof that I was worth it!

Abbreviations

BP	<i>Back-Projection (method)</i>
BPI	<i>Back-Projection Intensity</i>
CC	<i>Correlation Coefficient</i>
CF	<i>Characteristic Function</i>
EVF	<i>Eastern Volcanic Front (of Kamchatka)</i>
FT	<i>Fourier Transform</i>
FFT	<i>Fast Fourier Transform</i>
HF	<i>High-Frequency range (> 5 Hz)</i>
LF	<i>Low-Frequency range (< 5 Hz)</i>
LP	<i>Long-Period (singular earthquake or type of seismicity in general)</i>
LPs	<i>Long-Period earthquakes (plural)</i>
P-	<i>Primary body wave (compressional), or its phase on a seismogram</i>
Q	<i>Quality factor</i>
RSAM	<i>Real-time Seismic Amplitude Measurement</i>
S-	<i>Secondary body wave (shear), or its phase on a seismogram</i>
STA/LTA	<i>Short-Term Average to Long-Term Average ratio</i>
STFT	<i>Short-Time Fourier Transform</i>
TM	<i>Template Matching (method)</i>
ULP	<i>Ultra-Long-Period (earthquake dominant period > 100 s, < 0.001 Hz)</i>
VEI	<i>Volcanic Explosivity Index</i>
VLP	<i>Very-Long-Period (earthquake dominant period from 2 s to 50 s, 0.5 to 0.01 Hz)</i>
VT	<i>Volcano-Tectonic (singular earthquake or type of seismicity in general)</i>
1D	<i>One-Dimensional</i>
2D	<i>Two-Dimensional</i>
3C	<i>Three-Component</i>
3D	<i>Three-Dimensional</i>
4D	<i>Four-Dimensional</i>

Content

Preface	Error! Bookmark not defined.
Acknowledgements	iii
Abbreviations	iv
Content	v
List of Figures	vi
Introduction	1
Study motivation & Thesis structure	12
PART I STUDY BACKGROUND	14
Chapter 1: Essentials of Volcano Seismology	15
1.1: Historical roots	15
1.2: Seismic monitoring of volcanoes	17
1.3 Classification of volcano-seismic signals	27
Chapter 2: Long-Period Volcanic Earthquakes	37
2.1 Observations of LP seismicity	37
2.2 Physical mechanisms and models	44
Chapter 3: Seismic Experiment on Gorely	49
3.1: Gorely volcano	49
3.2 Temporary seismic network of 2013-2014	59
PART II STUDY CONTENT AND RESULTS	64
Chapter 4: Compilation of Volcano-Seismic Catalog	65
4.1 Back-projection based detection and location	65
4.2 Application to Gorely's temporary network data	73
Chapter 5: Waveform-similarity based cluster analysis	77
5.1 Catalog inspection via correlation coefficient matrix	77
5.2 Clustering process	80
Chapter 6: Catalog extension via template matching	83
6.1 Template matching method	83
6.2 Seismic characteristic of the degassing episode	85
6.3 Interpretation	86
Conclusions	89
Bibliography	90
Publications	97

List of Figures

FIGURE 1 - CONCEPTUAL SKETCH OF MANTLE DYNAMICS	2
FIGURE 2 - TECTONIC SETTINGS OF VOLCANISM ON EARTH	3
FIGURE 3 CLASSIFICATION OF IGNEOUS ROCKS	6
FIGURE 4 MAJOR TYPES OF VOLCANIC ERUPTIONS	7
FIGURE 5 – VOLCANIC EXPLOSIVITY INDEX (VEI) CRITERIA	8
FIGURE 6 EFFECTS OF A LARGE VOLCANIC ERUPTION IN TIME AND OVER DISTANCE	10
FIGURE 7 – MAP OF THE STRONGEST VOLCANIC ERUPTIONS.....	11
FIGURE 1.1 - A COMPARISON BETWEEN MANUAL COUNTING AND AUTOMATED RSAM MONITORING	18
FIGURE 1.2 - CUMULATIVE REDUCED DISPLACEMENT PLOT	19
FIGURE 1.3 – SPECTROGRAM COMPUTATION PROCESS	21
FIGURE 1.4 – A COMPARISON BETWEEN TRADITIONAL SPECTRAL ANALYSIS AND CONTINUOUS WAVELET TRANSFORM	23
FIGURE 1.5 – 3D SHEAR VELOCITY MODEL BELOW THE TOBA CALDERA AND ITS INTERPRETATION.....	26
FIGURE 1.6 – SEISMOGRAMS OF DIFFERENT VOLCANIC SEISMICITY TYPES IN THE CLASSIFICATION OF TAKESHI MINAKAMI.....	28
FIGURE 1.7 – COLIMA VOLCANO OBSERVATORY CLASSIFICATION.	28
FIGURE 1.8 – VOLCANIC SEISMICITY CLASSIFICATION MENTIONED IN THE ENCYCLOPEDIA OF VOLCANOES.....	29
FIGURE 1.9 – COMPARISON OF DIFFERENT TYPES OF SEISMOGENIC SURFACE MOVEMENTS	30
FIGURE 1.10 – SLIDING BLOCK AND GRANULAR FLOW MODELS OF SURFICIAL SEISMICITY	31
FIGURE 1.11 – SPECTROGRAMS AND SEISMOGRAMS FOR VOLCANO-TECTONIC EARTHQUAKES.....	32
FIGURE 1.12 – THREE MODELS FOR RELATIONSHIP BETWEEN MAGMA MIGRATION AND LOCAL VT EARTHQUAKES.....	32
FIGURE 1.13 – COMPARISON BETWEEN VOLCANIC SEISMICITY WAVEFORMS.....	34
FIGURE 1.14 – CONTEMPORARY VIDEO AND 3C SEISMIC RECORDS DURING STROMBOLIAN EXPLOSION.....	35
FIGURE 2.1 – WAVEFORMS OF LP EVENTS.....	38
FIGURE 2.2 – EXAMPLES OF LONG-PERIOD SEISMIC WAVEFORMS AND THEIR FOURIER SPECTRA	39
FIGURE 2.3 – EXAMPLE OF REPEATING LONG-PERIOD EARTHQUAKES	40
FIGURE 2.4 – DIFFERENT KINDS OF VOLCANIC TREMOR	42
FIGURE 2.5 – TIME-FREQUENCY REPRESENTATION AND SEISMOGRAM OF VOLCANIC TREMOR EPISODES	43
FIGURE 2.6 – A CYLINDRICAL MAGMATIC CONDUIT MODEL	45
FIGURE 2.7 – SPHERICAL MAGMA CHAMBER MODEL.....	45
FIGURE 2.8 – FLUID-FILLED CRACK MODEL	46
FIGURE 2.9 – MODEL OF NONLINEAR EXCITATION BY VISCOUS, INCOMPRESSIBLE FLUID FLOW	47
FIGURE 2.10 – SCHEMATIC ILLUSTRATION OF GAS BUBBLE COALESCENCE MODELS	48
FIGURE 2.11 – LABORATORY MAGMA DEGASSING EXPERIMENT	48

FIGURE 3.1 – MAIN GEOGRAPHICAL AND TECTONIC UNITS IN THE STUDY REGION	50
FIGURE 3.2 – GORELY VOLCANO IN THE TECTONIC CONTEXT OF KAMCHATKA	52
FIGURE 3.3 – PHOTOGRAPHY OF THE GORELY’S CURRENTLY ACTIVE CRATER	53
FIGURE 3.4 – SIMPLIFIED GEOLOGICAL MAP OF GORELY	55
FIGURE 3.5 – INTERPRETATION OF THE GORELY’S TOMOGRAPHY MODEL	58
FIGURE 3.6 – THE TEMPORARY SEISMIC NETWORK ON GORELY (AUGUST 2013–AUGUST 2014).....	59
FIGURE 3.7 – EQUIPMENT OF A TEMPORARY SEISMIC STATION AND THE INSTALLATION PROCESS	60
FIGURE 3.8 CODA-NORMALIZATION PROCESS FOR A CHOSEN N-S COMPONENT	62
FIGURE 3.9 EXAMPLE OF THE LPS SWARM ON GORELY DURING THE LATE PHASE OF DEGASSING PROCESS	63
FIGURE 4.1 – GENERAL CONCEPT OF THE BACK-PROJECTION METHOD.....	66
FIGURE 4.2 – PRINCIPLE OF THE BENDING ALGORITHM FOR THE RAY TRACING	68
FIGURE 4.3 – GENERAL DETECTION IDEA OF KURTOSIS FUNCTION	70
FIGURE 4.4 – EXAMPLE OF THE BP DETECTION PROCEDURE FOR A HIGH-ENERGY LP EVENT ON GORELY	74
FIGURE 4.5 – RESULTS OF APPLYING THE BP DETECTION ALGORITHM TO GORELY DATA.	75
FIGURE 5.1 – THE BP-BASED CATALOGUE	77
FIGURE 5.2 – SIMILARITY ASSESSMENT OF EARTHQUAKES FROM THE BP BASED CATALOG	79
FIGURE 5.3 – CLUSTERING PROCESS FOR 1741 HIGH-ENERGY EARTHQUAKES	80
FIGURE 5.4 – CLUSTER ANALYSIS RESULTS FOR THE BP BASED CATALOGUE	82
FIGURE 6.1 – TEMPLATE WAVEFORMS FOR FIVE CLOSEST TO SUMMIT STATIONS.....	84
FIGURE 6.2 – THE MF-BASED CATALOGUE OF LOWER-ENERGY EVENTS IN COMPARISON.....	85
FIGURE 6.3 – SUGGESTED INTERPRETATION OF GORELY DEGASSING EPISODE.....	88

Introduction

*“And then at last over the miles between there came
a rumble, rising to a deafening crash and roar;
the earth shook, the plain heaved and cracked,
and Orodruin reeled.”*

*Prof. Tolkien's description of a catastrophic
hobbit-triggered volcanic earthquake*

Volcano seismology as a domain set at the intersection of two distinct geological disciplines may be approached from two principal points of view. While a volcanologist is more interested in revealing details of the magmatic process itself, a seismologist is puzzled by the abundance of various seismicity generated by an active volcano. The present study provides an example of the latter, focusing on the specific type of volcanic seismicity observed at a particular volcano. Since this research is more inclined towards seismology, the introduction aims to keep it balanced by highlighting volcanology foundations.

Key geological concepts are briefly described first, explaining volcanism's global role in Earth's evolution and its tectonic constraints. A short overview of magma geochemistry is directed to explain various volcanic structures and corresponding differences in their eruption style. Finally, the impact of volcanic activity on humankind is concisely emphasized to stress the topic's significance. The study motivation is presented at the end of this introduction, along with the chosen thesis structure.

Volcanism as a geological process

Different constituents of a planetary body tend to segregate from each other according to their physical and chemical properties in the process of planetary differentiation. Earth underwent primary gravitational separation by density during its formation 4.51 billion years ago. As a result, the typical terrestrial system has been developed: dense metallic core in the center, silicate mantle surrounding it, and chemically diverse crust covering planet surface. Mantle dynamics and plate tectonic

movements indicate that our planet is still following an evolutionary trend towards a gravitationally and thermally stable layered structure. As long as there are regions within where temperature and pressure allow a substance to be in a liquid or partially melted state, the differentiation process will continue arranging elements according to their physical parameters and chemical affinity. Such motion led to the core segregation into solid and liquid parts. The same process drives magmatism in the crust.

In the grand terrestrial scheme, volcanism could be viewed as a manifestation of deep thermal processes on the planet's surface. The internal heat flow ultimately drives volcanic activity as high temperature provides necessary conditions for partial melting of rocks at sufficient geostatic pressure. In addition to primordial heat accumulated from the kinetic energy of impact events during planetary accretion and subsequent gravity-driven differentiation, energy is released by radioactive decay of various isotopes trapped inside the planet's interior and crystallization process in the inner core. Heat is primarily transferred via mantle convection – a mechanism of slow creeping motion, in which solid silicate mantle behaves like an extremely viscous fluid in geological time scale. While warmer bulk of mantle floating up, colder masses are sinking deeper, forming convection cells. In some areas, abnormally hot material from the core-mantle boundary can move straight to the surface, forming mantle plumes (*Figure 1*). Such character of mantle dynamics causes heat flow anomalies in the lithosphere, providing necessary circumstances for magmatic processes in various tectonic settings, which in turn give rise to volcanic activity.

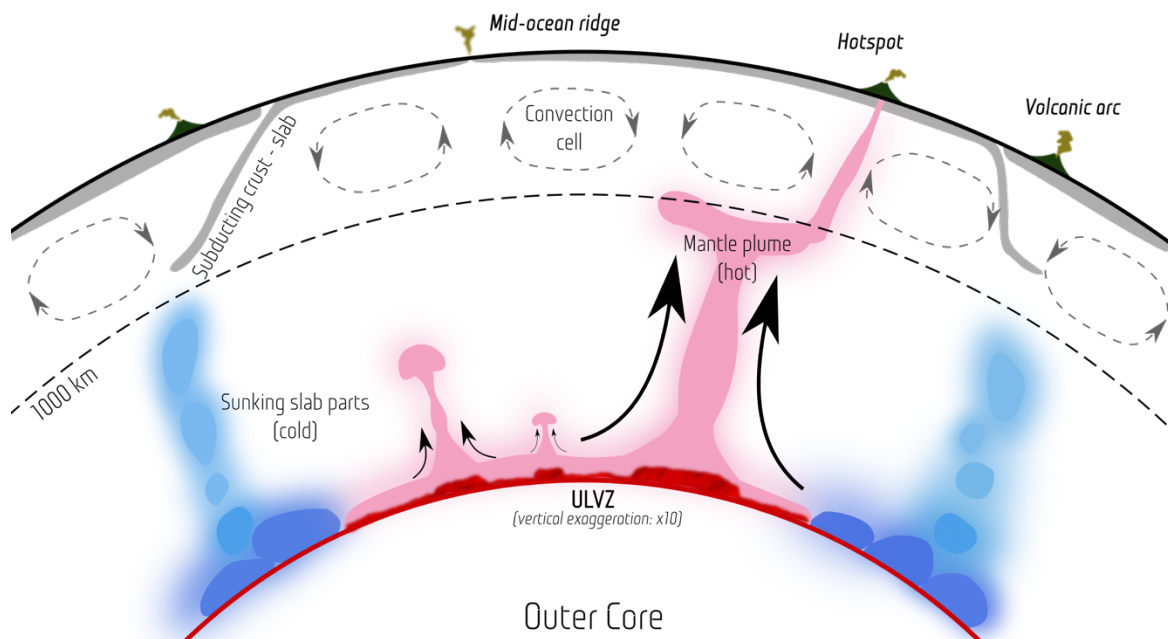


Figure 1 - Conceptual sketch of mantle dynamics based on the recent discovery of Ultralow-velocity zones (ULVZ) – localized regions of extreme material properties detected seismologically at the mantle base. Such structures appear to be root characteristics of mantle plumes. The thick dashed line indicates the depth of 1000 km, where many large plumes are deflected horizontally, and some slabs stagnate. Above the line, in the upper mantle, convection cells are more pronounced, while below it, the sinking slabs are more fragmented. Modified after Yuan & Romanowicz (2017).

Volcanic activity as a tectonic feature

From a tectonic point of view, volcanoes are formed under specific geological conditions defined by lithospheric plate interactions driven by mantle convection. Most of the current volcanic activity tends to occur at plate boundaries: either divergent at mid-ocean ridges and rift systems or convergent at continent and island volcanic arcs (Figure 2). There are, however, examples of intraplate volcanism that could be attributed to the existence of mantle plumes beneath.

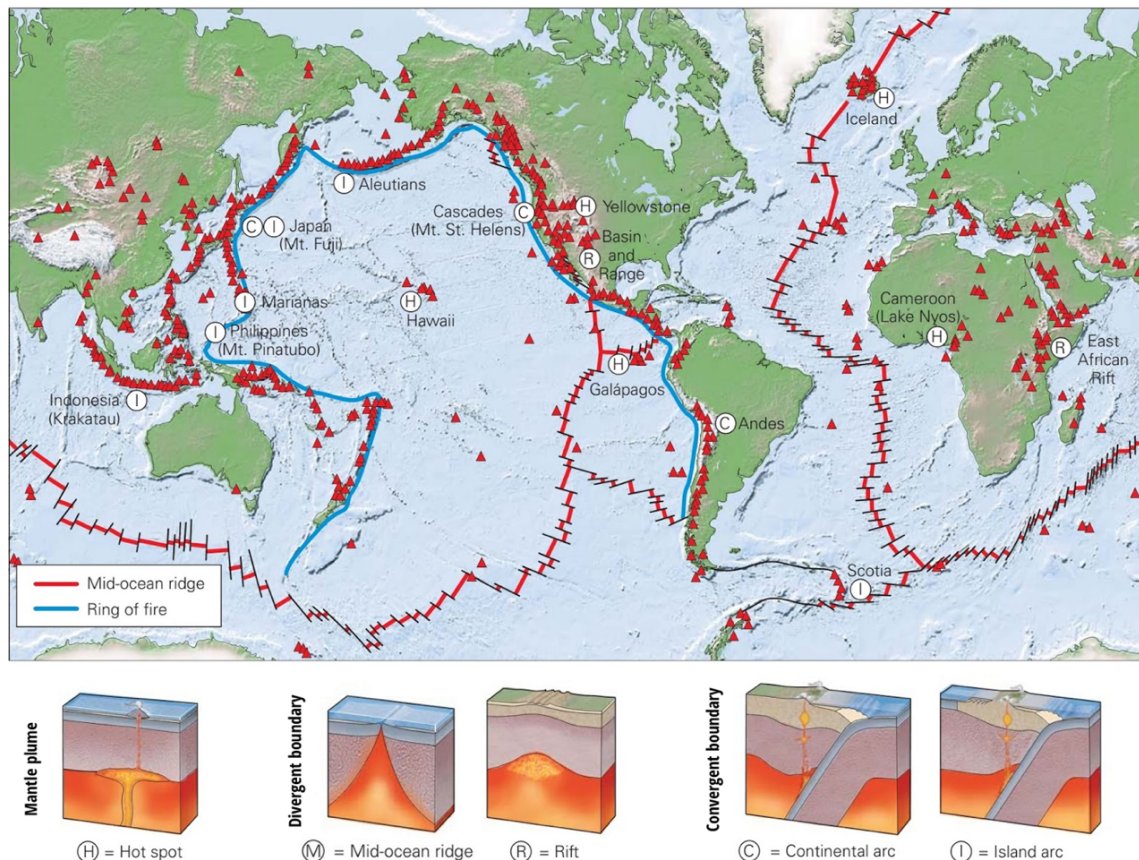


Figure 2 - Tectonic settings of volcanism on Earth: a vast portion of volcanic activity is almost unnoticeable due to its submarine nature in mid-ocean ridges; directly observable volcanoes on land are primarily located in subduction zones (ex. the famous Ring of Fire around the Pacific). Modified after Condie (1997).

Examples of intraplate volcanism are found both in the oceanic and continental lithosphere. For instance, well-studied Hawaii Island is a classical hot spot where mantle plume penetrates thin oceanic crust. Hawaiian-Emperor seamount chain is a piece of strong evidence that this narrow channel in the mantle has been stable for more than 80 million years, while the Pacific plate was moving over it. Flood basalts discovered worldwide are another manifestation of the mantle plumes that had faced thick continental crust and therefore were forced to spread underneath it over a vast area. After the subsequent warming of crustal rocks above, vast amounts of material had been rapidly erupted on the surface. These so-called Large Igneous Provinces are exceptional cases of volcanism that have

formed many oceanic plateaus. The most prominent example of this phenomenon on land is Siberian traps, which are believed to be the reason for the devastating mass extinction during the Permian-Triassic transition (251-250 Ma). It is crucial to note that such catastrophic events happened in a relatively short time window in geological timescale but were several orders of magnitude longer and more influential than any eruption ever witnessed by humanity.

Volcanic activity at divergent boundaries of lithospheric plates is also going on inland (rift systems) and underwater (mid-ocean ridges). In both tectonic environments, volcanism is explained by the decompression melting of hot asthenosphere above the upwelling current of a mantle convection cell. Since many divergent plate boundaries are located at the ocean bottom, a substantial part of our planet's current volcanic activity is submarine. This type may be regarded as the least violent case, which holds a productive role in constant crust recreation without severe damage to the biosphere.

Finally, convergent boundaries represent the most complex tectonic conditions of volcanism, especially in subduction zones because, in this case, an additional agent is strongly involved in magmatic processes. The influx of water released from the top part of a descending oceanic plate forces the melting-point depression of surrounding rocks. Moreover, return flow in the mantle wedge overlying subducting plate further drives partial melting. Due to these two effects combined, magmatic processes in the subduction zone stand out by geochemical complexity. Signature diversity in eruption styles is the expected result of volcanic activity in such tectonic settings. Great examples may be marked along the famous "Ring of Fire" built by several subduction zones.

Volcano structure as a magmatic composite

A volcano is essentially a vent in the planet's crust, which connects a deep magma source with the surface. Volcanoes can be divided into groups according to the chemical composition of the erupted material in the same manner as extrusive igneous rocks that make up their edifices. The geochemistry of a source magma (*Figure 3*) affects its physical properties and predominantly defines a volcano's morphological structure and eruption character. As the silica content increases, extrusive rock types generally express a more viscous behavior, while the higher portion of a gas content making an eruption process more explosive. Volcanoes are typically classified by their shape or eruptive habit. Alternatively, geochemical categorization is a reasonable way to approach the matter from the magma properties differences. The following three paragraphs summarize geochemistry essentials for the main types of extrusive rocks.

Basaltic lavas

Basaltic magmas are the most common type of melt – they can be found in all tectonic settings presented above. Produced along mid-ocean ridges, in continental rift environment, and from hot spots in the mantle beneath oceanic plates, basaltic lava has low viscosity due to its high eruption temperature (1000° to 1200°C) and chemical composition: low silica content, high amount of iron, magnesium, and calcium. Flowing lava streams generally reach velocities of a few kilometers per hour. Basaltic eruptions are rarely explosive: more often, hot fluid magmas fill-up the volcano's plumbing system and overflow the volcano's flanks in voluminous streams. Thus, a *shield volcano*, built by the accumulation of thin basaltic flows, is the most typical morphological structure for a primarily basaltic volcanic system.

Andesitic and dacitic lavas

Dacitic and andesitic magmas erupt mainly in the volcanic belts along subduction zones. Both types of lava, being intermediate in the silica content range of volcanic rocks, have medium viscosity and lower eruption temperature (800° to 1000°C). They move slower than their basaltic analog but faster than a very viscous rhyolitic counterpart. A *volcanic cone*, built by blocky lava deposits and pyroclastic material, may be considered the most common morphology of such volcanic systems. The source magma composition often alternates between intermediate and mafic composition, forming a *stratovolcano* – a concave-shaped structure of alternating lava flows and beds of pyroclastic deposits.

Rhyolitic lavas

Rhyolitic magmas are produced in specific tectonic settings where the mantle heat has melted significant continental crust volumes. Rhyolite lavas have felsic composition: silica content greater than 68 percent, high sodium and potassium percentages. Rhyolite is richer in silica than any other volcanic rock type and has the lowest melting point (erupting at only 600° to 800°C) – therefore, rhyolitic lavas have the highest viscosity. They are least fluid and usually flow ten times slower than the basaltic counterpart, forming bulbous deposits that may plug the vent. A *lava dome* is a morphological type common for the thick masses of felsic lava. Domes being a rounded, steep-sided mass of rock with a minimal lateral spreading, often trapping volcanic gases below, until the pressure increases above the explosion limit, which blasts existing dome into fragments.

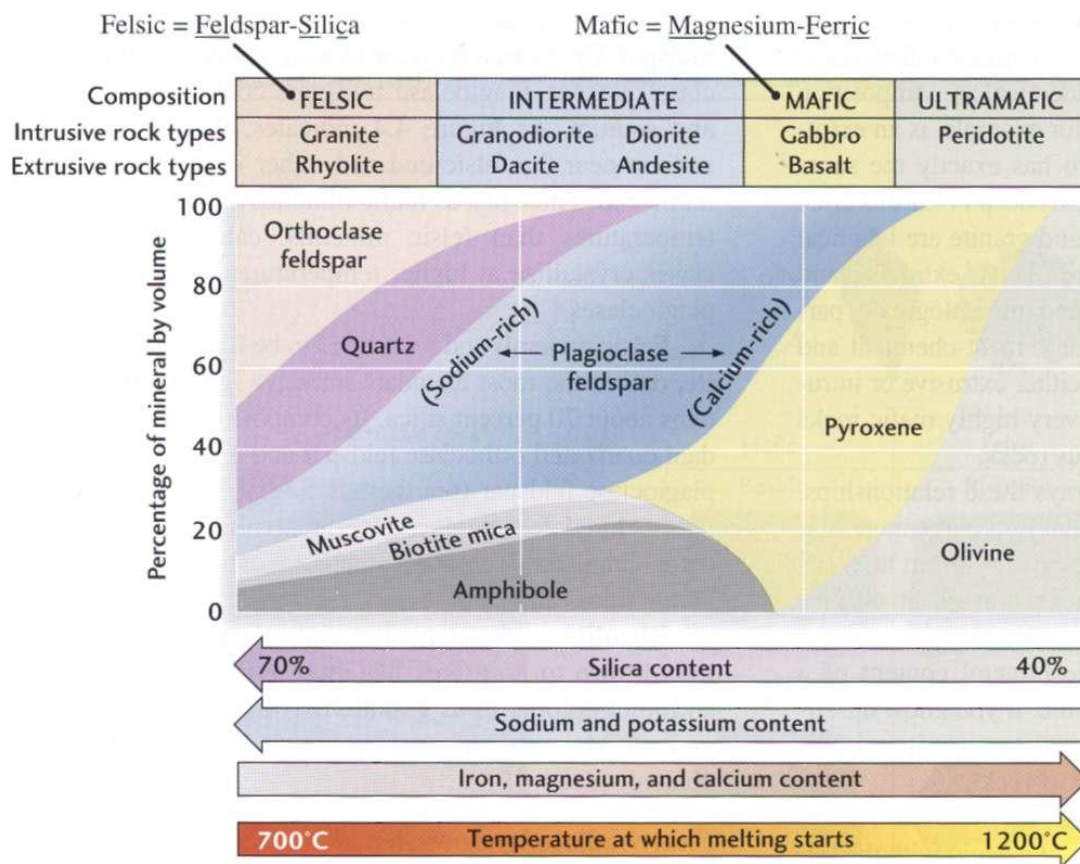


Figure 3 *Classification of igneous rocks*: The vertical axis shows a given rock's mineral composition as a percentage of its volume. The horizontal axis is a scale of silica content by weight. Modified from Grotzinger (2007).

Volatile components in a volcanic eruption

Magma sources related to converging tectonic settings generally have a high gas content with different kinds of volatile components. The vast mass bulk of it is water and carbon dioxide, but volcanoes also release a significant amount of hydrogen sulfide, sulfur dioxide, hydrogen chloride, and hydrogen fluoride as volatiles. In low-viscosity basaltic magma, dissolved volatiles can quickly boil out – that is why such eruptions are mostly effusive. In high-viscosity rhyolite magma, the magma's gaseous part remains pent up until it reaches the pressure sufficient to blow the viscous magma into fragments. The magma ascending rate, linked to the reduction of pressure, primarily controls the degree of explosiveness for a particular volcano.

Volcanic eruption as a physical process

A volcanic eruption is essentially an event of magmatic system discharging, in which material from the inner (subsurface) part moving up to the atmosphere or into the ocean (in case of submarine volcanoes) through a vent or fissure. The ejected material usually includes lava, tephra, and assorted

gases mixed with fractured pieces of the existing volcanic edifice – for example, a demolished volcanic plug or dome. Generally, volcanic eruptions are divided into **effusive**, involving a rather tranquil style of the lava outpouring, and **explosive**, in which magma is often shattered into pyroclastic fragments. The eruption style and the degree of explosiveness are primarily defined by magma viscosity, volatiles dissolved in magma and its ascending rate, as mentioned in the previous subsection.

Volcanic eruptions are divided into three types according to the physical process that drives it. A *magmatic eruption* involves the decompression of gas within magma that moves it upward. In this way a *phreatomagmatic eruption* may be considered directly opposite as it is driven by the compression of gas within magma resulting from the interaction between molten material and water. Finally, a *phreatic eruption* occurs due to the near-instantaneous evaporation of ground water to steam caused by its heating from the magmatic source. All three types may bring juvenile material to the surface and usually an explosive eruption is also accompanied by gas-emission.

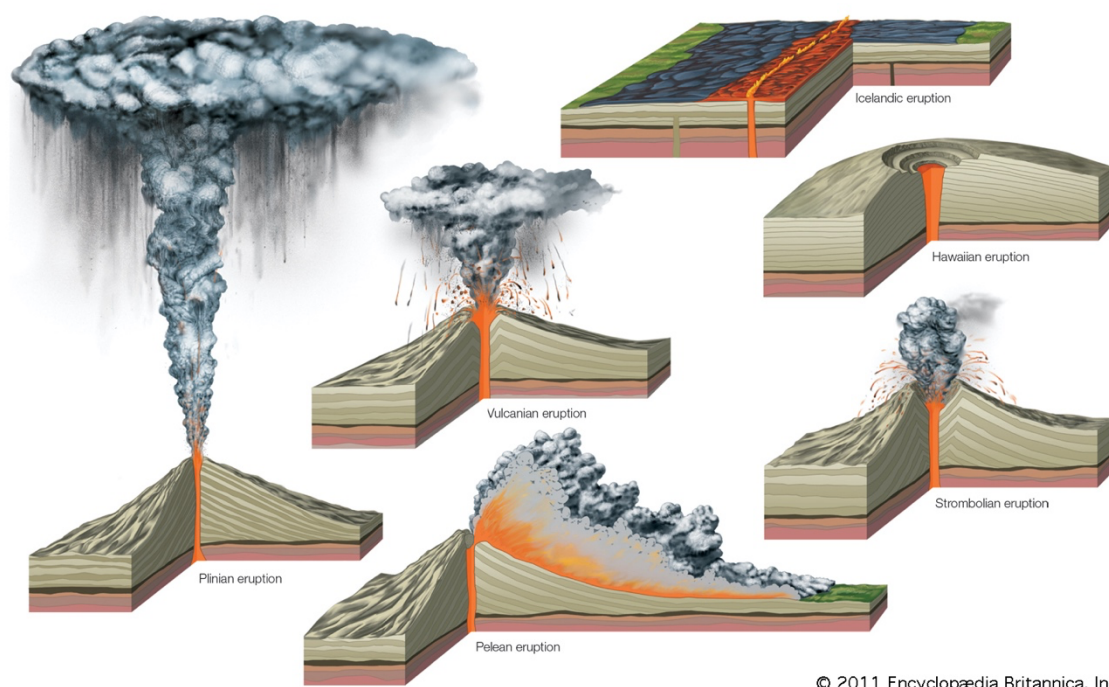


Figure 4 Major types of volcanic eruptions named after particular volcanoes, volcanic regions and eruption events. From Encyclopædia Britannica (2011). <https://www.britannica.com/science/volcano/Six-types-of-eruptions>

The common classification of volcanic eruptions is based on character of volcanic activity and divided into six major types (Figure 4). Following a geochemical approach to volcano diversity one may group these types according to the magmatic composition of respective volcanoes. Activity of predominantly basaltic volcanoes is expressed as the *Hawaiian* or the *Icelandic* type, depending on the volcanic system geometry. In the former case, fluid lava flows from a volcano's summit and radial fissures to form shield volcano, in the latter it runs from long, parallel fissures building large lava

plateaus. Most andesitic and dacitic volcanoes demonstrate the *Strombolian* or the *Vulcanian type* of eruption, generally involving minor to moderate bursts of expanding gases that eject clots of incandescent lava and gas laden with volcanic ash. The difference between these two types is mainly in frequency and amount of ejected material. Finally, the most violent and destructive types of eruption are characteristic of rhyolitic magmas. The *Pelean type* is associated with strong explosive outbursts leading to the collapse of lava dome that can generate devastating pyroclastic flows – a dense mixtures of hot (reaching more than 1000°C) fractured material and gases that moves down the slope at tremendous speed (often over 150 km/s). The *Plinian type* may be even more catastrophic, because the similar powering process of dissolved volatile gases expansion starts in the magma chamber itself. Resulted eruptive column is a distinct feature of this volcano explosion type.

As the chemical composition in many volcanic systems is not limited to a single rock type, so the eruptive style is not bound to one specific type. For example, Plinian eruption may as well occur at basaltic volcano, if the magma differentiation process has formed a chamber rich with highly viscous magma and sufficient volume of volatiles. As a matter of fact, most volcanoes located in the subduction zones frequently display many different types of eruption even in the span of a single cycle of activity. Most eruptions are almost unnoticeable, while a particular one may completely destroy the volcanic edifice and its surroundings. A semi-quantitative scale logarithmic scale known as the *Volcanic Explosivity Index (VEI)* was developed to assess the impact of eruption. The vast majority of events falls between values of 0 and 2, while only few catastrophic ones reaching values higher than 6. A short summary of the VEI chart is presented in *Figure 5*.

VEI	0	1	2	3	4	5	6	7	8
General Description	Non-Explosive	Small	Moderate	Moderate-Large	Large	Very Large			
Volume of Tephra (m ³)	1x10 ⁴	1x10 ⁶	1x10 ⁷	1x10 ⁸	1x10 ⁹	1x10 ¹⁰	1x10 ¹¹	1x10 ¹²	
Cloud Column Height (km) Above crater Above sea level	<0.1	0.1-1	1-5	3-15	10-25	>25			
Qualitative Description	"Gentle,"	"Effusive"	"Explosive"		"Cataclysmic," "paroxysmal," "Severe," "violent," "terrific"		"colossal"		
Eruption Type (see fig. 7)	Hawaiian		Strombolian		Vulcanian		Plinian Ultra-Plinian		
Duration (continuous blast)	<1 hr		1-6 hrs		6-12 hrs		>12 hrs		
Maximum explosivity	Lava flow	Phreatic		Explosion or Nuée ardente					
	Dome or mudflow								
Tropospheric Injection	Negligible	Minor	Moderate	Substantial					
Stratospheric Injection	None	None	None	Possible	Definite	Significant			
Eruptions	976	1239	3808	1083	412	168	50	6	0

Figure 5 – Volcanic Explosivity Index (VEI) criteria. Reproduced after Newhall & Self (1982).

It is important to note that assigning the VEI value is based on eight criteria in total. In most cases the principal ones are the erupted tephra volume (for ancient eruptions) or a combination of plume height and eruptive volume (for modern eruptions). This capability to use both quantitative and qualitative data, even if some information is missing, allows a great number of eruptions to be classified. However, the VEI implicitly assumes that eruption magnitude and intensity are related, which is not necessarily true.

The impact of volcanism

Volcanic activity has been shaping our planet's surface for over 4 billion years. From a continuous crust reproduction to the creation of Earth's atmosphere – the geological impact of volcanism is truly tremendous. In a nutshell, volcanism is the phenomenon to which we owe the existence of all land and water available. Moreover, active volcanoes are the source of fertile soils, rare and valuable minerals, building materials and geothermal energy.

While several pages above describe the role and effects of volcanism in the scope of geology, it is rational to close this introduction with the present research relevance. Volcanic activity has provoked continuous search for answers throughout the history of humankind. The inception of civilization itself is tailed to regions of active magmatism. For our ancestors, the idea that solid earth may suddenly break right under their feet and bombard them with glowing hot ejecta seemed almost inexplicable. Mythological and religious explanations were later superseded by the rise of natural philosophy, as people began to look for actual physical causes of volcanism.

Beside rather positive outcomes of the volcanic activity described earlier, there is a more dreadful angle to look on the phenomenon. Violent volcanic eruptions with tragic outcomes are relatively rare in comparison to overall daily eruptive activity on our planet. While small continues eruptions underwater are slowly moving tectonic plates apart during millions of years, a powerful catastrophe on land may depart a whole culture to the annals of history in a single day. Volcanoes are traditionally viewed as terrifying and spectacular landmarks. No wonder that volcanic eruption is a metaphor for the ultimate extermination in many cultures, which is also frequently used in literature and cinema as a plot device. Mount Doom or Orodruin is probably the most well-known example of a fictional volcano, whose eruption process, however, is depicted quite realistically by Prof. Tolkien J.R.R. in his monumental novel “The Lord of the Rings”. Such sublime representations did not arise from scratch: real volcanoes that inspired the most touching works in different forms of art are those that brought tragedy to the people living near them, such as Vesuvius in 79 AD or Krakatau in 1883.

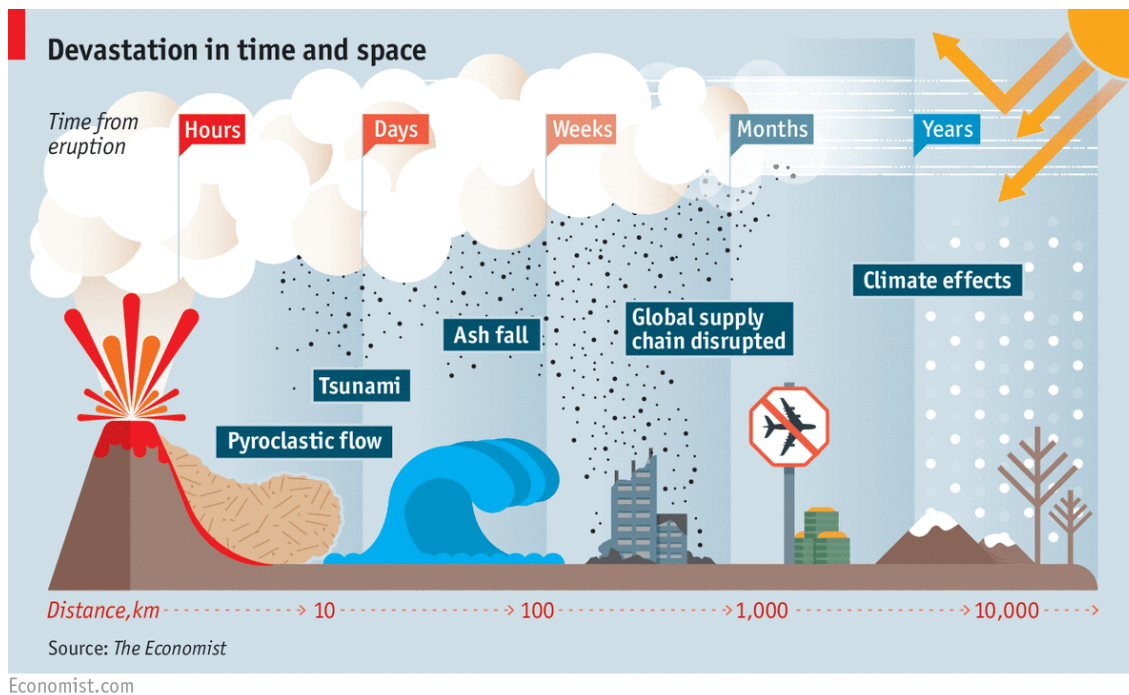


Figure 6 Effects of a large volcanic eruption in time and over distance. Infographic copyright: "The Economist"
<https://www.economist.com/briefing/2015/04/11/after-tambora>

Despite their spectacular appearance, volcanic eruptions have not been the deadliest natural hazard. Since 1700 it has taken a total of 260,000 lives, which pales in comparison with the death toll from earthquakes and tropical storms. However, the effects of a catastrophic volcanic eruption may spread on a great distance from the actual volcano location (Figure 6). The ash cloud rose into the stratosphere affects the climate on a global scale due to the atmosphere cooling caused by the emission of sulfur dioxide, which later oxidized to sulfate ions developing tiny particles that reflects sunlight away. witnessed the full range of volcanic eruptions that our planet is capable to produce. Krakatau in 1883 and the Tambora eruption of 1815 (Figure 7) may be regarded as 100 years and 1000 years events respectively. How much unknown about volcanic explosions that may occur on a large time scale? What is the upper limit of eruption magnitude and will civilization be able to survive such an event?

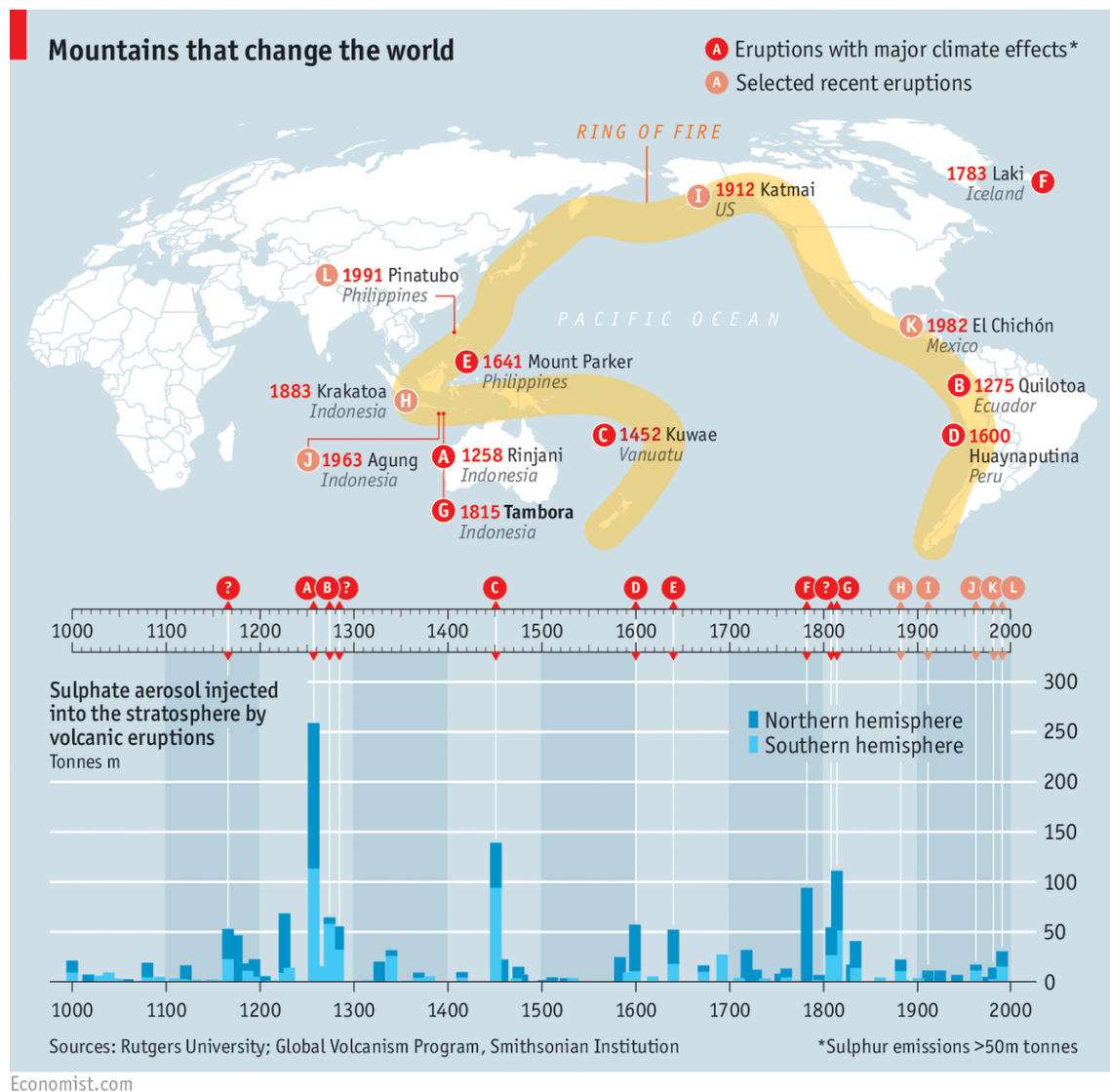


Figure 7 – Map of the strongest volcanic eruptions in the past 1000 years with their estimated climate effects. Infographic copyright: “The Economist” <https://www.economist.com/briefing/2015/04/11/after-tambora>

Thus, assessing volcanic eruption risk is more than a concern of people living near active magmatic regions. From the planetary perspective of time, it is a serious threat to the whole humankind. While the probability of a super volcano eruption in a single lifetime is exceptionally low, the climate effect of such an event may become completely devastating for the human species. One should not forget chillingly wise words of William Durant, “The Story of Civilization” author: *“Civilization exists by geologic consent, subject to change without notice.”*

Study motivation & Thesis structure

The thesis is aimed to add a piece of knowledge to the volcano seismology domain via studying of volcano-seismic signals linked to the degassing episode of Gorely volcano, located in Kamchatka. The scientific advisor proposed an initial idea to the author after a seismic experiment, that provided unique data for this volcano. In a nutshell, the primary goal of the present research may be outlined as *‘a compilation and detailed investigation of the earthquake catalogue consisting solely of a specific long-period volcanic seismicity type in case of a particular volcano during several months of its degassing activity’*.

The thesis structure is divided into two main parts supplemented by introduction and conclusion. The first part is named **STUDY BACKGROUND** as it covers the current state of knowledge on the topic as seen by the author. It consists of three chapters ordered to keep logical synopsis started in the introduction. **Chapter 1** (*Essentials of Volcano Seismology*) highlights the fundamental ideas that are crucial for the understanding of challenges and problems arising at the intersection of volcanology and seismology, painting the broad thesis context. **Chapter 2** (*Long-Period Volcanic Earthquakes*) summarizes existing observations and main physical models for a specific type of volcanic seismicity called *long-period earthquakes* – the primary focus of this research. **Chapter 3** (*Seismic Experiment on Gorely*) describes volcano’s geological structure and eruption history in the tectonic context of Kamchatka, showcasing the data acquired during a one-year seismic experiment carried out on Gorely using a temporary seismic network consisted of 21 instruments.

Following the definition of study's main challenges, the essence of this research is condensed in the second part named **STUDY CONTENT AND RESULTS**. It also contains three chapters, which reflect three principal methods used to build, verify and extend a catalog of long-period earthquakes, ultimately opening a possibility to analyze this particular type of seismicity on Gorely volcano systematically. **Chapter 4** (*Compilation of Volcano-Seismic Catalog*) describes the automatic earthquake detection algorithm based on the *back-projection method* that uses advantages of a seismic network, followed by results of its application to Gorely. **Chapter 5** (*Waveform-similarity based cluster analysis*) covers the developed approach for *cluster analysis* of similar long-period earthquakes recorded during a degassing episode of Gorely, that revealed a sequential clustered pattern in their temporal appearance. Finally, **Chapter 6** (*Catalog extension via template-matching*) suggests the *template-matching method* as a tool for catalog extension using waveforms of previously discovered long-period earthquake clusters to form a cluster template for search in continuous data. Thus, the information presented in the second part of the thesis providing new knowledge to the field of volcano seismology, effectively ratifying the author as a person capable of carrying scientific research in this domain.

The author with colleges published the core part of this study in a condensed form as a paper in ‘Geosciences’ journal (Abramenkov et al., 2020), reprint of which is included in the end matter of this manuscript. A reader looking for a quick acquaintance with the study may find it preferable to the full thesis text. Chapters 3-6 of the manuscript follow the same outline as the paper, providing a more in-depth report on the topic with a broader discussion in each chapter.

PART I

STUDY BACKGROUND

Seismology provides an excellent metaphor for scientific research in general - the survey scope of a single "sensor" is limited, but a well-designed "network" having the fundamental advantage of multiple viewpoints may lead to genuinely astonishing discoveries.

Chapter 1:

Essentials of Volcano Seismology

The chapter aggregates information digested by the author from published scientific literature on topic of volcano seismology. Before conducting a new study, it is beneficial to understand **how** ideas about volcanic seismicity nature have evolved over the centuries. It is essential to know **what** convenient seismological tools and methods available nowadays may be applied to investigate a particular volcano. Lastly, it is crucial to recognize **where** similar studies were conducted previously. This chapter is aimed to answer these questions consecutively.

- Section 1.1 provides a concise outline of seismology's roots with the emphasis on its relations to volcanology.
- Section 1.2 presents seismological techniques currently used for volcano monitoring, pointing out their suitability and limitations.
- Section 1.3 highlights some classifications of volcanic seismicity with a discussion regarding existing terminology issues.

1.1: Historical roots

A strong linkage between volcanic eruptions and ground trembling was known to cultures which inhabited active magmatic regions from ancient times. Pliny the Younger, an eyewitness of the Vesuvius catastrophe (79 AD), wrote about numerous associated earthquakes in his letters that virtually became the first scientific report of the eruption (Zobin, 2012). At that time, Greco-Roman philosophers (Thales of Miletus, Anaximenes of Miletus, Aristotle, Lucius Annaeus Seneca) have already abandoned the mythological explanation of earthquakes in favor of the natural law. Based on the chemically simplified tetrad of elements, their hypothesizes about "water", "air", and "fire" trapped inside "earth" influenced European theories until the XVII century. For example, Athanasius Kircher proposed a system of channels inside Earth in 1664, where volcanoes were viewed as ending points on the surface, and earthquakes were explained by the motion of the internal fire working against the rocks that block this motion (Ben-Menahem, 1995). Even nowadays, these concepts are somewhat rational as specific features of volcanic seismicity are related to the interaction of hot magmatic fluid and gases ("fiery mixture of water and air") with rigid enclosing rocks ("earth").

The history of seismology, for the most part, may be viewed as a narrative of earthquake observations: qualitative at the beginning, instrumental with a persistently increasing level of details afterwards. While the early reports of seismic activity have some retrospective value, the first proper observation was made in November 1755 during the catastrophic Lisbon earthquake, described scientifically by John Bevis (1757). Based on this work, John Michell used a popular at that time hypothesis about the subterranean explosion nature of earthquakes (proposed in 1703 by Martin Lister and Nicolas Lemery) to demonstrate that the ground shaking is caused by the waves spreading out from the source throughout the Earth's interior (Hardin, 1966). A century later, this pioneering attempt was followed by Robert Mallet, who studied the Neapolitan earthquake of 1857 in detail. He has conducted systematic analysis by defining an earthquake shock as *"a wave of elastic compression, produced either by the sudden flexure and constraint of the elastic materials forming a portion of the earth's crust, or by the sudden relief of this constraint by withdrawal of the force, or by their giving way, and becoming fractured"* (Mallet, 1848). Mallet published the first world map of seismicity (Mallet & Mallet, 1858) and introduced a common meticulous cataloguing approach which is relevant up today.

Seismology, as a distinct scientific discipline, has emerged in the second half of the XIX century on a theoretical basis of general wave theory and continuum mechanics. The methodological fundament was created by the brilliant physicists and mathematicians of that time: most notably Poisson, Cauchy, Kirchhoff, Rayleigh. The earliest seismoscope was invented in China back in 132 AD by Chang Hêng. However, the global seismology became an instrumental science only in 1889, when Ernst von Rebeur-Paschwitz obtained the first records of a teleseism originated in Japan on his device located in Potsdam (Dewey & Byerly, 1969). Henceforth, many seismological breakthroughs were achieved due to the development of more precise seismographs with a broader frequency range. The series of destructive earthquakes in the late XIX and early XX centuries became a catalyst for seismological studies and initiated the systematic instrumental observations worldwide.

At the beginning of the XX century, tectonic and volcanic seismicity started to be treated differently. The primary efforts were focused in three main directions: understanding seismic wavefield nature, studying Earth's interior structure and creating earthquake source theory. Seismic waves from strong tectonic earthquakes travel through the whole Earth's interior and carry information about its structure recorded in the form of different seismic phases. Thus, it was an obvious choice of data for scientists who worked on large scale problems mentioned above. In contrast, volcanic seismicity typically was studied locally by designated volcano observatories. This fact, coupled with the global diversity of observations, formed a more isolated domain with terminology in many ways unique for each group of scientists.

1.2: Seismic monitoring of volcanoes

It is hard to imagine a volcano observatory without any seismological equipment. Nowadays, most active volcanoes are monitored by the designated observatories equipped with several types of geophysical instruments. Among them, measuring ground vibration can be considered the most traditional way of instrumental volcano monitoring. The first volcanic observatory founded in 1847 on Vesuvius started to record seismicity just a few years later using the Palmieri electromagnetic seismograph installed in 1862. Following the rapid development of seismological instruments in the late XIX and early XX century, volcano observatories worldwide incorporated seismic observation into the standard monitoring routine. Some, like Hawaiian Volcano Observatory, founded in 1912, had to upgrade instruments over time. However, in many cases (Asama Volcano Observatory established in 1934, Kamchatka Volcano Observatory created in 1946), an observatory was equipped by continuously operated seismographs from its inception.

The development in volcanic seismicity observations follows two principal trends: increasing the number of instruments and widening their frequency range. Seismic monitoring in volcanic environments was conventionally carried out using short-period seismometers except a pioneering broadband observation conducted by Kenzo Sassa (1936). He combined Wiechert horizontal-component seismographs (*pendulum period* $T_0 = 10.0$ s) and vertical ones ($T_0 = 4.6$ s), Gallitzin seismographs ($T_0 = 8.0$ s), and short-period seismographs ($T_0 = 0.55$ s) to extend the limited frequency range of instruments available at that time and take a 'wider' look on the seismicity of Aso volcano in Japan. However, in the next half-century, there were almost no similar attempts. Only in the '90s, the advent of modern portable broadband instruments reinvigorated volcano seismology with significantly more informative observations.

1.2.1: Single station

There are several leading volcanic observatories relying on seismic networks equipped with dozens of instruments. However, for some remote locations general principle 'better one than nothing' still applies since even one seismograph can provide important information about the volcanic system's state. The basics of a single-station approach are included inside more sophisticated seismic monitoring methods that use multiple receivers – therefore, it is reasonable to start this overview from the simplest case.

Amplitude analysis

The *real-time seismic amplitude measurement (RSAM)* technique, developed in the US Geological Survey (Endo & Murray, 1991), is a classic approach that quantifies the seismic energy release rate. Initially, it was designed as an A/D converter for analogue telemetry to reduce the size of storing data on the computer by averaging absolute amplitudes of a seismic trace in a sliding window:

$$u^{\text{rsam}}(t) = \frac{\Delta t}{T_{\text{rsam}}} \sum_{k=-T_{\text{rsam}}/\Delta t}^0 |y(t + k\Delta t)| \quad (1.1)$$

where $y(t)$ is the initial seismic signal sampled with the discretization step Δt , and T_{rsam} is the averaging time interval (in the original RSAM system equal to 1- or 10-minutes). This simple approach has proven to be an effective tool for highlighting changes in seismic activity dynamics, as one can find out by examples of the eruption sequence at Mount St. Helen (*Figure 1.1*) and at Redoubt volcano in Alaska (Chouet et al., 1994; Power et al., 1994). Both the initial massive phreatic eruption and the dome-destroying explosion were preceded by a steep acceleration in the energy release rate noticed on RSAM records and contributed to the successful forecasting of these two eruptions (Brantley, 1990).

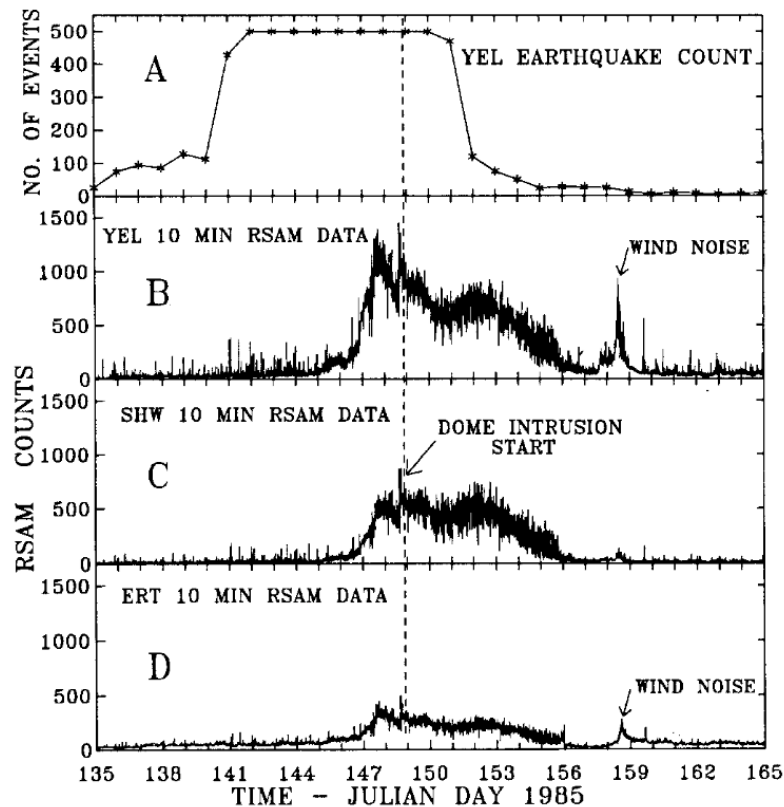


Figure 1.1 - A comparison between manual counting and automated RSAM monitoring for the dome building eruptive episode at Mount St. Helen from 15 May (Julian day 135) to 14 June (Julian day 165), 1985. (A): Plot of manual daily counts for seismic events recognized as earthquakes on station YEL analogue seismogram. (B): Plot of 10-min RSAM data for station YEL. (C): Plot of 10-min RSAM data for station SHW. Although SHW is located about 3 x the YEL distance from the dome, the SHW 10-min plot mimics the YEL 10-min plot. (D): Plot of 10-min RSAM data for the ERT seismic station. After Endo & Murray (1991).

The *reduced displacement* is another observational parameter based on the similar idea. The principal difference is a correction for geometrical spreading. Proposed by Keiiti Aki and Robert Koyanagi (1981), it requires an assumption on the source distance and seismic wave type (Wassermann, 2012). The implied type defines the correction term for *body* and *surface waves*, respectively:

$$u^{\text{rdb}}(t) = \frac{l}{2\sqrt{2}} \frac{\tilde{y}[t - T_{\text{rd}}, t]}{y^*} \quad (1.2)$$

$$u^{\text{rds}}(t) = \frac{\sqrt{\lambda l}}{2\sqrt{2}} \frac{\tilde{y}[t - T_{\text{rd}}, t]}{y^*} \quad (1.3)$$

where l is the distance to an assumed source location and λ is the surface waves dominant wavelength, y^* is the instrument magnification and \tilde{y} is the *peak-to-peak amplitude* of $y(t)$ in a $[t - T_{\text{rd}}, t]$ window. This approach is more sophisticated than RSAM but has its shortcomings, the main one being neglect of the strong scattering, which is frequently observed at volcanoes and may significantly alter amplitude-distance relation. However, this empirical approach delivers valuable information for a general understanding of the magmatic process as such a parameter provides an overview of the volcano dynamic in a wide timescale. In the same article, Aki & Koyanagi utilized the developed reduced displacement parameter to analyze tremor activity beneath Kilauea, Hawaii, on an 18-years cumulative plot (Figure 1.2). Moreover, the reduced displacement may be used to compare seismicity's temporal characteristics of different volcanic eruptions to reveal scaling and constraints, for example, on the conduit size (McNutt & Nishimura, 2008).

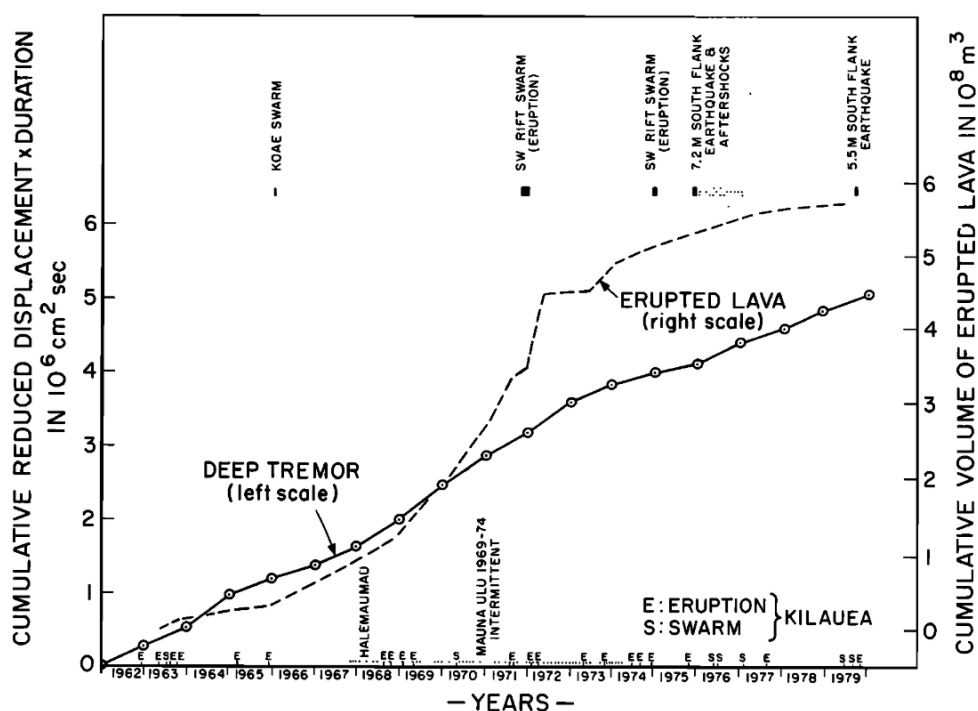


Figure 1.2 - Cumulative reduced displacement plotted for the 18-year period from 1962 to 1979, with major seismic events and cumulative volume of erupted lava, Kilauea, Hawaii. After Aki & Koyanagi (1981).

Polarization analysis

The single-station monitoring, evolving further from the simplest case of recording only one seismic signal component (typically being vertical), naturally transforms into the *three-component (3C)* case. The addition of two orthogonally positioned (typically being horizontally oriented as N-S and W-E) receivers not only triples the volume of recorded data but also allows one to perform polarization analysis. In application to volcanic seismicity monitoring, the arguments for using this approach are based on the predominantly shallow depth of events – thus, an abrupt change in the active source position will be reflected as a substantial variation in the incidence angle and azimuth.

The main drawback at this point should be clear: the undeniable path effect. The volcanic environment's extremely high heterogeneity substantially complicates seismic monitoring and imaging in general, but for the polarization analysis in particular, the path effect impact on results may be devastating. The wavefield radiated from a volcanic source is a mixture of many wave types produced by a complex source, which then travelled through strongly scattering media (Chouet et al., 1997; Goldstein & Chouet, 1994). While it affects all seismic signal features, polarization is likely the most vulnerable one and should be treated very cautiously as a sole source of information. However, a careful examination focusing on basic parameters (*incidence angle*, *azimuth*, and a measure of the *components rectilinearity*) may help identify changes in the volcanic system state.

The path effect problem can be mainly solved using a broadband seismic station located close to an active vent. Polarization analysis made in the near field has a significantly higher quality of source estimation because of a smaller propagation path influence. Unfortunately, the complicated source mechanisms are still at play for the bigger part of volcanic seismicity. If the usual assumption of a point source is not valid, the observed polarization patterns are practically uninterpretable. Besides, the nearly unknown influence of the volcano's topography on signals with a wavelength comparable to the topographical features complicates interpretation even more (Neuberg & Pointer, 2000). However, in some cases, under the assumption of a simple source mechanism, a reasonably good estimation of the source region could be made like it was performed at Stromboli volcano with just a single 3C broadband station (Kirchdörfer, 1999) and Merapi volcano using the network of such instruments (Hidayat et al., 2000).

As a monitoring system part, the estimation of the polarization parameters requires automation. Various approaches may extract necessary information from continuous seismic records: most are based on the least-square fit of the 3D-trajectory of the seismic vector to a 3D-ellipsoid (Wassermann, 2012). Typical algorithms consist of the eigenequation solving and simultaneous search for the eigenvector orientation corresponding to the largest eigenvalue (Flinn, 1965; Montalbetti & Kanasewich, 1970).

Spectral analysis

A seismic signal is recorded as a time series in which each sample represents the value of ground velocity or acceleration. As for almost any time series, one can apply well-developed mathematical apparatus, in which *Fourier transform (FT)* remains one of the key tools. Computing FT for an isolated signal basically provides an image of the said signal from another mathematical dimension – the frequency domain. Signal representation in this dimension is called its *spectrum*, which, strictly mathematically speaking, is a combination of phase and amplitude spectrums. Analysis of the phase spectrum has its value in some applications, but the phrase ‘spectral analysis’ usually implies an inspection of the amplitude spectrum. In many cases, such representation better highlights signal features, especially if the process has a harmonic character. As the very nature of seismic waves involves repeated oscillation of stress and strain around a mechanical equilibrium at a specific frequency value, its implementation in seismology was practically unavoidable.

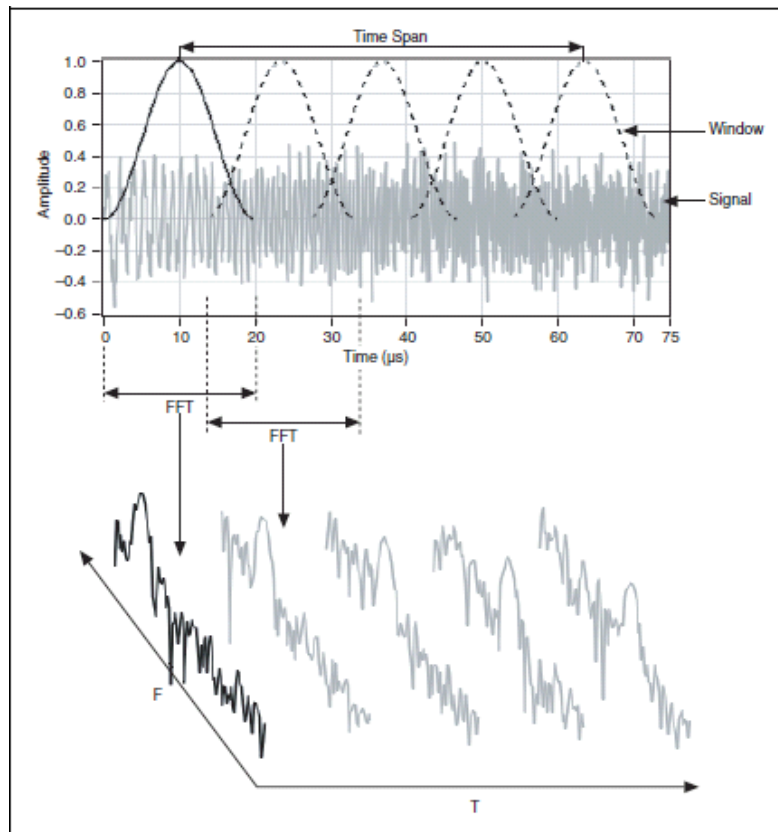


Figure 1.3 – Spectrogram computation process using STFT for windowed segments of the signal. Example courtesy of NI zone.ni.com/reference/en-XX/help/370371K-01/smtlvconcepts/guid-295d927b-4a07-4592-a34b-c4fe1c1b5d33/

Spectral analysis gradually became an essential instrument in the seismologist toolkit. In this regard, computation of the *cumulative power spectral density* for the chosen frequency band may be considered an intermediate step up from the basic amplitude analysis. For monitoring purposes, it is better to use its detrended version (Wassermann, 2012, p. 24) to avoid fast saturation, and estimation

of the cumulative power slope should be done when the volcano's activity is on its baseline. Moving towards a more informative representation of the continuous seismogram in the frequency domain, one may find different techniques for computing the amplitude spectrum. Methods well-suited for efficient (or analogue) processing accomplish it by using *filter banks* (see Chapter 6 in Mertins, 1999). Alternatively, many modern approaches, like Seismic Spectral Amplitude Measurement (SSAM, Rogers & Stephens, 1995), rely on *fast Fourier transform* (**FFT**, Cooley & Tukey, 1965) or *short-time Fourier transform* (**STFT**, Qian & Chen, 1996). The rapid development of computers nowadays allows the implementation of even more computational-costly techniques in real-time monitoring. Besides monitoring purposes, spectral analysis is highly useful for signal discrimination. In fact, it is so powerful that most classifications of volcanic seismicity are based on signal depiction in the frequency domain along with its overall duration and shape in the time domain [e.g., Section 1.3, *Figure 1.8*].

Signal decomposition into two-dimensional (**2D**) *time-frequency* space is the most meaningful way to analyze its time-varying spectral content. For example, a bank of band-pass filters is traditionally used in analogue processing to produce a *spectrogram*. In this case, the input signal is divided into frequency bands, and the magnitude of each filter's output represents a spectral amplitude value for the central frequency. An alternative approach is more common in digital processing: successive computation of signal's FT using sliding window techniques, such as the STFT, which calculates FT over a small, overlapping time window. Thus, plotting a changing spectrum as a function of time will also yield a spectrogram. Seismogram format may vary, but the most common is a 2D image where x and y axes represent time and frequency, respectively, and the color or intensity of the point depicts the amplitude of a particular signal frequency at a particular time moment [e.g., *Figure 1.4*, *Figure 1.8*].

Results of spectral analysis using standard sliding window Fourier techniques, however, suffer from two significant drawbacks. First, the basis for standard FT is constructed of sine and cosine functions that have the infinite non-localized reach. Thus, such a transform fundamentally provides only an averaged representation of a whole seismogram without information about local concentrations of energy and cannot fully represent sharp changes and transient features that are signature to the majority of seismic events. It results in insufficient time-frequency localization of the onset, phase arrivals, and generates spurious harmonics (Bowman & Lees, 2013). The second issue relates to the required segmentation of a signal into windows of fixed length. It leads to the time-frequency trade-off, which is applied to the whole spectrogram, essentially making this representation vulnerable to plotting parameter changes. Longer time window more accurately determines spectral components of a signal extending the spectrogram trustworthy frequency range but changes the time domain resolution leading to 'smearing' (Tary et al., 2014). Conversely, short windows provide

relatively better time resolution but at the cost of lower frequency discretization that truncates the overall determinable spectral range (Chakraborty & Okaya, 1995).

There is a vast choice of alternatives to FT that are based on wavelet transform: many of them are better for spectral analysis of seismicity in general, and some are excellent for the case of volcano-seismic signals in particular. Wavelet-transform analysis being originally invented for seismic signal analysis in the '80s (Goupillaud et al., 1984; Grossmann & Morlet, 1984; Morlet et al. (part I and II), 1982) is hardly a novel technique in geophysics. It gained immense popularity in applications throughout science and engineering after remarkable development and research in mathematics during the '90s (Daubechies, 1992). Surprisingly, the application of wavelet decomposition for spectral analysis of broadband volcano-seismic signals is still limited to a small number of studies (e.g., Bartosch & Seidl, 1999; Lapins et al., 2020; Lees & Ruiz, 2008). Signal non-stationarity, wide-varying frequency scales of interest, and the importance of transient feature localization are severe arguments for this approach utilization. Sadly, most observation-oriented studies in volcano-seismology are still using the 'default' FT approach, probably due to mental inertia, diminishing our understanding of the underlying process. A striking visual example of the difference in data representation is shown in *Figure 1.4*.

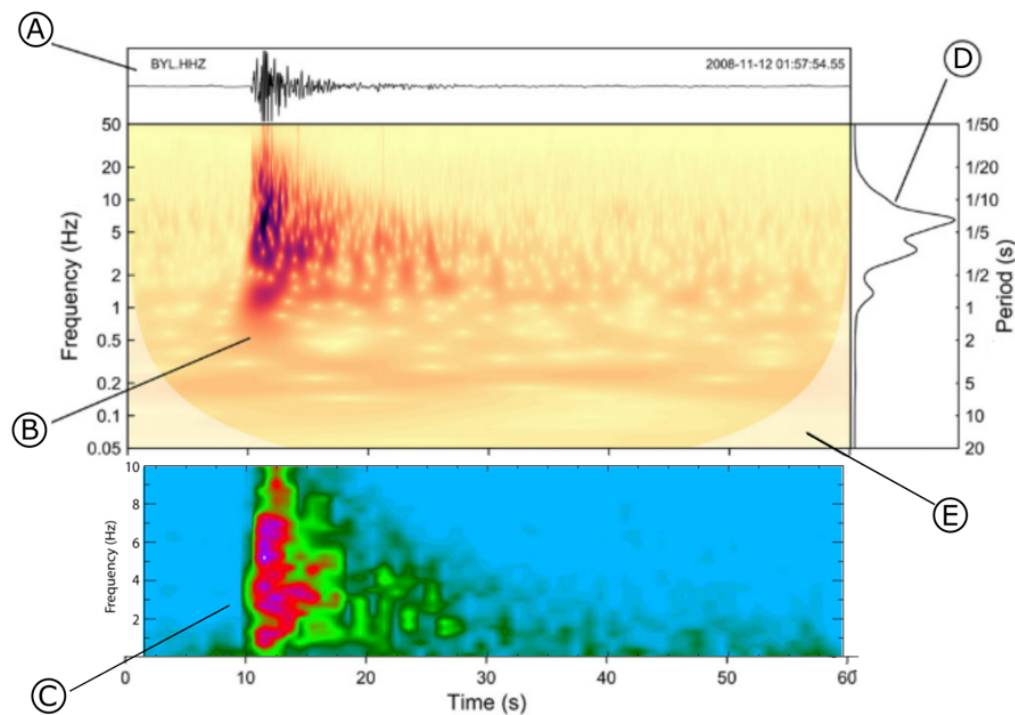


Figure 1.4 – A comparison between traditional spectral analysis and continuous wavelet transform (CWT) version in visual representations for the same volcano-tectonic earthquake signal recorded at Kilauea, Hawaii. (A): Seismogram used for both decompositions. **(B):** Scalogram (logarithmic scale) obtained by CWT that sharply highlight transient features of the signal not sacrificing resolution in the frequency domain. **(C):** Spectrogram (linear scale) obtained using standard STFT that has fixed time-frequency resolution. **(D):** Average wavelet energy distribution (average energy across all time points at each wavelet scale). **(E):** Potential edge effect at each wavelet scale ('cone of influence'). Modified after Lapins et al., (2020) and McNutt & Roman, (2015)

1.2.2 Networks and arrays

A set of seismic stations has two main advantages comparing to a single station. First is the increasing amount of acquiring data, which is useful for said data quality assessment. The second advantage is the fundamental ability to localize seismic events, which opens possibilities for earthquake parameter estimation and examination of the study region. This section contains a brief overview of seismological methods utilizing these advantages to investigate magmatic systems and its evolution in time. A typical seismic network at a well-monitored active volcano nowadays usually consists of at least four to six permanent seismic stations distributed in various azimuths and distances from the volcanic center (Wassermann, 2012). Some notable volcanoes have denser networks: Kilauea, Etna, Colima, Aso. Another approach is to use a regularly spaced set of (typically short-period) seismographs called a seismic array. The network of seismic arrays is a more cost-efficient combination, which has advantages of both observational schemes.

The traditional approach for earthquake location

The earthquake epicenter triangulation technique is pretty well-known even among non-specialist: timing the difference between P- and S-wave arrival (S-P time interval) on at least three stations; translating it to the distance using standard travel-time curve plot; triangulation of the epicenter by plotting resulted distances as a circle around each respective station. It is a good school exercise that can be done in a paper notebook, however, not suited for serious seismological research. In this regard, even the standard seismological approach for earthquake location estimation utilizes a modern PC. Its main strength and weakness at the same time is manual picking of seismic phases: P- and S-wave onsets are selected visually by a qualified and experienced seismologist. Then the inversion for the source location and origin time is frequently done using algorithms like HYPO71 (Lee, 1985). However, most of the standard hypocenter determination programs are based on the assumption of a simple horizontally layered half-space or models with linear gradients of velocity and no topography account. Existing approaches that are not restricted to 1D or 2D models perform localization of the source in a non-linear, probability-based manner but still fundamentally requires a well-defined 3D velocity model (Lomax et al., 2000).

For global-scale seismology based on high-magnitude tectonic earthquakes, such limitations are negligible since even PREM (Dziewonski & Anderson, 1981) provides the sufficient velocity model. However, the lack of satisfactory velocity models for many monitored volcanoes strongly biases earthquake locations, especially when focusing on shallow events. The obtained source coordinates should be seen just as an approximation of true hypocenters. On a good note, relative earthquake locations can be further utilized in minimization of observed and theoretical travel-time differences

(or double-differences) for pairs of earthquakes at each station while linking together all observed event-station pairs (Waldhauser, 2000). Moreover, the presence of multiplets with similar waveforms in data can significantly improve final earthquake location results (Ratdomopurbo & Poupinet, 1995).

Seismic tomography

Seismic tomography is a method for reconstruction of a continuous distribution of seismic parameters in 1D, 2D, 3D, or 4D (space and time) using the characteristics of seismic waves traveling between sources and receivers (Koulakov & Shapiro, 2021). The targeting seismic parameters to be found in tomographic inversion are, in most cases, velocities of *primary (P-)* and *secondary (S-) body waves* (V_p and V_s velocities), but it could also be P- or S- waves attenuation. Additionally, tomography methods can be described in terms of utilized seismic waves (body, surface) or ambient noise), scale (teleseismic, local), observational schemes (active, passive), and the data source nature (specific earthquake type or ambient noise). Thus, the full method description utilized for a study may sound like "body-wave local seismic tomography with active observational scheme" or "ambient noise surface-wave tomography", which directly conveys a message about a certain aspect of the chosen method. Undoubtedly, a particular approach or technique may be unique in implementation, but such precise terminology is useful for understanding what method was used in a study.

There are two reasons why seismic tomography is so applicable in a magmatic environment on several scales. First is the actual data availability necessary for non-ambient noise tomography - volcanic seismicity itself may be used to study seismic parameters of the geological object where it was originated. Mathematically any tomographic technique heavily relies on ray coverage to illuminate the region of interest. Active volcanoes are perfect in the way that distribution of seismicity in space may be sparse enough to produce sufficient rays-angle coverage while being simultaneously dense enough in time to generate a significant amount of data during a short period of observations. The second reason for seismic tomography success lies in targeted parameters. The ratio V_p/V_s between seismic P- and S- body wave velocities of is a critical metric used to evaluate the content of fluids and melts. The *attenuation* of P- and especially S-wave may also give important information on magma sources beneath volcanoes.

There are numerous articles on the topic, presenting cases where tomography was applied to investigate volcanic or magmatic structures successfully. An outstanding example recently published in Science demonstrates that the magmatic reservoirs of present (non-eroded) super volcanoes can be formed as large sill complexes and supports the concept of the long-term incremental evolution of magma bodies that lead to the largest volcanic eruptions. Kairly Jaxybulatov, with a group of colleges, discovered an anisotropy anomaly below the Toba caldera using ambient-noise seismic tomography (Figure 1.5). They interpreted it as a fine-scale layering of large partially-molten sill complexes

(Jaxybulatov *et al.*, 2014) - a “pancakes” able to store vast amount of magma. These complexes are shaped in such a manner due to the pressure gradient that forces magma to move in lateral direction, forming observable anisotropy anomaly.

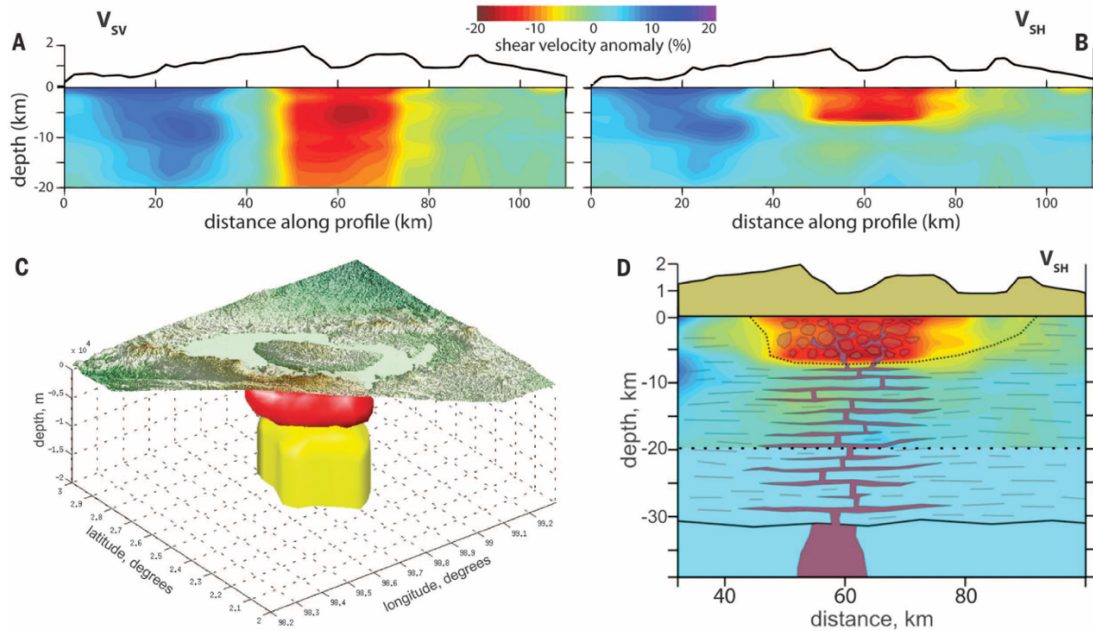


Figure 1.5 – 3D shear velocity model below the Toba caldera and its interpretation. (A): Distribution of V_{SV} in vertical cross section along the profile crossing volcanic complex. The topography is vertically exaggerated. (B): Similar to (A), but for V_{SH} . (C): 3D iso-surface representation of the tomographic model. Red surface, low ($< -10\%$) average speed anomaly; yellow surface, region with strong ($> 10\%$) radial anisotropy [$\xi = 2 \times 100 \times (V_{SH} - V_{SV}) / (V_{SH} + V_{SV})$]. Vertically exaggerated topography is shown on the top. (D): Schematic interpretation of the velocity structure for the Toba caldera complex superimposed on the distribution of the V_{SH} (shown above 20 km in depth). The anisotropy below 7 km in depth appears to be due to a layered magmatic intrusion dominated by horizontally oriented sills. Dotted line, the low-velocity area below the caldera that might have been affected by the super-eruption 74,000 years ago and where the horizontal stratification would not be preserved. From Jaxybulatov *et al.*, (2014)

1.3 Classification of volcano-seismic signals

Seismic monitoring has proven to be a powerful tool for volcanological applications as magmatism manifestation includes characteristic volcanic seismicity. Ideally, one would like to categorize seismicity based on its genesis, but the diverse range of seismic records at different volcanoes reflect a whole spectrum of physical processes with various parameters. Contrary to studies of conventional tectonic earthquakes, volcano seismology mostly remains the science of observation and cumulative experience. We are used to describing volcanic seismicity in terms of its duration, frequency content, and sometimes depth, but rarely in terms of its source mechanism or the nature of underlying processes. Besides, it is not always clear that the same physical mechanisms cause similar signals; therefore, many volcanic observatories follow their unique way of naming certain seismic events.

Even with the broad definition of a volcanic earthquake as ***"seismic disturbance, which is due to the direct action of the volcanic force, or one whose origin lies under, or in the immediate vicinity of, a volcano, whether active, dormant, or extinct"***, Fusakichi Omori (1912) already mentioned two categories: the earthquakes not simultaneously accompanied by an eruption and those caused by more or less explosive eruptions. One of the first attempts to classify volcanic seismicity was made by Takeshi Minakami (1961), who divided earthquakes originated from Asama volcano into four types (type-A, type-B, explosion quakes, and volcanic tremor) based on their foci location and relation to the eruption. Minakami's classification (*Figure 1.6*) was later applied to volcano-seismic signals observed on other volcanoes in Japan and the Pacific region (Minakami, 1974) and it is considered traditional nowadays. Another pioneering work in categorization was done in Kamchatka by Pavel Tokarev (1966), who divided volcanic seismicity into five types (ranging from type-I to type-V) according to the nature of ground motion and expected movements of magma. The subsequent discussion in the volcano seismology domain, however, mostly follows works, in which proposed categorization is more figurative than rather generic terms like 'type-A' earthquake or 'type-I' event (Chouet, 1996, 2003; Chouet & Matoza, 2013; Lahr et al., 1994; McNutt, 1996, 2005).

In this section, one may find yet another attempt to group volcano-seismic signals according to the degree of complexity and knowledge about corresponding sources, which reflects the author's understanding on the subject. The basis for this summary were the book "Introduction to Volcanic Seismology" by Vyacheslav Zobin (2012) (*Figure 1.7*) and Chapter 59 "Volcano Seismicity" of "The Encyclopedia of Volcanoes" written by Stephen McNutt & Diana Roman (2015) (*Figure 1.8*).

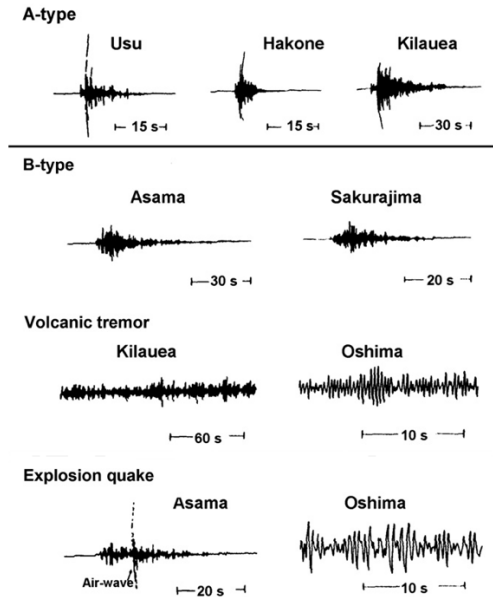


Figure 1.6 – Seismograms of different volcanic seismicity types in the classification of Takeshi Minakami. The nature of A-type earthquake motions is similar to those of the shallow tectonic earthquakes. The P- and S-phase of seismic waves are clearly defined. B-type earthquake motions consist mainly of vibrations with periods in the range from 0.2 s to 1.0 s (1-5 Hz). The surface waves are predominating, and the S-phase is not clear. Explosion quakes, accompanying individual explosive eruptions, have amplitudes proportional to the eruption kinetic energy. Seismograms show initial motion as “push” in every direction and often complicated by air-shocks wave. Volcanic tremor has a form of an irregular sinusoid of rather long duration compared with earthquakes of the same amplitude. Various wave forms are found in volcanic tremors, including surface waves of Rayleigh and Love type. Modified after Minakami (1974).

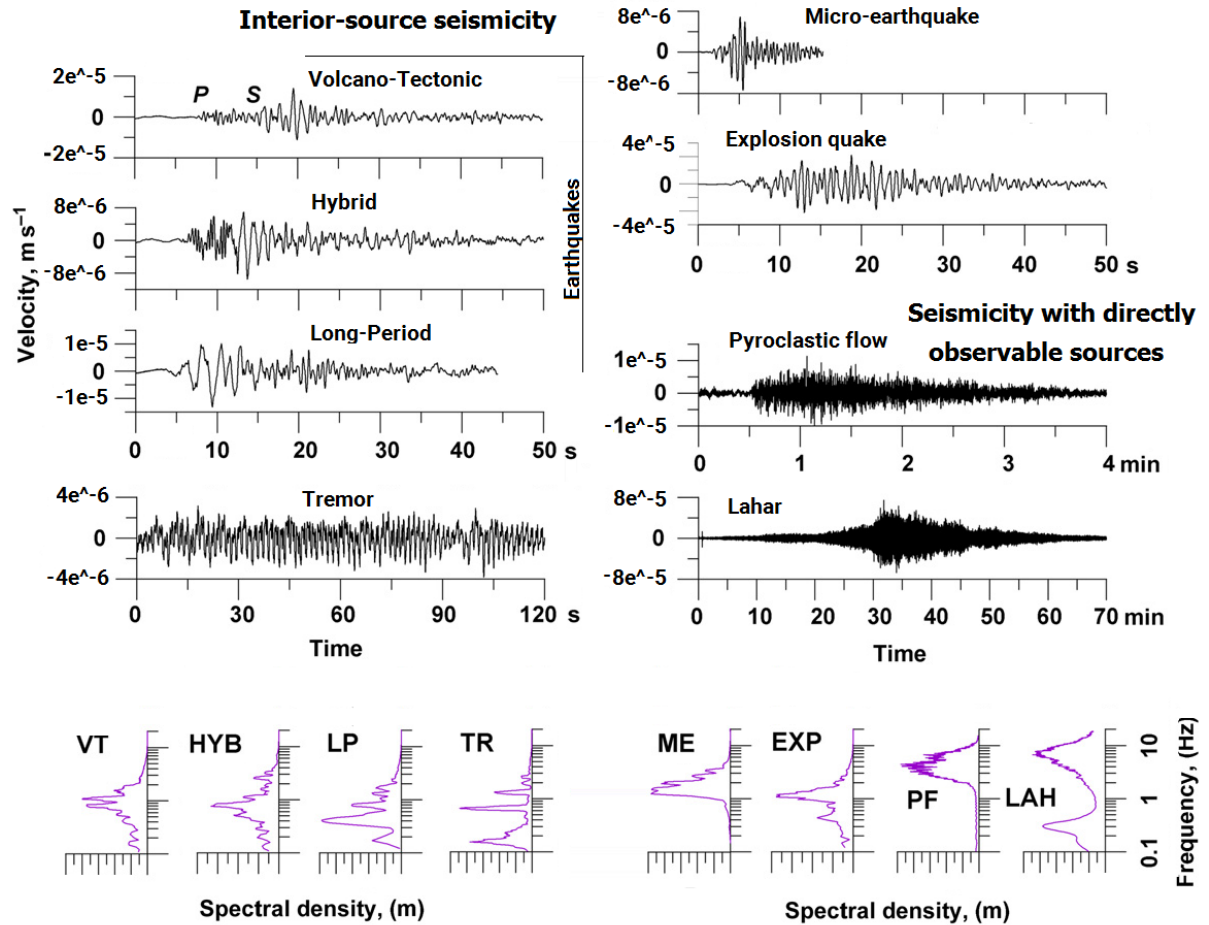


Figure 1.7 – Colima Volcano Observatory classification. (Top part): types of seismic signals (velocity, vertical component) recorded during the 1998-2011 unrest at andesitic Volcan de Colima. (Bottom part): corresponding Fourier spectra. All seismic signals were recorded by broadband seismic station at a distance of 4 km from the crater and corrected for instrument response. Modified after Zabin (2012).

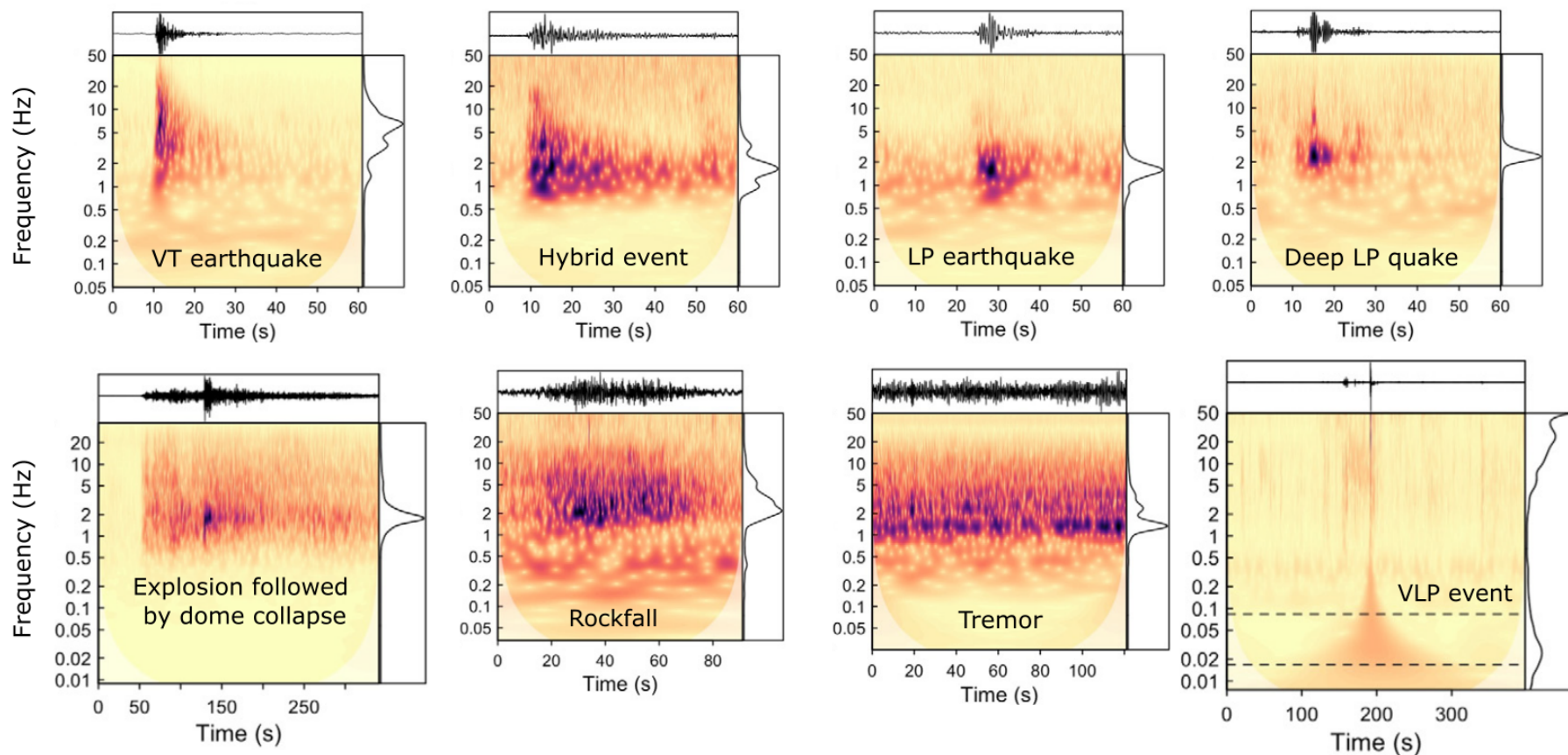


Figure 1.8 – Volcanic seismicity classification mentioned in the *Encyclopedia of Volcanoes (second edition)* Chapter 59 “Volcanic seismicity” written by McNutt & Roman, (2015) and presented here using CWT spectral decomposition shown on Figure 1.5. Each figure shows waveforms and scalograms: **Volcano-tectonic (VT) earthquake recorded at Kilauea volcano, Hawaii (Data courtesy HVO). **Hybrid event** recorded at Mount St Helens, Washington (Data courtesy CVO). **Long-period (LP) earthquake** recorded at Shishaldin volcano, Alaska (Data courtesy AVO). **Volcanic tremor** recorded at Kilauea volcano, Hawaii (Data courtesy HVO). **Deep long-period earthquake** recorded at Akutan volcano, Alaska (Data courtesy AVO). **Explosion earthquake followed by a dome collapse** at approximately 130 s recorded at Soufrière Hills volcano, Montserrat (Data courtesy MVO). **Rockfall** event recorded at Soufrière Hills volcano, Montserrat (Data courtesy MVO). **Very long-period (VLP) event** recorded at Fuego volcano, Guatemala (Data courtesy of G. Waite.). All signals have been bandpass filtered between 0.1 and 10 Hz, with the exception of VLP event, which was bandpass filtered between 60 and 12 s periods. Note different timescales and frequency scales. HVO – Hawaiian Volcano Observatory; CVO – Cascades Volcano Observatory; AVO – Alaska Volcano Observatory; MVO – Montserrat Volcano Observatory. Modified after Lapins et al., (2020).**

Seismicity with directly observable sources

Before diving into a discussion of volcano-seismic signals with less obvious source mechanisms, it is rational to review seismicity with a visible volcanic cause first. Ground vibrations produced by pyroclastic flows and lahars have observable sources directly acting at volcanic edifice during the eruption. Depending on the event's size, the corresponding seismic signal can last up to several minutes with rather large amplitudes exceeding several times those of other volcanic seismicity types (Wassermann, 2012). It is generally dominated by surface waves with the emergent onset and no apparent peak amplitude (Hibert et al., 2011). Seismogram envelopes with spindle shape are typically the main distinguishable feature (Figure 1.9), while observed frequency ranges depend strongly on a study location and relative position of the seismic station to the event (Allstadt et al., 2018).

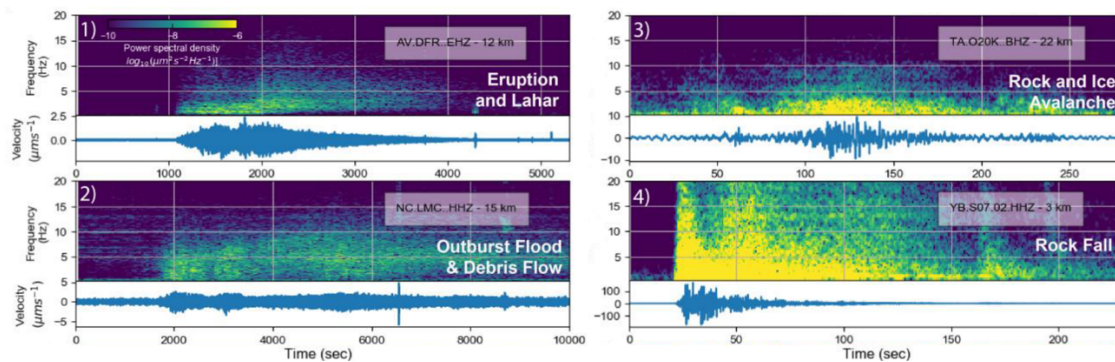


Figure 1.9 – Comparison of different types of seismogenic surface movements on spectrogram and seismograms reported in (Allstadt et al., 2018): (1) 24 March 2009 eruption of Mount Redoubt followed by lahar, starting at ~1900 sec; (2) Mud Creek outburst flood and debris flow at Mount Shasta, CA, in Sept. 2014; (3) Red glacier rock and ice avalanche at Iliamna volcano, May 2016; (4) Rock fall off lava dome during 2006 Mount St. Helens eruption, May 2006.

It is important to note that seismographs installed on volcanoes are recording all surficial events, including those generated by nonvolcanic processes (McNutt & Roman, 2015). Among the most common are landslides and rockfalls, which share the same physical mechanism of a surficial gravitationally driven mass movement with lahars and, to some extent, pyroclastic flows. Several models can approximate it: a relatively simple one more suited for landslides is the sliding block model (Zhao et al., 2015); another one, more fitting for the lahars, is the granular flow model (Mangeney et al., 2010). The signal's emergent character can be explained by the growing nature of the source momentum and size, as it can take time before sufficient material is moving fast enough for the signal to exceed the noise level (Havens et al., 2014; Suriñach et al., 2000).

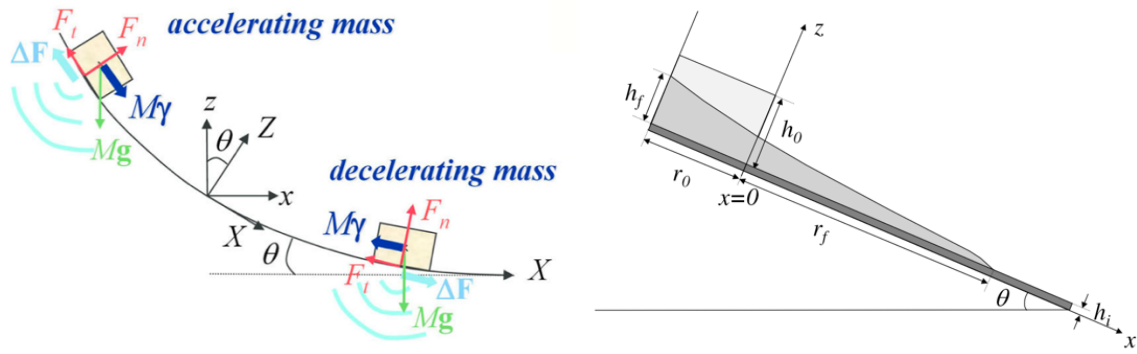


Figure 1.10 – Sliding block and granular flow models of surficial seismicity. Sketch of a rigid block accelerating and decelerating down a slope and associated forces used to describe sliding block model from Zhao et al., (2015) (left). Sketch of morphometric and control parameters measured in the experiments that simulate rockfalls to describe granular flow model from Mangeney et al., (2010) (right).

Volcano-tectonic earthquakes

Volcano-tectonic (VT) earthquake, as the name implies, has a close resemblance to an ordinary tectonic earthquake. Both look similar in the frequency domain but quite different in amplitude. The typical magnitudes of VT is around 3.0 or less, with the maximum sometimes exceeding 6.0 (Toda et al., 2002). Contrary to the usual tectonic seismicity pattern, VT earthquakes tend to occur as a group of many earthquakes clustered in space with no dominant shock, which is called a *swarm*. VT swarms have a more uniform magnitude distribution with the difference in magnitude between the most energetic event and its successor in 0.5 magnitude unit or less, as opposed to 1.0 magnitude unit or more for most mainshock-aftershock sequences (McNutt & Roman, 2015).

Although some researchers subdivide VT earthquakes on deep and shallow ones, this type of seismicity is universally recognized among all classifications of volcanic seismicity even if it is referred by other names like A-type earthquake (Minakami, 1961, 1974), type-I (Tokarev, 1966), or high-frequency events in (McNutt, 1996). The typical seismogram of a deep VT event (with a hypocenter at a few kilometers depth) is dominated by body waves and short exponentially decayed coda (Figure 1.11 a, b). Both P- and S-wave have precise impulsive arrivals with peak frequencies above 5 Hz and a broad spectrum of coda extending up to 15 Hz (Lahr et al., 1994). Shallow VT earthquakes are characterized by more prominent surface waves, less clear P-wave onset, and weaker or sometimes even undetectable S-phase (Figure 1.11 c, d). The strong scattering (especially for higher frequencies) also results in the shift of recorded spectral bands to lower frequencies (Wassermann, 2012). For shallow VT events, a variation in dominant coda frequency with time is noticeable, which is characteristic of a dispersed wavetrain (Lahr et al., 1994). Eventually, both shallow and deep VT earthquakes share the same source mechanism, and the difference in recorded seismic signals may be explained by the path effect, which could be extreme in a volcanic environment.

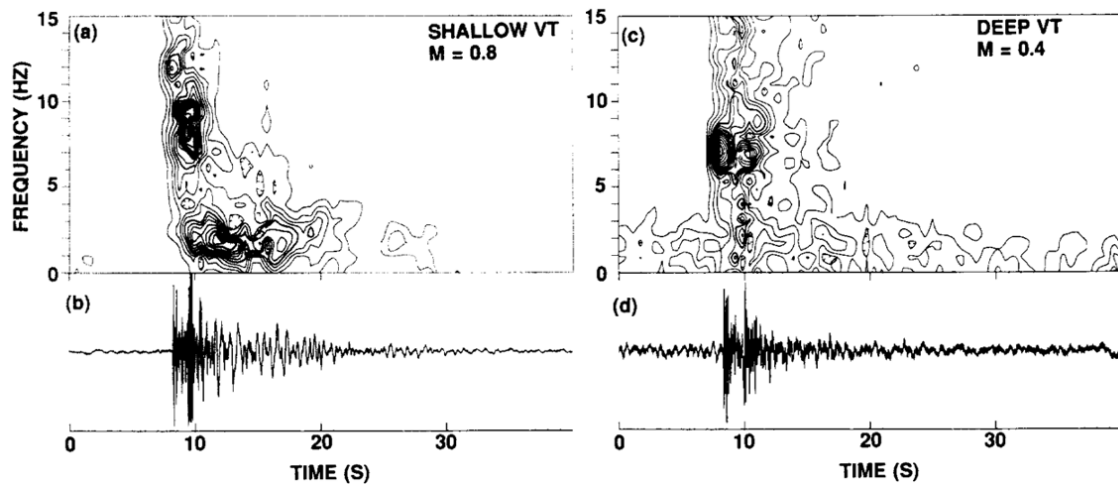


Figure 1.11 – Spectrograms and seismograms for volcano-tectonic earthquakes: shallow VT (a, b) and deep VT (c, d) that were recorded at Redoubt Volcano, Alaska. From Lahr et al. (1994).

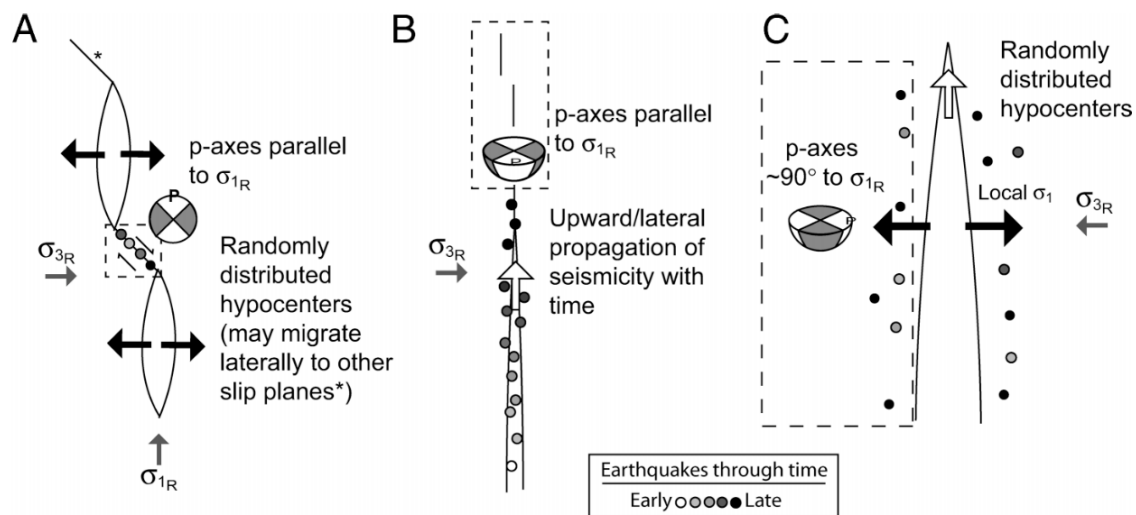


Figure 1.12 – Three models for relationship between magma migration and local VT earthquake swarms, including expected spatio-temporal patterns of earthquake locations and fault-plane solutions. (A): Map view of model by Hill (1977) linking occurrence of VT earthquakes to slip on shear planes extending obliquely from edges of inflating dike. (B): Cross-section view of model by Ukawa and Tsukahara (1996) linking propagation of magma-filled dike to VT earthquakes occurring in zone of inflation-induced tension ahead of propagating dike tip. (C): Cross-section view of model by Roman (2005) linking inflation of dike to occurrence of VT earthquakes with $\sim 90^\circ$ degree rotated fault-plane solutions (relative to regional faulting) in walls of dike. White arrows show direction of magma flow (out of page in A); black arrows show dike inflation (insignificant in B); grey arrows show regional principal stress orientation (σ_1 is out of page in B and C). Shaded dots show earthquake locations through time (darker dots indicate later earthquakes). Dashed box indicates seismogenic region considered in each model. From Roman and Cashman (2006).

Because signals of VT earthquakes are almost indistinguishable from the tectonic ones, they imply the same double-pair source mechanism (Aki & Richards, 1980). In a well-studied tectonic case, an earthquake occurs as a result of abrupt sliding of opposite rock surfaces caused by stress build-up due to large-scale tectonic movements. In the case of a VT earthquake, driving stresses are associated with magmatic processes acting both beneath volcanic structure (deep VT) and within the edifice itself (shallow VT). The crust's pre-existing ambient stress field affects developing magma channels setting

their position and orientation (Nakamura, 1977). Conversely, conduit pressurization or depressurization resulting from magma movement influences local stresses near the conduit generating swarms of VT earthquakes (Roman et al., 2004). Diana Roman and Katharine Cashman evaluated three physical models for VT seismicity proposed for dike-propagation mechanism (Figure 1.12), and concluded that none of the three can explain seismic observations at different volcanoes, probably because each model describes the seismic expression of magma-induced stresses only in a specific area around the propagating dike (Roman & Cashman, 2006).

Long-period seismicity

The main troublemakers in volcanic seismicity classification are various seismic signals that share a main spectral feature – the central part of their energy is concentrated on long periods or, conversely terming, in a narrow low-frequency band. The choice of using 'period' versus 'frequency' terminology is an ambiguous one, as traditional classifications (ex. Minakami's) were created for signals obtained using short-period seismographs and followed typical high- and low-frequency discrimination of seismicity. The current generation of broadband instruments, however, opened possibilities to record ground vibrations at longer periods. Since the part of volcanic seismicity existing at very low frequencies was not mentioned in such classic taxonomies, this discovery encouraged the shift in terminology.

The conventional usage of a period instead of frequency in earthquake seismology is based on the Earth noise peak at approximately 10 s (<0.1 Hz; see Aki & Lee, 2003). The situation in volcano seismology, however, differs from that. A widely accepted notation was proposed by Bernard Chouet (1996) events with a dominant period of about 1 s (<1 Hz) are called 'long-period' (**LP**) events; signals with longer periods are named 'very-long- period' (**VLP**, 2 s to 50 s, 0.5 to 0.01 Hz) and 'ultra-long-period' (**ULP**, >100 s, <0.001 Hz) events. After comprehensive comparison of existing classifications (see table 1 in McNutt, 1996), appealing for consistency in seismology as a whole, Stephen McNutt pointed out the unfortunate choice of period instead of frequency and the need for genetic terms to eventually replace descriptive nomenclature. To this day one may only quote his words about volcano seismology: *"Although a consensus on terminology is desirable, one is not likely to emerge any time soon"* (p. 462, McNutt, 2005).

Since the present thesis is focused on specific application in volcanology rather than a broad scope of seismology, the author chose to use a vocabulary that is more popular in the study domain. It is mainly based on the recent review paper by Chouet & Matoza (2013). A complete understanding of LP seismicity nature could be considered "The Holy Grail" of volcano seismology. Better insight into mechanisms generating such diverse signals will immensely improve our knowledge about volcanic processes behind it. Since the main focus of the present thesis is a systematic analysis of LP events,

the whole next chapter is devoted to the acquaintance with observations and physical models of LP earthquakes.

Hybrid events and explosion earthquakes

Few types of volcanic seismicity possess spectral features of both VT and LP earthquakes, which may indicate a complex source mechanism involved in their generation. Hybrid events have more pronounced high-frequency onsets than LP earthquakes and show a mix of first motions similar to VT ones (Figure 1.13). Their codas, however, are dominated by a non-dispersive harmonic wavetrain that is characteristic of LP events, hence the spectrograms of a hybrid coda and an LP coda are similar (Lahr et al., 1994). Such signal characteristic may reflect a possible coupling of source mechanisms. The succession of high- and low-frequency wavelets in hybrid event signal suggest that a VT earthquake could trigger a LP one nearby and thus source spectrum is mixed on the recorded seismogram. Alternatively, time-frequency differences between these three types (VT → Hybrid → LP) may be due to the path effect (Harrington & Brodsky, 2007).

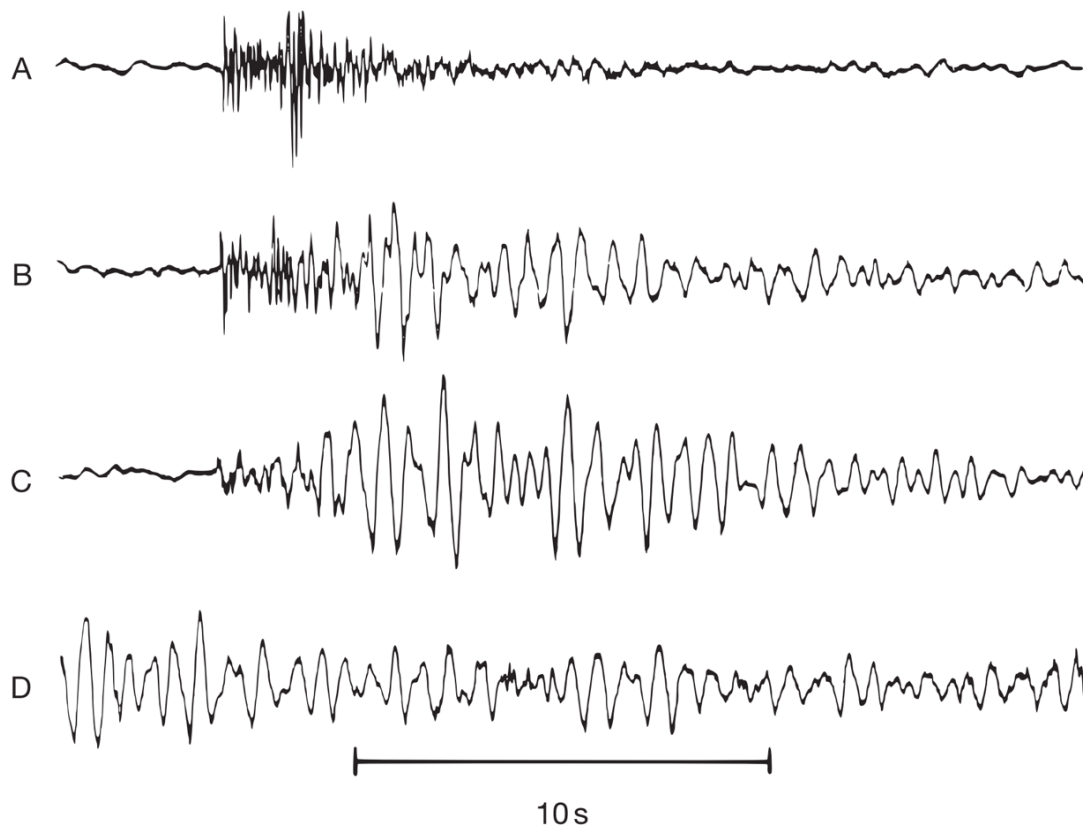


Figure 1.13 – Comparison between volcanic seismicity waveforms: Typical volcano-tectonic earthquake (A), hybrid event (B), long-period earthquake (C) and harmonic tremor (D). All four waveforms were recorded on the same station RED on Redoubt volcano. From Kawakatsu & Yamamoto (2015) adopted from McNutt (1996).

Explosion earthquakes occurring during magmatic, phreatic, or phreatomagmatic eruptions have a clear visual manifestation on the volcano edifice. Despite the fact, this type of seismicity should not be assigned to the first group mentioned in this classification, as the actual source, even being shallow, is still located inside volcanic edifice and cannot be directly observed. The distinguishable air disturbance phase is often seen on seismograms and to study explosion earthquakes, many seismic networks are complemented by infrasonic pressure sensors or calibrated infrasonic microphones (Caplan-Auerbach & McNutt, 2003). Another notable feature of the explosion quake is a sequence of low- and high-frequency wavelets inside full signal (*Figure 1.14c*), which gives a clue about source mechanism operational order.

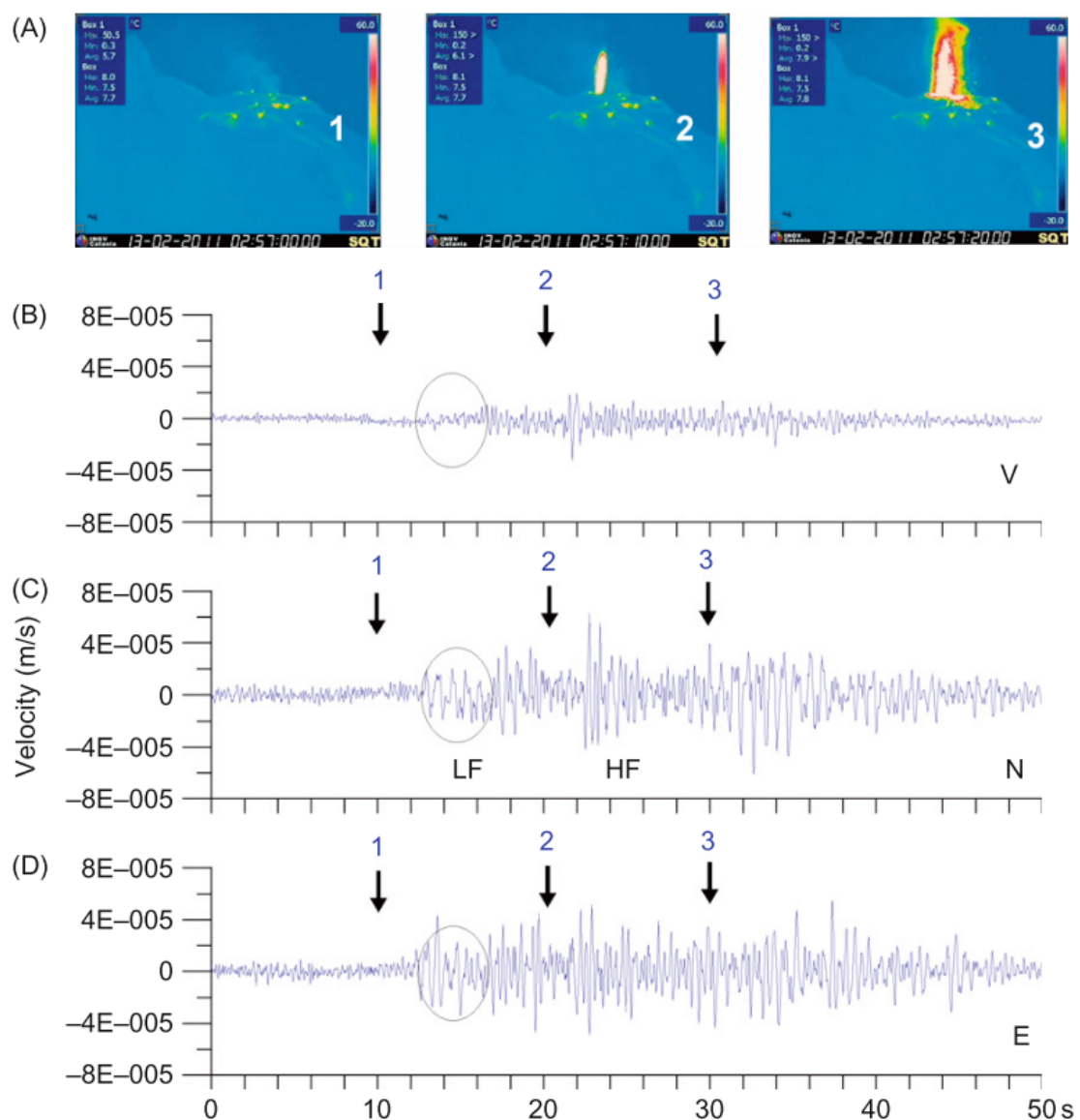


Figure 1.14 – Contemporary video snapshots and 3C broadband seismic records during Stromboli explosion that occurred [13 February 2011, 02:57] at Stromboli volcano. Seismic station was situated at a distance of 0.5 km from the crater. Video station was situated at a distance of about 1 km from the crater. LF and HF indicate low-frequency and high-frequency signals. 1, 2, and 3 correspond to the timing of images and the seismic record. From Zobin (2012).

Chapter 2:

Long-Period Volcanic Earthquakes

Long-period (LP) volcanic seismicity is probably the most intriguing kind of seismic signals widely observed on active volcanoes. In the present thesis, this term unifies several distinct types, that seem to be caused by the same physical process but differs in actual generation's mechanisms as was mentioned in the last section of a previous chapter (Section 1.3). Understanding the origin of LP seismicity is one of the main challenges in volcano seismology. This chapter is not aimed to comprehend its nature as a whole. Instead, the primary focus here is given to a single most common type – *long-period earthquakes (LPs)*.

Even within a scope of the same type, LPs have a wide diversity in an appearance on different active volcanoes. Two main questions arise: *why* we observe such a visual variety of LPs that still have the same key signal features, and *how* it can be possibly generated? Thus, the chapter is structured as two complementary sections to approach the matter, mirroring the universal ‘data-model’ pair:

- Section 2.1 carries an analysis of standard features and significant differences in observations of LP volcanic seismicity.
- Section 2.2 focuses on the discussion about existing physical models explaining various mechanisms of its generation.

Information combined in this chapter gave the author insight into the possible nature of studied signals, essential for interpreting obtained results (presented in PART II).

2.1 Observations of LP seismicity

Short-period seismometers deployed on various volcanoes provided scientists with numerous examples of LP seismicity recorded both as continuous (harmonic volcanic tremor) and discrete (LPs) cases. The current generation of broadband instruments uncovered more intriguing examples of *very-long-period (VLP)* and *ultra-long-period (ULP)* events. Since it is almost impossible to review this wide range of signals in a single text section, only main aspects of LPs observation and its relation to volcanic tremor are presented below.

2.1.1 Key features of a typical long-period earthquake

Typically, LPs share a characteristic signature consisting of a brief high-frequency onset followed by decaying harmonic waveform that contains one or several dominant periods in the typical range of 0.2 – 2 s (frequencies in the range of 5 – 0.5 Hz, Chouet, 1996). Various volcanic systems with diverse geochemical composition produce LPs that have different amplitude and duration (*Figure 2.1*). While these two signal parameters are subject of a seismograph location, the dominant period of the recorded wave coda is generally shared by all stations of the seismic network. It suggests that the coda harmonic nature is a characteristic of the seismic source itself, rather than the path effect.

The decaying nature of LPs coda may be characterized by the *quality factor (Q)* – quantitative parameter of anelasticity, which corresponds the fractional loss of oscillation energy in each cycle at a certain frequency. A smaller value of Q implies stronger attenuation of seismic waves. As some physical models (ex. Kumagai & Chouet, 1999) allow to compute Q theoretically, the analysis of this parameter opens possibilities to compare LPs sources in different volcanic systems.

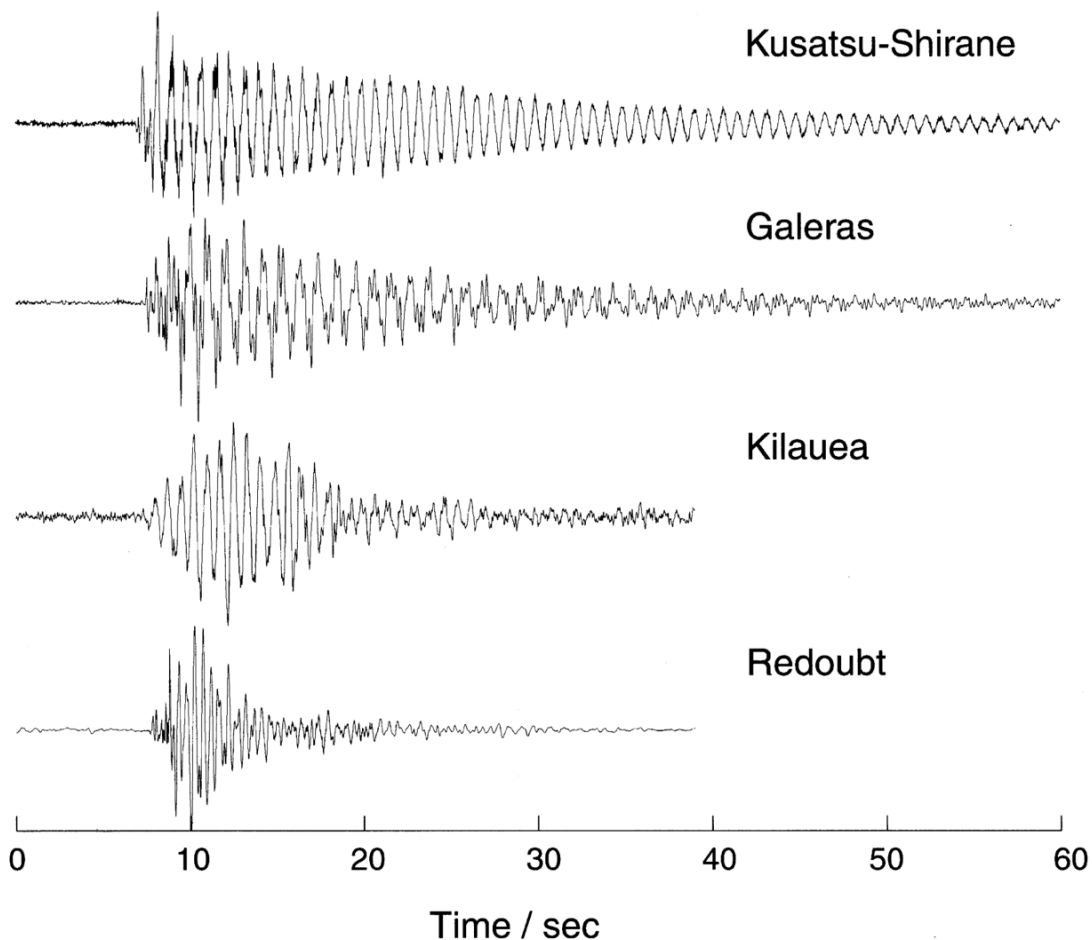


Figure 2.1 – Waveforms of LP events (normalized) observed at Kusatsu-Shirane (Japan), Galeras (Colombia), Kilauea (Hawaii) and Redoubt (Alaska). The waveforms are characterized by simple decaying harmonic oscillations except for a brief time interval at the event onset. From Kumagai & Chouet (1999).

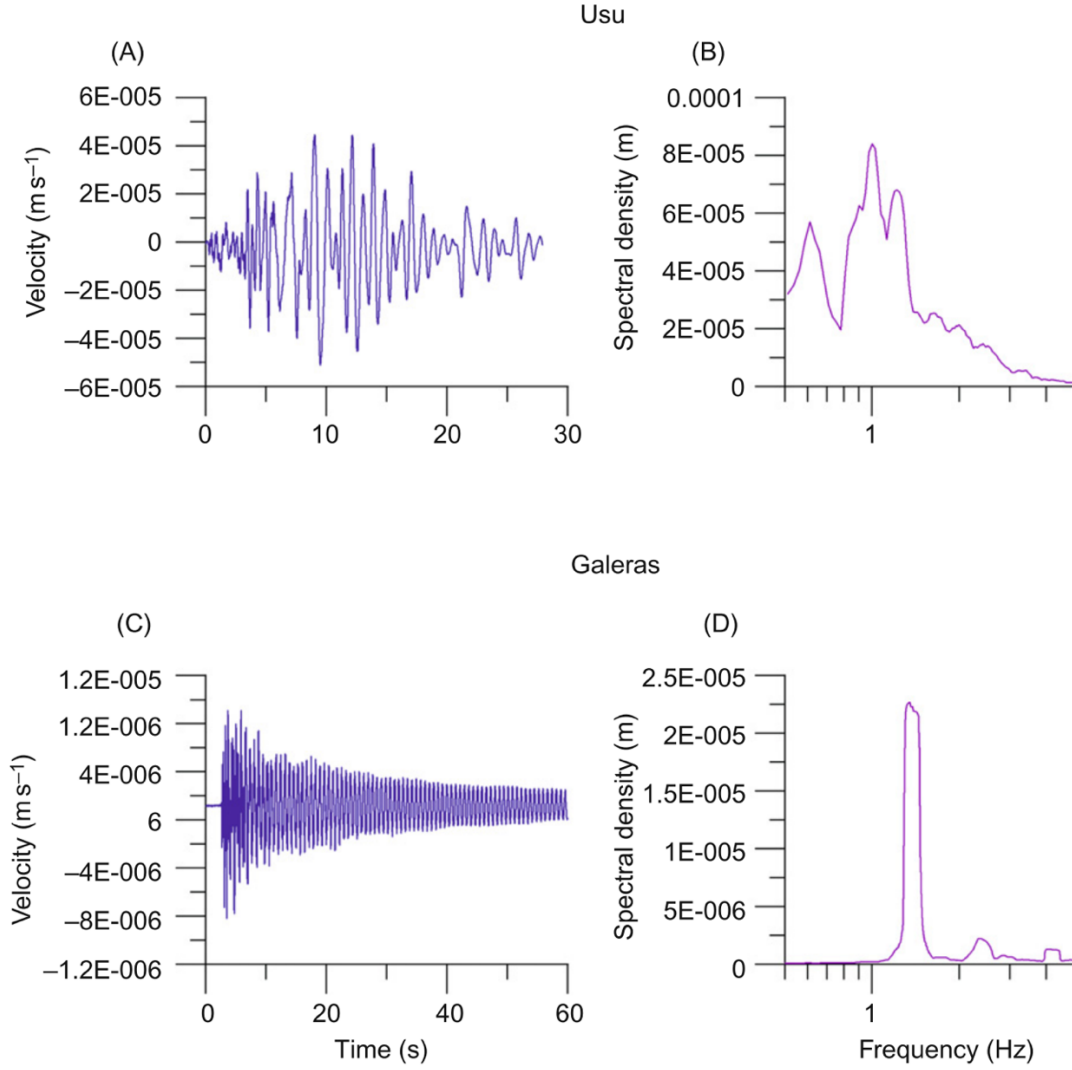


Figure 2.2 - Examples of long-period seismic waveforms and their Fourier spectra. (A): Seismic signal (velocity, vertical component) recorded at Usu volcano on 30 March 2000 and its Fourier spectrum (B). (C): Seismic signal (velocity, vertical component) recorded at Galeras volcano on 1 January 2010 and its Fourier spectrum (D). From Zobin (2012).

In many cases, similar to VT and hybrid earthquakes behavior, LPs occur in swarms, however the situation is fundamentally different in that they appear as a series of repetitive signals with almost identical waveform (Iverson et al, 2006; Kendrick et al, 2014; Matoza et al, 2015). A common representation of the recorded signal in seismology is a convolution of three terms:

$$\mathbf{y}_{\mathbf{r}}(t) = \mathbf{I}_{\mathbf{r}} * \mathbf{G}_{\mathbf{x}}^{\mathbf{r}} * \mathbf{s}_{\mathbf{x}}(t) \quad (2.1)$$

where $\mathbf{y}(t)$ is the seismic signal recorded in location \mathbf{r} by the instrument with $\mathbf{I}_{\mathbf{r}}$ response (for the sake of simplicity it also includes the site effect), \mathbf{G} is the Green function between points \mathbf{x} and \mathbf{r} , and $\mathbf{s}_{\mathbf{x}}(t)$ - is a time-depended function describing the source. Assuming that for signals closely observed in time instrument response and geological media on the propagation path are not changing (therefore no dependence of t for these two terms in the equation above), it is clear that such events must have the same source. This conclusion permits one to stack repetitive waveforms of similar LPs and use

resulted ‘artificial’ wavelet as a *template* representing corresponding *cluster* (also sometimes called ‘family’) of LP events (*Figure 2.3*).

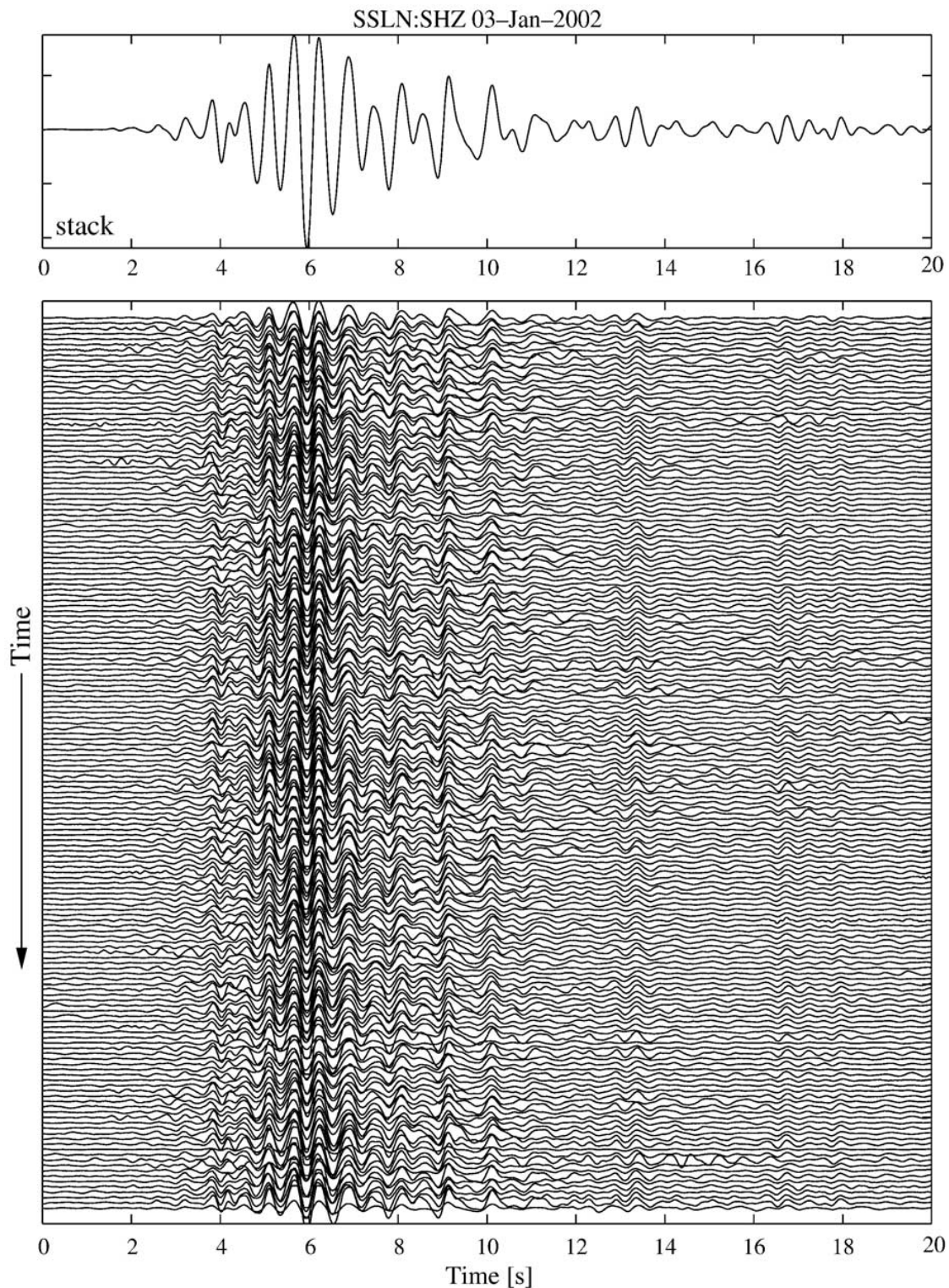


Figure 2.3 – Example of repeating long-period earthquakes at Shishaldin. LP events recorded at station SSLN on January 3, 2002. The cluster was extracted by cross-correlation. The spectral-coherence values for these events are > 0.9 . The upper part of the plot shows a stack of all events in the lower part. The waveform similarity between the events is also seen on other stations. From Petersen et al. (2006).

2.1.2 Character of the volcanic tremor

By *tremor* seismologists used to refer to continuous seismicity with a long duration: it can range from minutes to hours, days, weeks and even months or years in some cases. While there are observations of non-volcanic, *tectonic tremor* (Obara, 2002), this subsection is primarily aimed to review a more prevalent in observation and literature case of *volcanic tremor*. It was included into the traditional Minakami's classification, as well as in pretty much any other, because volcanic tremor is one of the most common types of seismicity associated with active volcanoes. Besides a long duration, shared signal features include generally ambiguous onset and unclear phases. However, volcanic tremors observed worldwide differ in amplitude and duration – both parameters have a several orders of magnitude span. The hypocenter depth also varies in a wide range: from the surface down to about 60 km. Since the frequency content is a special aspect of volcanic tremor observations, it is reviewed in more details below, but the predominant frequency of the onset is usually about 1 – 3 Hz, and the overall frequency range for most cases is 0.5 – 10 Hz (McNutt & Nishimura, 2008).

The terminology issues in LP seismicity analysis are not limited to the naming of discrete events like LPs. Volcanic tremor signals are also termed in a number of ways, that may confuse beginner researcher. In the author's opinion, volcanic tremor may be subdivided into two kinds according to their time-frequency images: *harmonic tremor* and *spasmodic tremor*. The former strongly resembles LPs prolonged in time – the tremor spectra contain several regularly spaced peaks with both odd and even overtones (Lesage et al., 2006). Harmonic tremor generally has a rather stable amplitude in time with a sustained oscillation, however there are special cases of 'banded tremor', where periodic bursts are separated by quiescence of uniform duration (McNutt, 1992). Spasmodic tremor consists of irregular pulses with higher frequencies. It lacks such regularly spaced spectral peaks that defines harmonic tremor, and the appearance of sustained spasmodic tremor is similar to so-called 'broadband tremor'. Some researchers also distinguish 'pulsating tremor' that is close to spasmodic type in appearance but has more irregular signal amplitude in time. In the author's opinion pulsating tremor may be considered a special case of spasmodic tremor, which is in a way mirroring harmonic and banded tremors pair. While all mentioned kinds of tremor represent a more general case of volcanic tremor, spasmodic type leans toward a broadband seismicity, while harmonic tremor shares spectral features with LP seismicity.

The same magmatic system may express various types of volcanic tremor. For example, at Popocatepetl (Mexico) harmonic tremor was associated with lava dome growth, while episodes of spasmodic and pulsating tremor were linked to ash and gas emissions (Arámbula-Mendoza et al., 2016). In this case average amplitudes of harmonic part of volcanic tremor were about one order of magnitude large than lower and intermediate energy spasmodic (pulsating) counterpart (*Figure 2.4*).

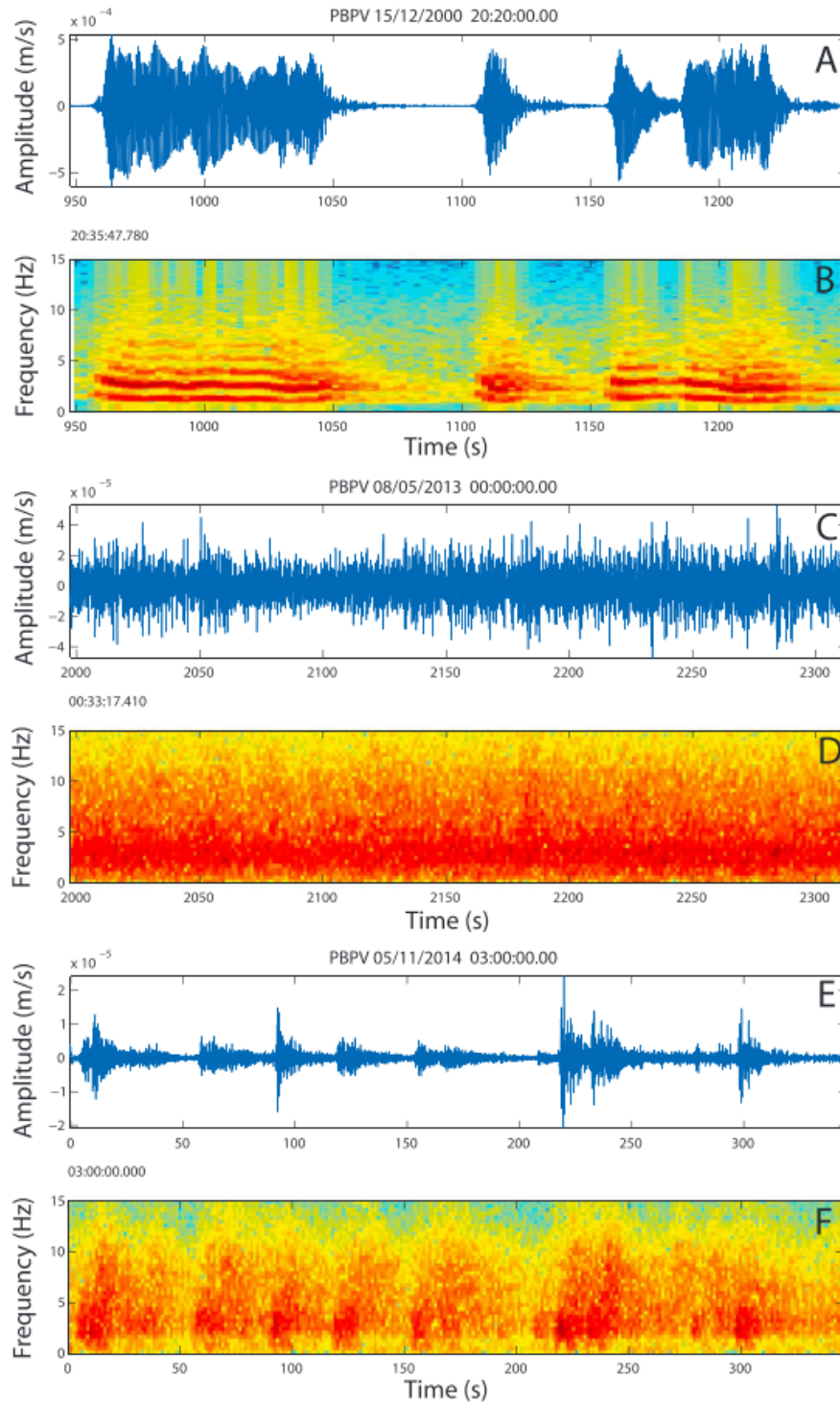


Figure 2.4 – Different kinds of volcanic tremor observed at Popocatepetl (Mexico). (A) Seismogram of an episode of harmonic tremor during 15–16 December 2000 (UTC time), (B) spectrogram of Figure 2a, (C) spasmodic tremor on 8 May 2013, (D) spectrogram of Figure 2c, (E) pulsating tremor on 5 November 2014, and (F) spectrogram of Figure 2e. From Arámbula-Mendoza et al. (2016)

Cruz et al. (1999) showed another observational example of both volcanic tremor kinds at Galeras volcano (Colombia), although they named harmonic one as a ‘flute tremor’, since in that case it was accompanied by a flute-like sound. Besides switching between different types of volcanic tremor may

show a change of its parameters even within the scope of one type. Such complex behavior was observed on Arenal volcano (Costa Rica) by Lesage et al. (2006).

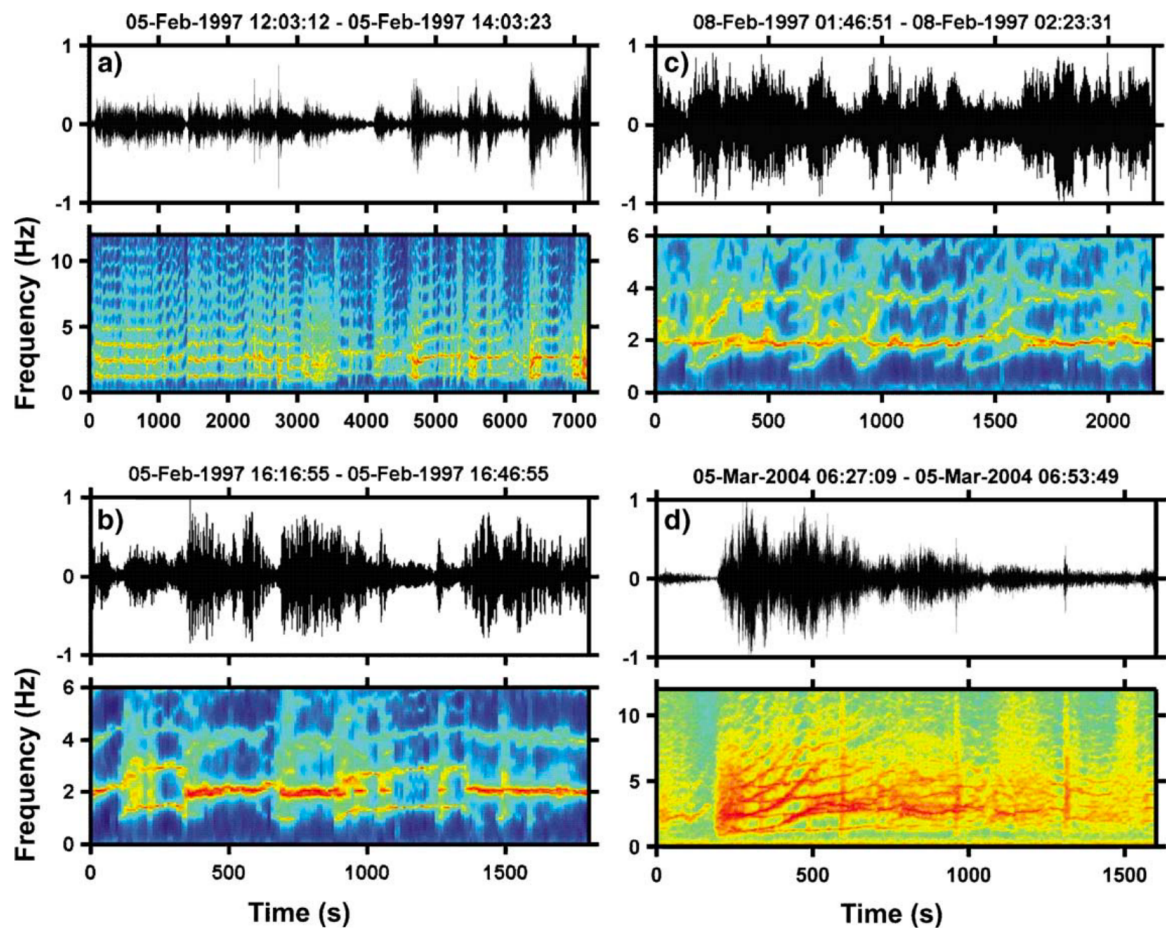


Figure 2.5 – Time-frequency representation and seismogram of volcanic tremor episodes recorded at Arenal volcano, Costa Rica. (a): Two hours of harmonic tremor. (b): Tremor showing sharp transitions between two states characterized by fundamental frequencies of about 1.5 and 2 Hz, respectively. (c, d): Examples of tremor showing two sets of spectral peaks with independent gliding behaviors. From Lesage et al. (2006).

In addition to its time-frequency characteristics, volcanic tremor may be described in relation to volcanic activity. A tremor directly associated with explosive sequences and continuous ash eruptions is often called ‘eruption tremor’, wherever it is harmonic, spasmodic or mixed. McNutt & Nishimura (2008) investigated systematic relations between tremor reduced displacement and factors such as vent radius, erupted volume, and tremor time history with the purpose of deducing general scaling relationships.

The core resemblance in the nature of volcanic tremor and LPs is a wide variety of appearances that indicates possible existence of several distinct physical mechanisms. The frequency content of harmonic tremor and LPs share high similarity that supports an idea of the same source process operating, however, in dissimilar conditions, which may explain such a range of observed signals.

2.2 Physical mechanisms and models

Long-period seismicity in volcanic environments is usually linked to the presence of a fluid phase in the system. LPs and tremor represent volumetric sources driven by pressure disturbances associated with the flow of magmatic and/or hydrothermal fluids. These signals thus provide a direct window into the dynamics of volcanic fluids. The signature of tremor consists of continuous harmonic vibrations, whereas the waveform of a LP event looks like the superposition of simple decaying sinusoids except for a brief time at the event onset (Kumagai & Chouet, 2000).

Virtually all eruptions are accompanied by volcanic tremor, suggesting that the source mechanism behind it is linked to the pressure fluctuation caused by processes of magma movement or degassing (McNutt, 1992). One cannot simply count the number of events for continuous signal like tremor. Synthetic experiments have shown that the duration at different elevated amplitudes is equivalent to counting events because large and small earthquakes have different durations (large ones shake longer). Thus, the source of volcanic tremor may be described by the exponential law. While for earthquakes both the fault area and the slip increase as magnitude increases, for tremor either the source size (such as conduit length) or the magnitude of pressure fluctuations (analogous to slip) must remain constant to produce the observed exponential scaling. The available information indicates that in typical magmatic system the conduit size is a more constant parameter than pressure (McNutt, 1992).

2.2.1 *Resonance triggered by pressure excitation*

Regularly spaced spectral peaks, being one of LP seismicity's main features, are often viewed as the signature of a resonating process within a volcanic structure. Indeed, vibrations on natural frequencies may be sustained by several essential components of a volcano filled with magmatic fluid such as: *magma chamber* and *conduit*, *dikes* and *cracks*. In this perspective, key features of LPs are commonly interpreted as a broadband, time-localized pressure excitation mechanism (trigger mechanism), followed by the response of a fluid-filled resonator (Kumagai & Chouet, 2000).

Spherical magma chamber

Resonance of the magma chamber was one of the first mechanisms suggested for LP earthquakes. Crosson and Bame (1985) analytically modelled it as a spherically symmetrical magma-filled chamber enclosed by solid rocks and containing a spherical gas-filled cavity in the center (*Figure 2.6*). Although highly idealized, this two-boundary model predicts a peaked spectrum and an oscillating, decaying seismogram. For physically arguable values of the model (the 'gas cavity' radius must be more than

few meters), authors were able to obtain seismograms and spectra resembling those of observed LP earthquakes with signal's dominant frequency in the range of 1 to 5 Hz. As the radius decreases, the fundamental mode frequency increases as the inverse power of the radius. The main shortcomings of this model are the inability to explain LPs emergent onsets without special modification of the source time function and the elusive nature of a rather large cavity formation.

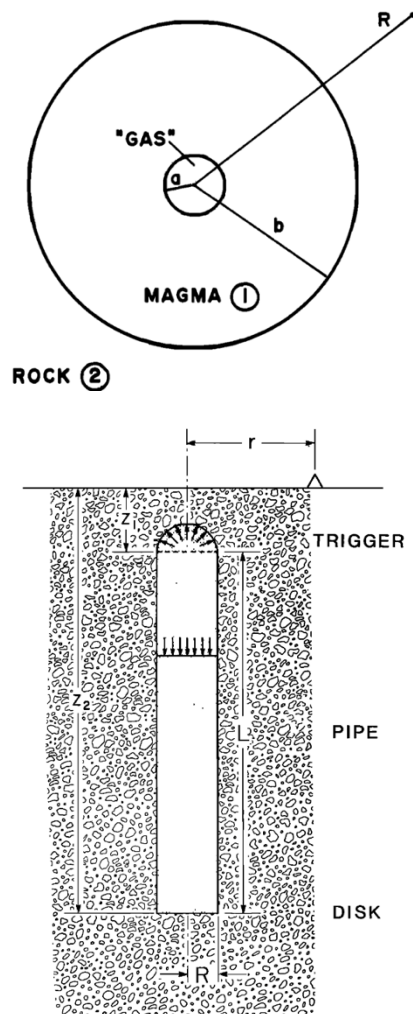


Figure 2.6 - A cylindrical magmatic conduit model proposed by Bernard Chouet to explain harmonic tremor and LPs generation. Configuration of the source, medium, and receiver used in the computation of the ground motion produced by the excitation of a fluid-filled pipe. The composite source consists of a vertical conduit of radius R and length L capped by a hemisphere and shut by a horizontal disk at the bottom. The pipe is filled with a liquid while the hemispherical cap contains a gas. The depth to the pipe inlet is z_1 , and the receiver is located at the epicentral distance r . From Chouet (1985).

Figure 2.7 - Spherical magma chamber model. Diagrammatic sketch of the two-boundary model. The inner cavity is visualized as a gas bubble region within the magma body. Source boundary conditions are applied at the inner cavity boundary. The outer boundary is a fluid-solid interface with continuity of normal stress and displacement. Field observation points are in country rock outside the outer boundary, or inside magma. Subscripts 1 refer to magma properties, and subscripts 2 to properties of the surrounding rock. From (Crasson & Bame, 1985).

Cylindrical magmatic conduit

A magmatic conduit is another exemplary element of the volcano structure, that is commonly depicted in cylindrical symmetry. Bernard Chouet (1985) proposed a seismic model in which the source of tremor is the acoustic resonance of a fluid-filled volcanic pipe triggered by excess gas pressure (Figure 2.7). He used the discrete wave number method to obtain a complete representation of the ground motion response. The trigger contribution, limited to the source proximity, defines strong impulsive onset and resulted characteristics evolve to a well-developed harmonic wave train

dominated by Rayleigh waves at larger distances. This model explains LPs as the elementary process of harmonic tremor generation and interpret it as the resonance system's impulse response

Fluid-filled cracks

A fluid-filled crack is another easily imaginable element of volcano structure with a smaller scale. Fluid-driven crack resonance includes many models with different ideas and geometries (Aki et al., 1977; Chouet, 1986; Kumagai & Chouet, 2000). Overall, it may be considered the most common kind of physical models proposed in literature to explain existence of both LPs and harmonic tremor (Chouet, 1988). This model accurately reproduce observed signals for LP earthquake, while tremor in this case

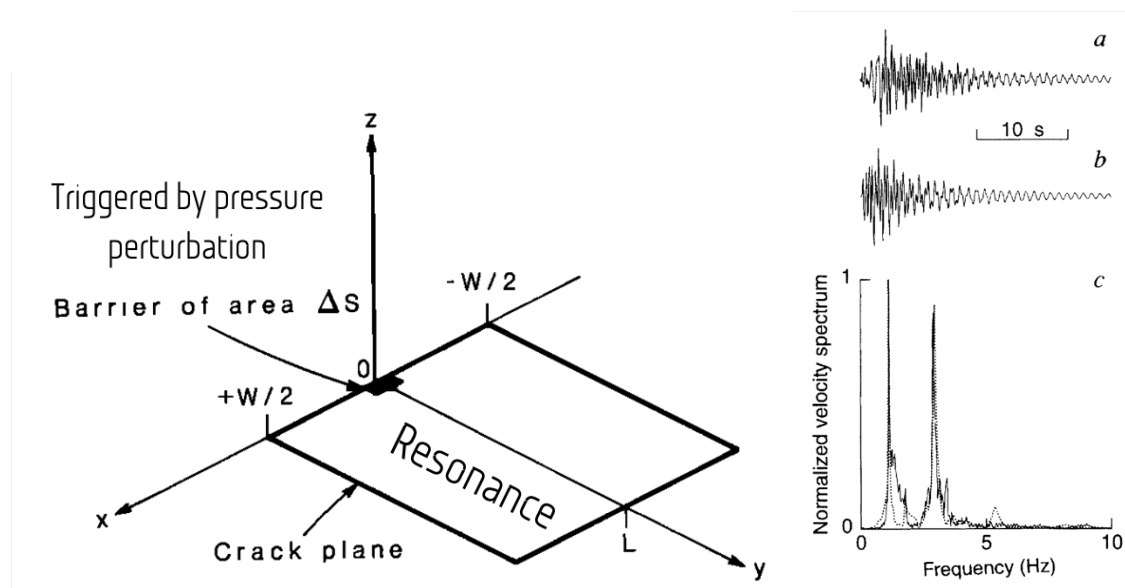


Figure 2.8 – Fluid-filled crack model (left) and comparison of the real LP signal and synthetic seismogram (right) calculated for this model: (a) LP event preceding January 14th 1993 eruption of Galeras volcano; (b) Synthetic signal calculated for crack dimensions of 180 m x 90m x 0.05 m, crack stiffness 100, sound speed of fluid 0.3 km s⁻¹, compressional wave speed of solid 2.5 km s⁻¹, density ratio of fluid to rock 0.5, and ratio of bulk modulus of fluid to rigidity of rock 0.025; (c) Spectrum of real data and synthetics (dotted). Modified after (Chouet, 1986, 1996).

In summary, resonance-based physical models of LP seismicity may be considered 'go-to' explanation, but they ultimately require some sort of pressure pulse perturbation to act as a trigger. The nature of such pressure perturbation being assumed as a trigger mechanism for the resonance is somewhat debatable. On one hand it directly controls the rate of LP earthquakes and whether they could merge in continuous tremor. Therefore, a volcanologist can link LP activity to magmatic system behavior. On the other hand, unclear conditions of such a trigger leave a place for the model extension if one is able to answer *why* the trigger pulse occurs in the first place?

2.2.2 Flow-induced oscillations

Among other models of LP seismicity there are a class of those based on processes that may invoke unstable fluid flow itself rather than a resonance of some volcanic structure. As shown by Bruce R. Julian (1994) a nonlinear process analogous to the excitation mechanism of musical wind instruments and human vocal cords can explain many characteristics of volcanic tremor, including (1) periodic and "chaotic" oscillations, with peaked and irregular spectra respectively, (2) rapid pulsations in eruptions occurring at the same frequency as tremor, (3) systematic changes in tremor amplitude as channel geometry evolves during an eruption, (4) the period doubling reported for Hawaiian deep tremor, and (5) the fact that the onset of tremor can be either gradual or abrupt.

While this mechanism is more suited for tremor, it may as well explain LP earthquakes as oscillations excited by transient disturbances produced by nearby earthquakes, fluid heterogeneity, or changes in channel geometry, when the magma flow rate is too low to excite continuous tremor. Julian proposed a simple lumped-parameter tremor model involving the flow of an incompressible viscous fluid through a channel with movable elastic walls leads to a third-order system of nonlinear ordinary differential equations (Figure 2.9). As shown in this article for different driving fluid pressures, numerical solutions exhibit steady flow, simple limit-cycle oscillations, a cascade of period-doubling subharmonic bifurcations, and chaotic oscillations. In this model, tremor occurs most easily at local constrictions, and fluid discharge is lower than would occur in unstable steady flow.

Tremor observed at Sakurajima volcano (transverse component)

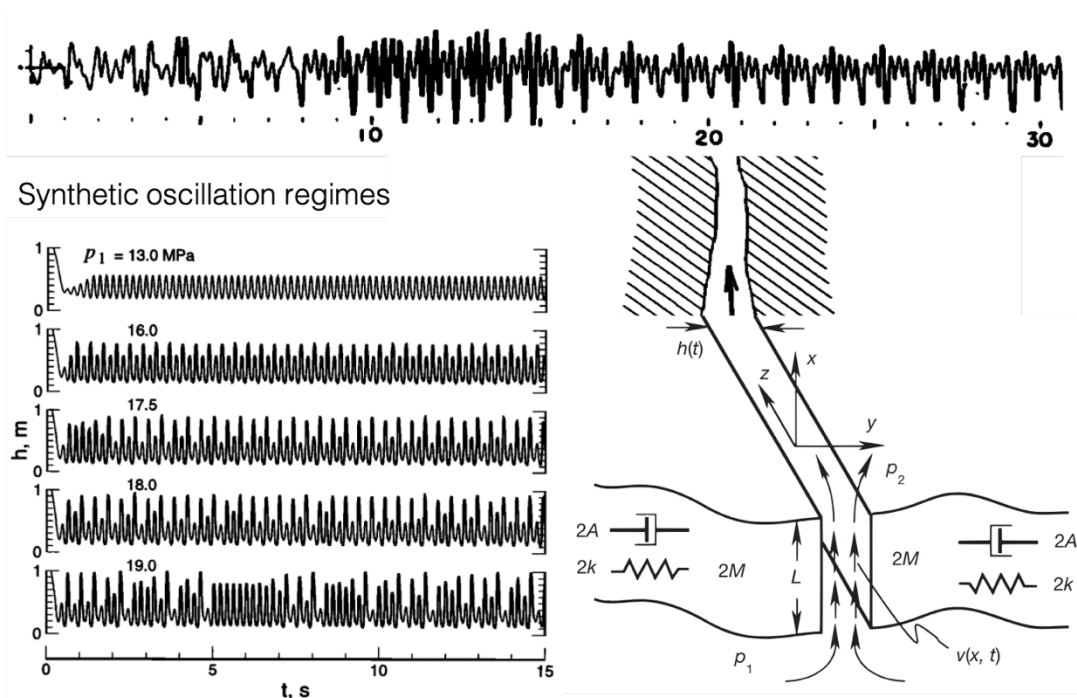


Figure 2.9 - Model of nonlinear excitation by viscous, incompressible fluid flow (magma) moving upwards through a channel with imperfectly elastic walls. Modified from (Julian, 1994)

2.2.3 Bubble dynamics

Last class of physical models that the author was able to acquire from existing literature deals with three-phase magmatic systems that involves gas bubble dynamics. Such models are serious contender for volcanic seismicity in general, because volatiles play a significant role in volcanic eruptions, especially the explosive ones and magma degassing is observed at many volcanoes.

For example, in the article by Ripepe & Gordeev (1999), infrasonic and seismic signals of shallow volcanic tremor at Stromboli were explained by a two-step model of gas bubble coalescence and bursting. Authors calculated that forced coalescence induced in magma a pressure change ($\sim 10^4$ Pa) sufficient to explain tremor ground displacement (10^{-5} m).

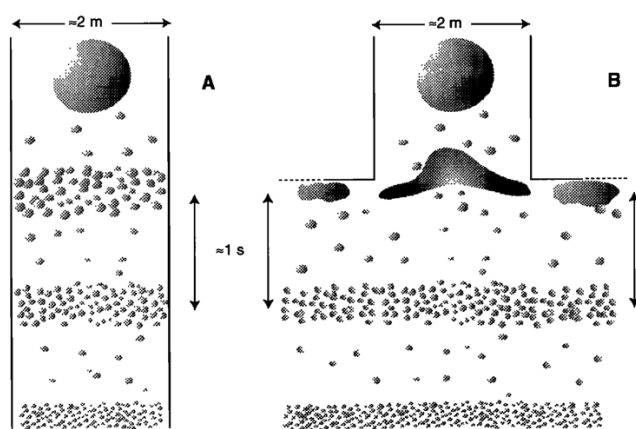


Figure 2.10 – Schematic illustration of gas bubble coalescence models: (a) Free coalescence model: bubble layers rising along the conduit freely coalesce in a larger bubble when hydrostatic pressure drops below a critical value. (b) Forced coalescence model: a layer of bubbles reaching a structural barrier is forced to coalesce and starts flowing in the above conduit inducing a hydrostatic pressure drop.

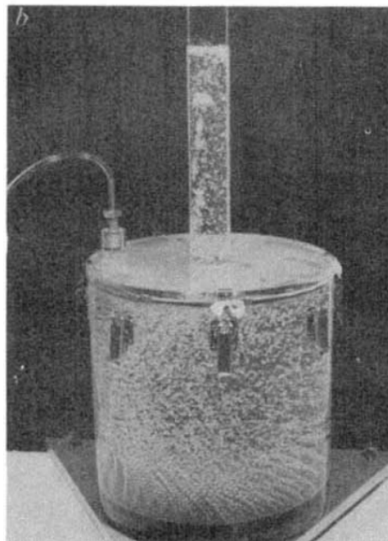


Figure 2.11 – Laboratory magma degassing experiment (with 0.1 Pa s liquid viscosity) described in (Jaupart & Vergnolle, 1988).

The great thing about bubble dynamics is that it has some laboratory modeling to support the ideas behind it. Jaupart & Vergnolle (1988) simulated degassing process in basaltic eruptions as a tank filled with viscous fluid and topped by a small open conduit. The bubbles rise and accumulate at the roof in a foam layer whose thickness increases. At a critical point the bubble coalesces and the foam collapses, generating gas pockets whose size depends on liquid viscosity and surface tension. At low viscosity a single gas pocket is formed which flow into the conduit, while at higher many smaller pockets are formed, which rise as slugs and burst out intermittently at the vent. The experiments imply that the presence of constrictions in the chamber and conduits plays a major role in determining eruption behavior.

Chapter 3:

Seismic Experiment on Gorely

Moving further from the general discussion on the topic of volcano seismology (Chapter 1) and description of the specific volcanic seismicity type (Chapter 2), this chapter logically closes the first part by presenting the study object and acquired seismic data. Two key questions have to be answered in order to fully comprehend the significance of the results discussed in the second part of the thesis. **Why** is Gorely volcano so impressive from the volcanological point of view, although it is not the most dangerous or magnificent volcano in Kamchatka? Furthermore, **what** makes recorded data so unique, even though a particular temporary seismic experiment was carried out back in 2013–2014? The chapter is divided into two sections accordingly to answer these questions:

- Section 3.1 describes the Gorely volcanic system geological evolution in the Kamchatka tectonic context and previously conducted studies.
- Section 3.2 showcases seismic experiment of 2013–2014: its design, the installation process and pre-processing of the temporary network data.

In a linear manuscript structure, this particular chapter marks a transition from research background to the thesis foreground as the very seismic experiment on Gorely reported here has conceived the PhD project initial idea.

3.1: Gorely volcano

In the eyes of the general public, a volcano is classically depicted as a perfect cone with steep slopes. Although it is correct for some iconic stratovolcanoes like Mount Fuji, Gorely volcano cannot be represented by such an ideal shape. This long-lived eruptive center does not stand out in the landscape, yet it has an intriguing geological history which has been preserved in its composite structure. The main morphological feature – a large ancient caldera can be viewed as a proof of the system's ability to produce powerful eruptions, which already happened once and probably may be repeated in future. Moreover, during active degassing phase Gorely emits significant volume of H_2O , CO_2 and SO_2 , which signifies substantial volatile content in the source magma.

3.1.1: Geography and tectonic context of Kamchatka

Gorely volcano is located in one of the most outstanding volcanic regions of the world – the Kamchatka Peninsula. Spectacular coastline, high density of active and extinct volcanoes, glaciers with alpine lakes and wild rivers: all this together forms a dynamic landscape of incredible beauty. It is not surprising that Volcanoes of Kamchatka were included in the World Heritage List by UNESCO and Kamchatka itself is often referred in media as “The Land of Ice and Fire”. More importantly, from a scientific point of view, Kamchatka can be considered a natural laboratory for studying volcanism of subduction zones owing to the amount and diversity of volcanic systems varying in age, volume, eruption style, and magma composition.

Geographically the Kamchatka Peninsula occupies the north-eastern part of Eurasia and stretches from the north-east to the south-west for about 1 200 km. The Pacific Ocean and the Sea of Okhotsk make up the peninsula's eastern and western coastlines, respectively. With a total area of approximately 270 000 km², it is connected to the mainland in the north by narrow (93 km) isthmus and the maximum width of peninsula reaches 440 kilometers at the latitude of Cape Kronotsky. The southernmost point of Kamchatka - Cape Lopatka lies about 11 km north of Shumshu, the northernmost island of the Kuril archipelago. The Pacific coast of Kamchatka has many bays and immediately offshore along it runs the 10.5 km deep Kuril–Kamchatka Trench.

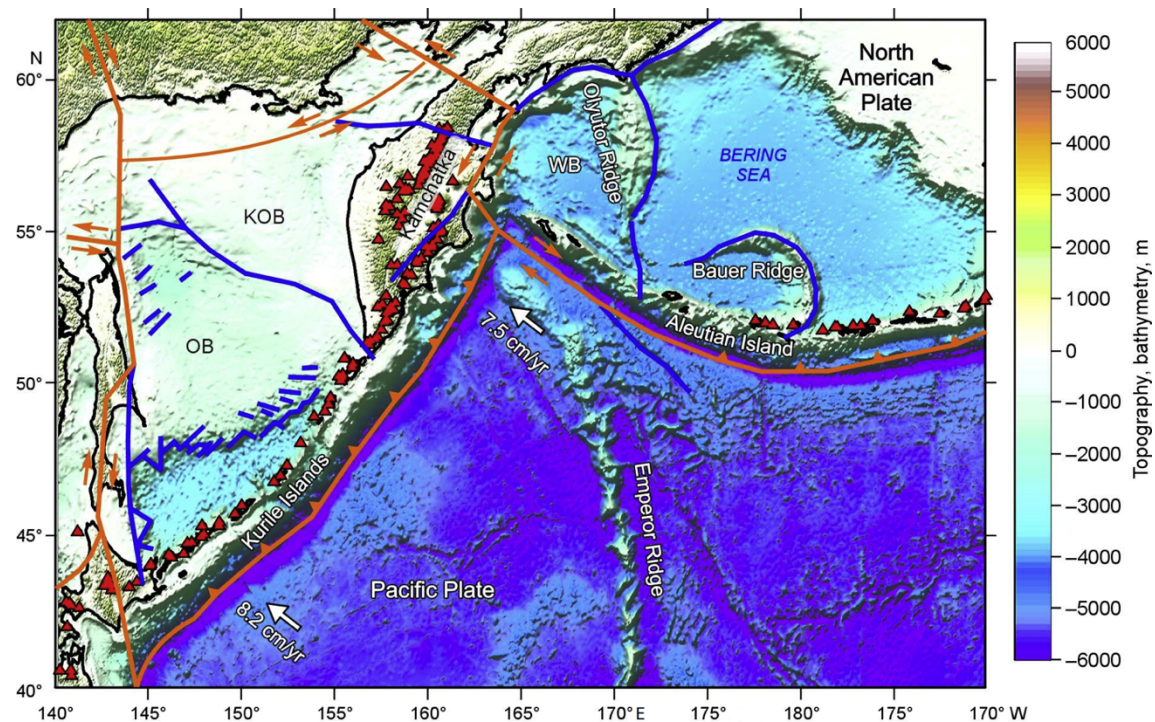


Figure 3.1 – Main geographical and tectonic units in the study region, with a topographic/bathymetric base map (after Koulakov et al., 2011). Orange lines represent main tectonic-plate boundaries; violet ones were suggested by the article authors. The movement speed of the Pacific Plate is (after Avdeiko et al., 2007 and Steblou et al. 2010). Red triangles show active volcanoes (after Simkin and Siebert, 1994). WB, Western Basin; KOB, Kamchatka–Okhotsk block; OB, Okhotsk block.

The Kuril-Kamchatka Trench indicates an active convergent margin of the Pacific Plate. The Japan Trench continues it on the south, while its northern part abuts at almost 90° angle to the Aleutian Trench which spreads to the east. This entire area is a result of the Pacific Plate subduction under the adjacent plates caused by its overall movement in the north-west direction (*Figure 3.1*). Corresponding volcanic arcs constitute a substantial part of the famous Ring of Fire, also remarkable for the abundance of seismic activity. The Kamchatka peninsula, in particular, represents a zone of very intense volcanism due to the high subduction rate and structural features of the converged plates.

Quaternary arc volcanism on the peninsula is presented in three distinguished regions: the oldest and nearly extinct Sredinny Ridge, Central Kamchatka Depression containing very active Northern Group of Volcanoes, and young Eastern Volcanic Front (**EVF**) (Avdeiko et al., 2007). Both Northern Group and EVF are fed by processes associated with the contemporary subduction of the Pacific plate beneath the northern part (Kamchatka-Okhotsk block) of the Okhotsk microplate (Apel et al., 2006; Kogan et al., 2000). Under the ~700-km long EVF general azimuth and dip of subduction in relation to the overriding plate appears to be ~310° and ~55° respectively (Gorbatov et al., 1997). The rate of subduction is estimated at ~80 mm/year and the age of the subducting plate is estimated at ~80-90 Ma (Timofeev et al., 2012). Located in the southern segment of EVF, Gorely stands about 130 km above the slab surface (Gavrilenko et al., 2016).

While magmatism on Kamchatka dates back to the Cretaceous, current plate-tectonic geometry has formed from Late Miocene to Early Pliocene with the following remarkable increase in volcanic activity during Upper Pleistocene and Holocene period (Melekescev et al., 1987). The formation of the Kamchatka volcanic arc is associated with the rotation of the Pacific Plate 45 and 30 million years ago, which led to the restructuring of the back-arc basins and subduction zones in the interval 15-20 million years ago (Avdeiko et al., 2007). It started with a collision of the Ozernovsko-Valaginsky island arc with Kamchatka, which dates back about 55 million years ago (Volynets et al., 1992). Starting from 15 million years to 7 million years ago, the structure of the eastern part of Kamchatka changed significantly: many bays were formed, which is connected to the process of collision with the Kronotsky arc (Portnyagin et al., 2005). In its modern form, the Kamchatka volcanic arc has formed at the end of Miocene – early Pliocene (Avdeiko et al., 2001).

In the geological discussion, Gorely is usually mentioned with nearly located Mutnovsky volcano, which lies 15 km to the southeast. Together they form a short row in the direction of slab sinking orthogonal to the general stretch of volcanic ridges on Kamchatka. Thus, a shared magmatic feeding system may exist in the mantle wedge and lower crust below these two volcanoes. However, in the upper crust, Gorely and Mutnovsky volcanoes appear to be currently divided by a narrow amagmatic zone. Moreover, the independence of their magma sources is supported by compositional

features of erupted material. Despite close tectonic positions and apparent similarity of the eruption style, neighboring Mutnovsky and Gorely volcanoes are significantly different in their evolution.

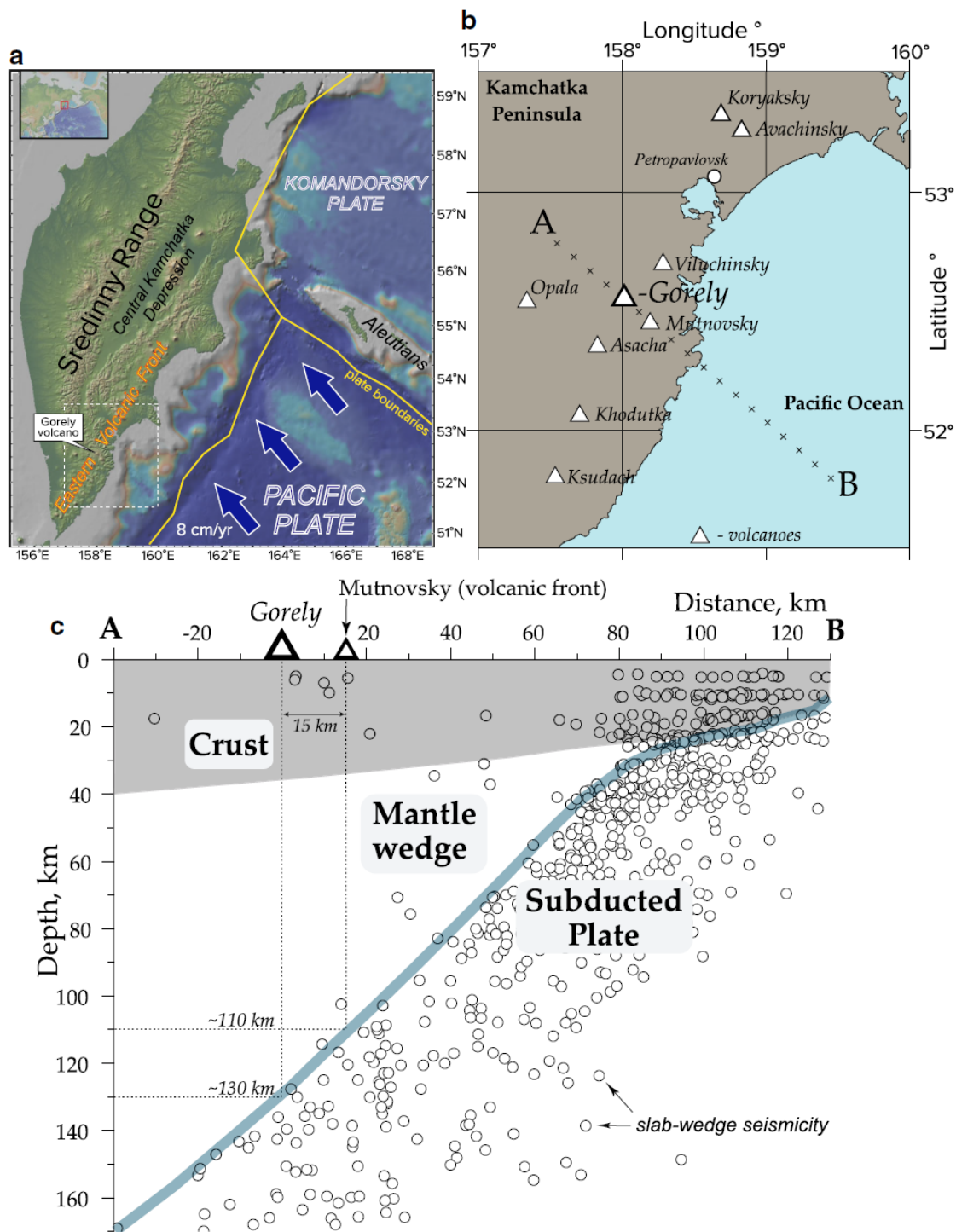


Figure 3.2 – Gorely volcano in the tectonic context of Kamchatka, as presented in the comprehensive paper by Gavrilenko et al., 2016: (a) Kamchatka structural units and Gorely volcano location. The topographic base was produced in GeoMapApp (<http://www.geomapp.org>), based on the Global Multi-Resolution Topography (GMRT) synthesis (Ryan et al. 2009). Arrows show the direction of Pacific plate subduction—310°. **(b)** Location of seismic profile (A-B) with names of surrounding volcanoes. **(c)** Seismic profile through Kamchatka subduction zone centered on Gorely volcano, showing seismic events with $M_w > 5.5$, as calculated and reported by the Kamchatka Branch of the Geophysical Service (KBGS), drafted within a 20-km band perpendicular to the strike of the subducting Pacific slab (310°).

3.1.2 Morphology and evolution of the Gorely volcanic system

Morphologically Gorely is a compound stratovolcano: the modern edifice is nested inside a broad caldera of its ancient similitude. Based on the age and composition of the erupted rocks, one can define three significant stages of its formation, which are described below.

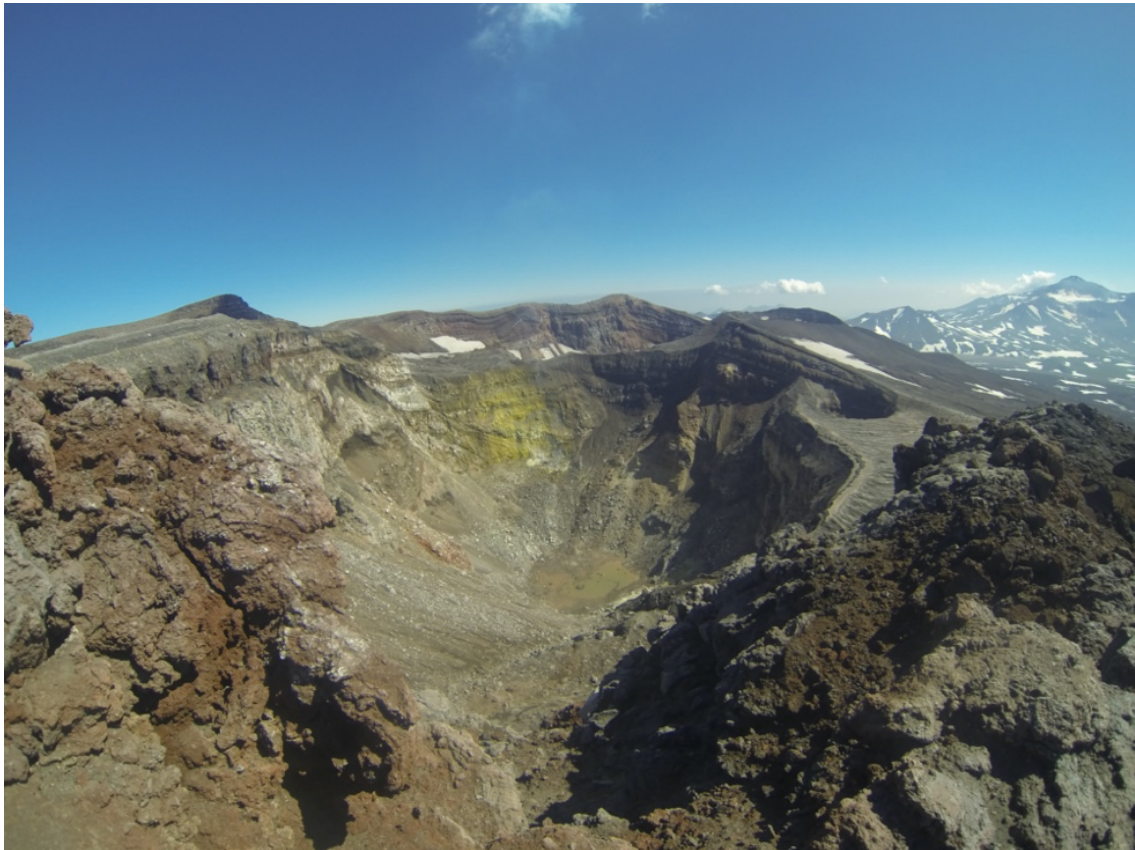


Figure 3.3 – Photography of the Gorely’s currently active crater made by the author during the expedition in August 2013.

First (pre-caldera) stage is linked to the development of Pra-Gorely (also referred to as “Old Gorely”). It was an extensive shield volcano of about 12 x 15 km in size stretched in the north-eastern direction. Pra-Gorely has emerged in the middle Pleistocene through multiple centers of extrusive magmatic discharge. The erupted material composition in this period ranged from basalts and andesites to dacitic extrusions and rhyolites. Nowadays the remnants of Pra-Gorely are mainly represented by peripheral parts of massive lava flows at the edges of the caldera and some relicts in the surrounding plateau. In particular, the sole episode of magma breakthrough in the zone between Mutnovsky and Gorely belongs to this stage. Two echelon-like displaced chains of slag cones are opened from under cover of later volcanic deposits at the south-eastern side of the caldera and at the foot of the Dvugorbaya mount.

Second stage led to formation of both large caldera in the top part of Gorely's older edifice and massive felsic pyroclastic deposits surrounding it with the estimated area of 600 km². This thick ignimbrite and pumice complex with the total volume >100 km³ was once believed to have been deposited during a single caldera-forming eruption approximately 38–40 ka (Selyangin & Ponomareva, 1999). However, Ar-Ar and U-Pb dating from different ignimbrite units suggest that there were several nested calderas ranging in age from 361 ka to 38 ka (Bindeman et al., 2010). Whether it was single catastrophic eruption event or series of consecutive eruptions, the result is morphologically equal: depletion of a large magma chamber embedded in the earth's crust below Pra-Gorely caused its roof to collapse. This has formed the actual caldera (or as one may see it – a series of nested calderas) in the top part of the ancient edifice which has an oval shape elongated to the northwest direction and measuring 10 x 13 km in size. Its top layer was filled with products of eruption (mostly ignimbrites), while bottom part represents so-called “broken dish” structure: disposed pieces of the Pra-Gorely edifice that fell few hundred meters down.

Last (post-caldera) stage has started toward the end of Late Pleistocene with monogenetic volcanism on the weakened zone of caldera rim. It was continued by formation and development of the modern structure in the central part. There are three main merged cones stretched in west-northwest direction chronologically named as G1, G2 and G3, but in terms of magmatic evolution one may define 6 cycles during this stage. In the first one (Q₃⁴) a large structure of Gorely-1 (G1) was formed as a result of extensive andesite-basaltic lava discharge. Second cycle (Q₄¹) is characterized by development of the Gorely-2 (G2) cone (primarily made of andesite-basalts) and appearance of many secondary magma ruptures on the slopes of new volcanic edifice. In this period a fracture (rift) zone started to develop below modern construction, which later became the main magma-conducting framework. The third cycle (Q₄²) of volcanic activity is associated with the formation of the youngest and smallest volume cone Gorely-3 (G3) on the south-western slope of G2. It is complicated by a number of side breakthroughs, from which outflows of lavas of predominantly andesite-basaltic composition occurred. Almost simultaneously on the north-western and southwestern slopes of G2 in insignificant volumes poured medium-composition lavas of the fourth cycle (Q₄²). The last two largest episodes of volcanic activity of the fifth (Q₄³) and sixth (Q₄⁴) cycles are associated with the lava eruptions of primary and secondary composition along a branched riftogenetic zone that intersects the modern structure and also forms a short north-western branch on the slope of the G1 complex.

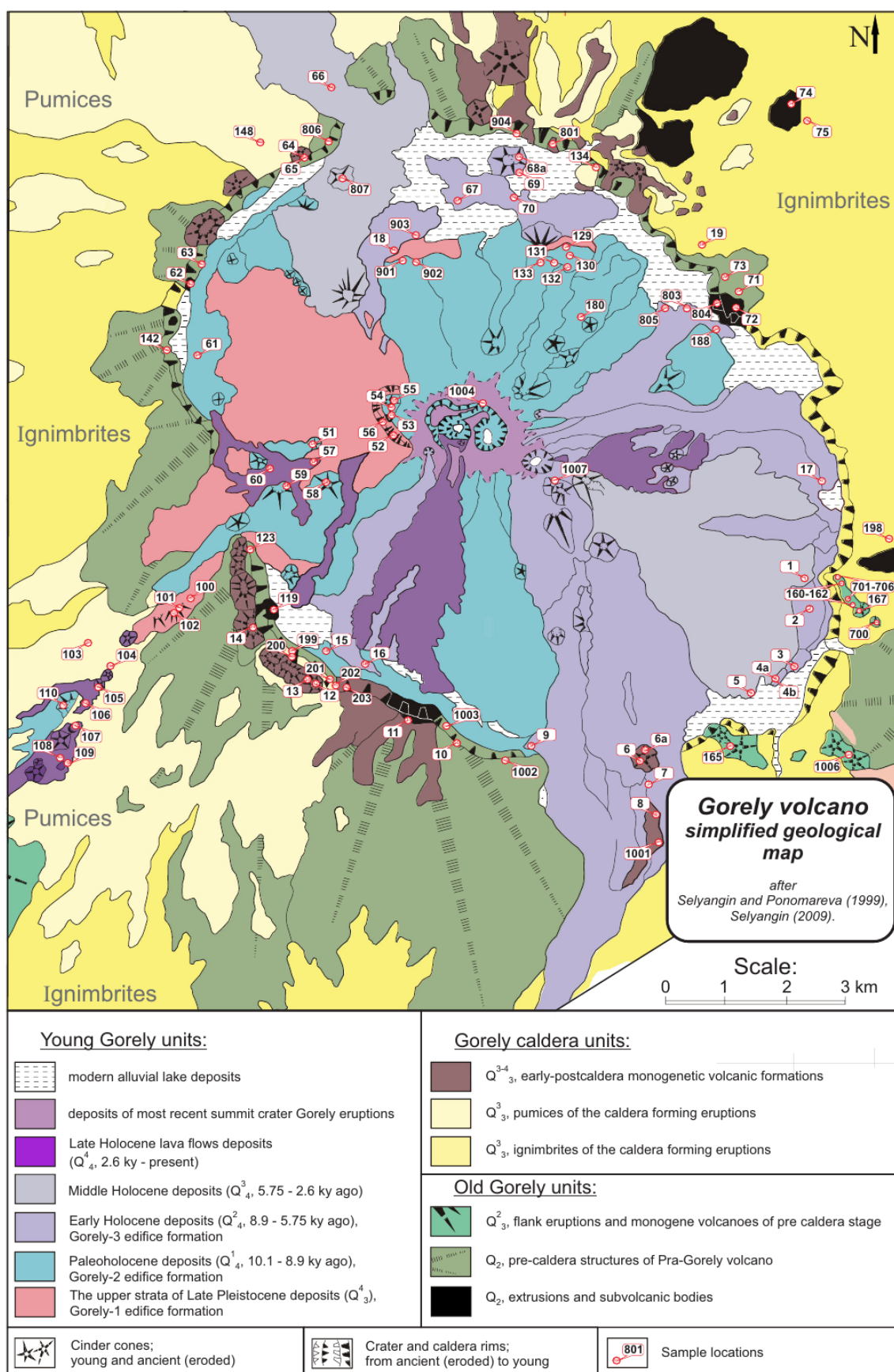


Figure 3.4 – Simplified geological map of Gorely. From Gavrilenko et al., 2016, after Selyangin & Ponomareva, 1999.

Thus, contemporary Gorely represents steady evolutionary development of the old volcanic center, followed by a radical transformation of its magma-feeding system (Gavrilenko et al., 2016). The recent activity consists of cyclic alternation between phases of persistent degassing and Vulcanian-style explosive eruptions, with periods of voluminous (about 0.1 km³) lava flow eruptions from the volcano's rift systems. After the most recent magmatic eruption in 1986, a large fumarole was formed in the crater of the Gorely volcano, through which an active emission of gases is occurred. In the period of strongest degassing activity in 2010, the mass of gases emitted through this fumarole was estimated at 11,000 tons per day with the outlet temperature reaching 900 °C. It was determined that these gases were composed of water (93.5%), CO₂ (2.6%), SO₂ (2.2%), HCl (1.1%), HF (0.3%), H₂ (0.2%), as well as some bromine and iodine compounds. It is estimated that in such conditions, Gorely emits about 0.3% and 1.6% of the total global fluxes from arc volcanism for CO₂ and HCl, respectively (Aiuppa et al., 2012).

3.1.3 Previous studies

Being quite a remote part of the Russian Far East, the Kamchatka peninsula is lacking an extensive historical record as one may found for more populated volcanic areas of the world. For several centuries Kamchatka has been synonymous with distant unknown territory, its actual coastline was discovered only in XVIII century during two monumental expeditions led by Vitus Bering. The earliest information about the natural features of this land, including volcanological and seismological ones were noted by academician Krasheninnikov (during the second Kamchatka expedition in 1737 - 1741) in his unique book "The description of the land of Kamchatka" (Krasheninnikov, 1755; and translation). Scientific exploration of the peninsula was continued by Karl Ditmar in 1851 - 1854, and another major expedition of Russian Geographical Society in 1908 - 1910 (Ditmar, 1901; Zayceva, Kotlyakov). Finally, regular volcanological studies of Kamchatka began in '30s of XX century (Novograblenov 1932, Kulakov 1936, Zavaritsky et al. 1954, Svyatlovsky 1956, Vlodavets 1957).

The first robust data on the geological structure and development of Gorely volcano was published by Kirsanov (1964; 1985), who described the volcano caldera and associated pumice-ignimbrite deposits, material composition of the pre-caldera structure and the modern volcanic edifice. Since 1959, observations of the volcanic activity on Gorely became systematic and all its later eruptions have been described in detail (Kirsanov and Fedorov 1964; Kirsanov et al. 1964; Kirsanov and Ozerov 1983; Kirsanov and Melekescev 1991). In 1974-1977 a geological survey on a scale of 1:50,000 was performed in the area and, as a result of this work, information about basement structure was obtained. It was followed by detailed geological map of Gorely volcano (Selyangin & Ponomareva, 1999) and the comprehensive reconstruction of its Holocene activity via tephrochronological analysis

(Melekescev et al., 1987). Recent geochemical and petrological studies focused on mantle wedge melting (Duggen et al., 2007), magma chamber processes (Chashchin and Martynov 2011; Chashchin et al. 2011), melt inclusions (Tolstykh et al., 2012), and silicic magma generation (Seligman et al., 2014).

Some studies of the volcano were associated with the exploring of the Mutnovsky-Gorely territory for ore raw materials and geothermal resources. These studies have indicated that Mutnovsky and Gorely volcanoes together represent paired magmatic systems with numerous geothermal sources. One of these sources is exploited by the Mutnovsky Geothermal Power Plant (MGPP) with the capacity of 50 MWt, which provides a significant part of the electrical energy to the metropole city of Petropavlovsk-Kamchatsky and its surroundings. In total it uses 12 boreholes that provide a mixture of overheated steam and water. Based on the amount of the explored geothermal sources, the capacity of the MGPP can be increased up to 300 MWt.

In 1980 radio-telemetric seismic station GRL was installed on the eastern slope of Gorely volcano by the Kamchatka branch of the Geophysical Survey of the Russian Academy of Sciences. In the summer of 2008, two more stations were installed in the area of neighboring volcanoes: MTV (on Mutnovsky volcano) and ASA (on Asacha volcano). All stations are equipped with three-component sets of short-period channels based on SM-3 seismometers for recording the speed of ground displacement in the frequency band 0.8–20 Hz (Chebrov et al., 2013). These permanent stations were used to investigate the seismicity beneath Gorely since 1984 (Sobolevskaya, 2009). Note however that these studies could only provide count and energy estimates for the events, but not the information about their locations. In addition to seismological approaches, other geological and geophysical methods were used to study the structure of the volcanic system of Gorely volcano, in particular, based on the use of electromagnetic fields. A large scale geoelectric model for Kamchatka was obtained using a magneto telluric sounding (Moroz & Pospeev, 1995). The authors revealed a conductive layer at a depth of 50 km with the resistance of 50 Ohm*m, which probably indicates the presence of a liquid phase in it (hydrothermal solutions and/or melts). Similar results are found on a smaller scale in geoelectric section along the profile from Gorely to Mutnovsky (Bortnikova S.B., 2013).

The installation of a temporary seismic network in 2013-2014 made possible obtaining a spatial distribution of seismicity and building a three-dimensional seismic model beneath Gorely volcano for the first time (Kuznetsov et al., 2017). The local earthquake seismic tomography inversion in this study was based on the LOTOS code (Koulakov, 2009). A careful manual selection of VT earthquakes suitable for travel time tomography in the presence of numerous LPs is a challenging task. Before the actual tomography inversion, authors made a grid-search for finding an optimal reference model that identified an unusually low average V_p/V_s of about 1.5. They interpreted this low value of the ratio as an indicator of a very high gas content in porous rocks composing the volcano Gorely. Similar gas

contaminated rocks with very low V_p/V_s were observed, for example, in Campi Flegrei (Battaglia et al., 2006; De Siena et al., 2010), where strong degassing and fumarole activity is also present. Such relationships between gas content and seismic attributes were also derived in a number of laboratory experiments (ex. Takei, 2002).

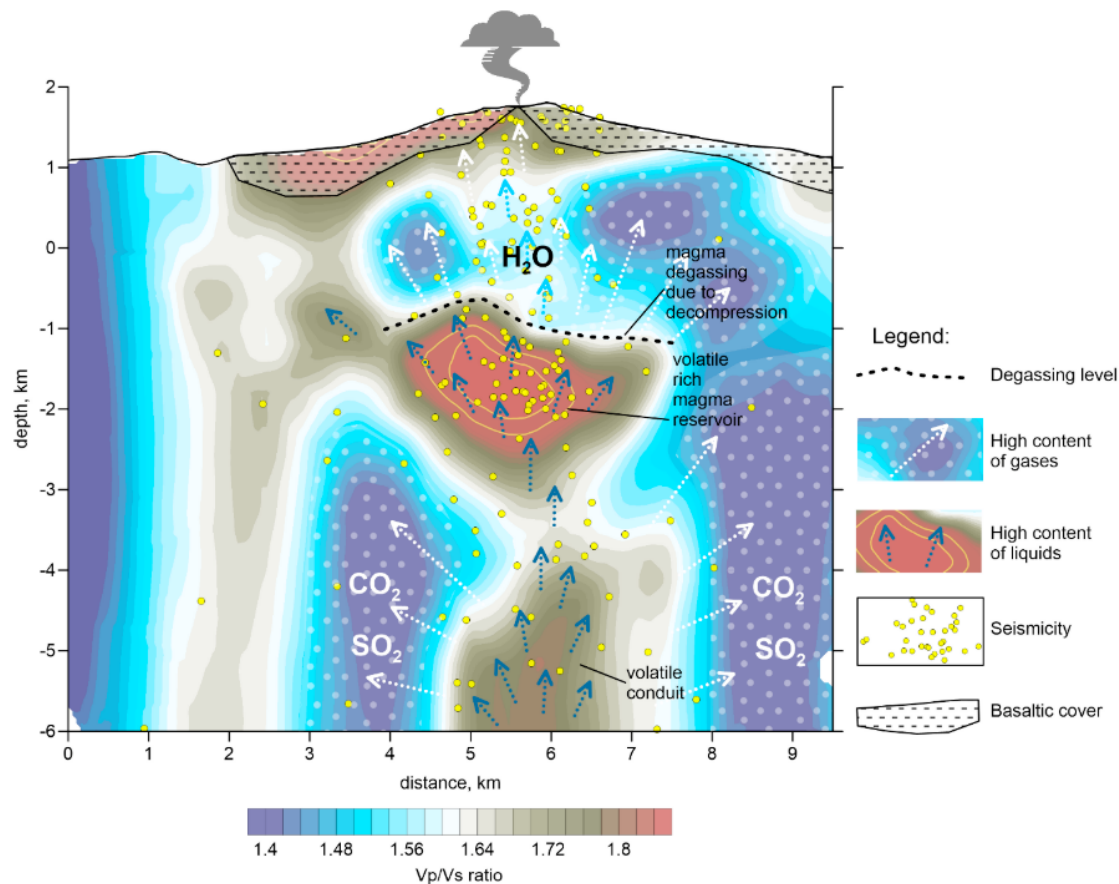


Figure 3.5 – Interpretation of the Gorely's tomography model (proposed in Kuznetsov et al., 2017): the distribution of V_p/V_s in vertical section is shown as background color. Yellow dots represent the seismic events. Two yellow contours within reddish area indicate the anomaly with V_p/V_s values of 1.9 and 2 respectively, discussed in text.

Based on these observations, Kuznetsov et al. (2017) conclude that in 2013–2014, Gorely represented a system highly saturated with gases and called by them “steam boiler” (Figure 3.5). The model reveals an anomaly of high V_p/V_s ratio located right beneath the shallow magma reservoir at depths starting from 3 km below surface level, which is interpreted as a conduit delivering the volatiles to the shallow reservoir from deeper sources. Authors also proposed that the near surface layer with high velocities represent a basaltic cover that prevents gases to release. The only location where gases escaped is the central fumarole, where the gas flux may reach the amount of 11,000 tons per day (as was previously measured by Aiuppa et al., 2012).

3.2 Temporary seismic network of 2013-2014

Besides a single permanent station GRL located on the volcanic edifice and used as a reference, a dense temporal seismic network of 21 three-component broadband seismographs was operated on Gorely for almost a year autonomously (Figure 3.6). It was installed on the volcanic edifice and in the surrounding area in August 2013 and removed in August 2014 after collecting ~350 Gb of continuous seismic records in total. Overall data coverage in space remains consistent enough for more than eight months with maximal density during the first four months. Some stations of the temporal network were eventually flooded by groundwaters or destroyed by wildlife (for example C4 station dug out by a bear). Most importantly, this data covering a significant span, including the period of activity, visually observed degassing during the network installation.

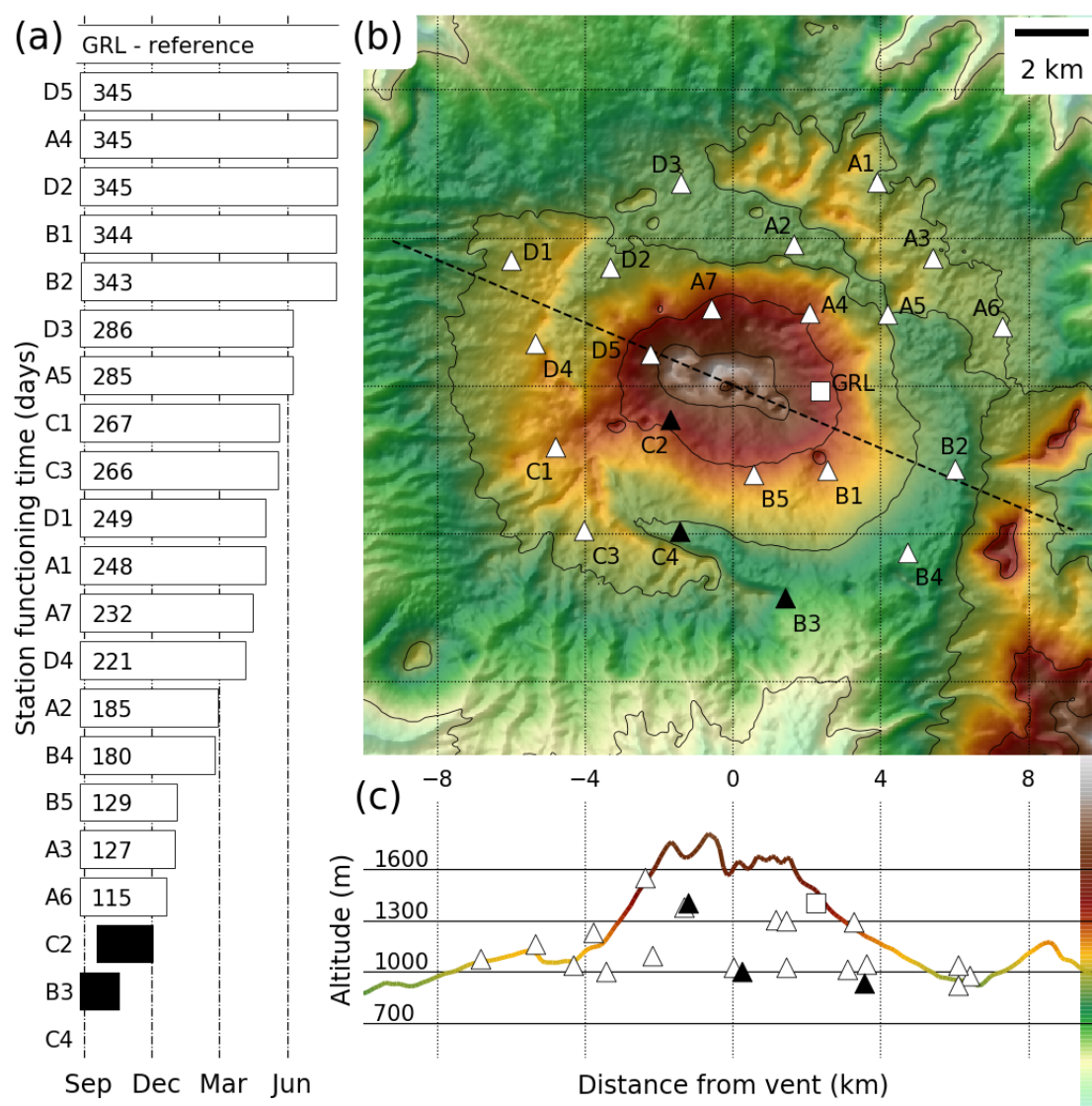


Figure 3.6 – The temporary seismic network on Gorely (August 2013–August 2014): (a) data recovery chart sorted according to station functioning time; (b) network geometry along with volcano topography (white triangles – stations used for analysis, white square – referential permanent GRL station, black triangles – non-functional stations); (c) projection of station locations on the volcanic edifice along the dashed line.

3.2.1 Equipment and installation process

Each of the temporal stations consisted of a three-component broadband sensor CME-4311 and a digital recorded Baikal-ACN-87/88 with power supply provided by one box of 10 high-capacity power batteries Baken VTs-1, external GPS antenna and essential ventilated protection against dust and moisture (*Figure 3.7*). Baikal-ACN series recorders are 3-channel autonomous seismic stations of an extended frequency range with an internal or external GPS module, a USB 2.0 channel for communication with a laptop and a memory slot for SD card supporting volumes up to 32GB. Recorded has internal backup power (two type-C batteries), however, for prolonged operations, it requires an external DC source with a rated voltage of 12 V. Powered in recording mode the current consumption does not exceed 50 mA. The maximum duration of continuous operation is limited only by the battery capacity and memory card used as declared by the manufacturer (“Baikal-CAN” recorder, Technical Passport).



Figure 3.7 – Equipment of a temporary seismic station and the installation process. Photos are courtesy of field experiment team members: Nikolai M. Shapiro, Ilyas Abkadyrov and Andrey Jakovlev.

The three-component broadband velocimeter CME-4311 is designed of three orthogonally oriented molecular-electronic transducer and an electronic board mounted on common base and placed in a protective outer casing. During external mechanical action due to the seismic vibrations

of the ground, a working fluid (concentrated electrolyte solution) inside the transducers moves between the electrodes removing or bringing to them ions of the dissolved substance. The convective flow of charged ions causes an electrical response at the electrodes, which is amplified and converted into electrical signal as voltage at the output for each channel, proportional to the speed of the ground movement. The manufacturer stated flat instrument response in the frequency band of 0.016 (60 sec) to 50 Hz (“CME-4311” sensor, Technical Passport).

Although each installation site has posed unique challenges, we used to follow identical process for every temporal station. First, two close holes of about 0.5 m² (circle) and 1 m² (rectangular) were dug in the ground to a depth of one meter. After that, the sensor was placed in the smaller circle pit on an artificial stone pedestal (a flat cinder block), securely fixed in bedrock. The sensor was set in azimuth and level so that the components N and E coincided with the directions to the north and east, respectively, and Z was strictly vertical. Next, both sensor and recorder together with the connected cables were covered with an oakum (as a thermal isolation) and placed in a dense plastic bag, which was completely sealed after installation. Nearby, the rectangular pit was allocated for the box of batteries pre-connected to the desired configuration. The batteries were also oakum-coated and placed inside a double sac, however in this case ventilation was required for the electrochemical reaction to go on. A perforated plastic hose was used as a means of providing necessary oxygen – it was set along the battery block inside and bended above the ground outside to prevent moisture from entering isolated space underground. After installation, connection and testing, the station was carefully buried, with minimal soil pressure on the sensor. Finally, the whole site was camouflaged from wild animals and tourists.

3.2.2 Data pre-processing

Raw seismic records of ground velocity were merged into daily ones and normalized in reference to stationary GRL station. Unfortunately, original instrument responses for temporary station were not available, therefore one had to make this workaround in order to convert digital samples into physical values of $\mu\text{m/s}$. The process of normalization relied on strong (> 5.5 magnitude) and deep (> 100 km hypocenter depth) tectonic earthquakes. In total 20 of such events occurred and were recorded by network during its operational period, making this approach statistically quite reasonable. For a single event we have calculated median ratios between reference GRL station and each temporary one for the absolute values in a time-window containing coda of the event (*Figure 3.8*). The choice of coda instead of P- or S- phase was dictated by its longer duration and therefore wider frequency band of the compared signals, which is important for the study of LP seismicity.

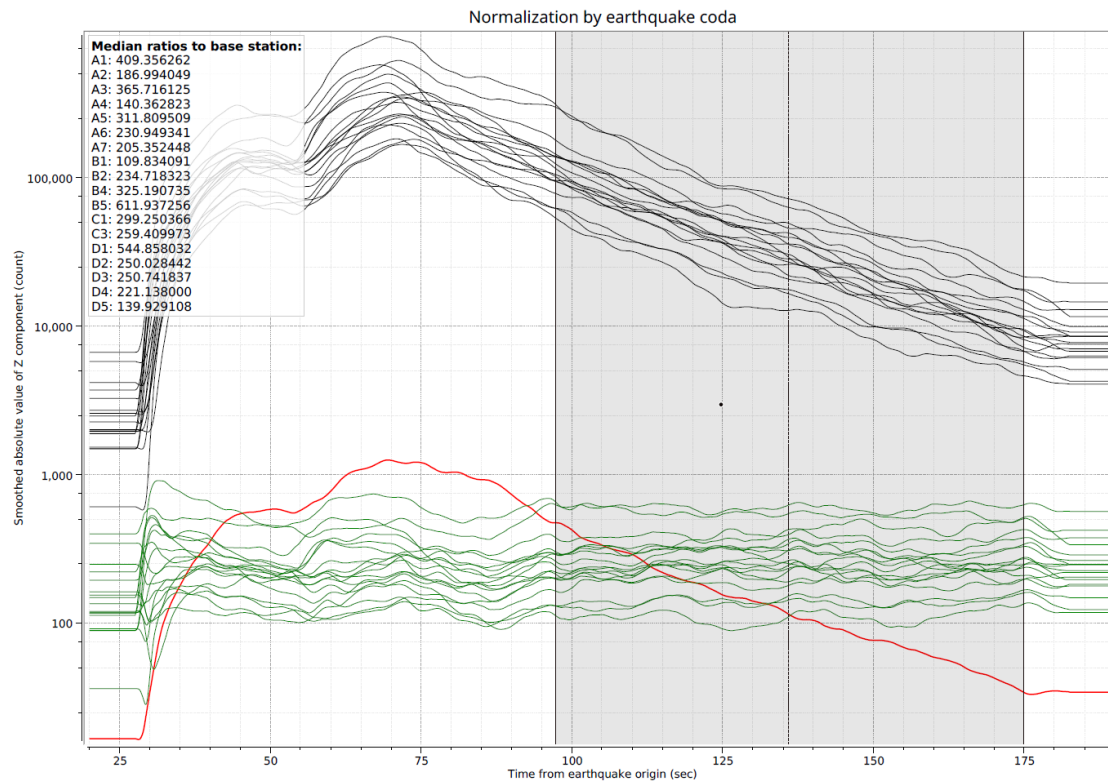


Figure 3.8 Coda-normalization process for a chosen N-S component: an example of high-magnitude tectonic earthquake ($MW > 5.5$, depth > 100 km). (Red line): smoothed absolute values of the component measured at reference station GRL. (Black lines): same for the temporary network stations. (Green lines): ratios between each temporary station amplitudes and the reference station. (Grey area): part of the earthquake coda in which median ratios were computed.

Further basic pre-processing of seismic records normalized to the physical values was done by removing daily mean and linear trend. Finally, a band-pass filter was applied to focus our attention on the part of vibrations that we most interested in. Because Gorely is located only about 30 km from the Pacific shore and frequently visited by tourists, the 1-10 Hz frequency range was chosen to remove most powerful part of oceanic microseisms as well as some anthropogenic noise. This frequency band, however, still allows us to investigate LP volcanic seismicity on Gorely and distinguish it from VT earthquakes (Kugaenko et al., 2011).

3.2.3 Preliminary analysis of seismicity

Preliminary analysis revealed that the dominant part of seismic energy was emitted in form of numerous *long-period earthquakes (LPs)*, which occurred on average twice per minute during most active phases of the degassing episode. Corresponding signals have a duration of about 10-15 seconds long, with energy peaks around 3 Hz. The strong similarity of these waveforms for consecutive events is the most notable feature of the dataset. Even a short example of a 5-minute seismogram during late phase of degassing activity clearly shows this crucial feature of the LPs swarm (Figure 3.9). In this

interval, at least eight events can be visually identified with two of them located next to each other and having almost identical waveforms, as seen in comparison.

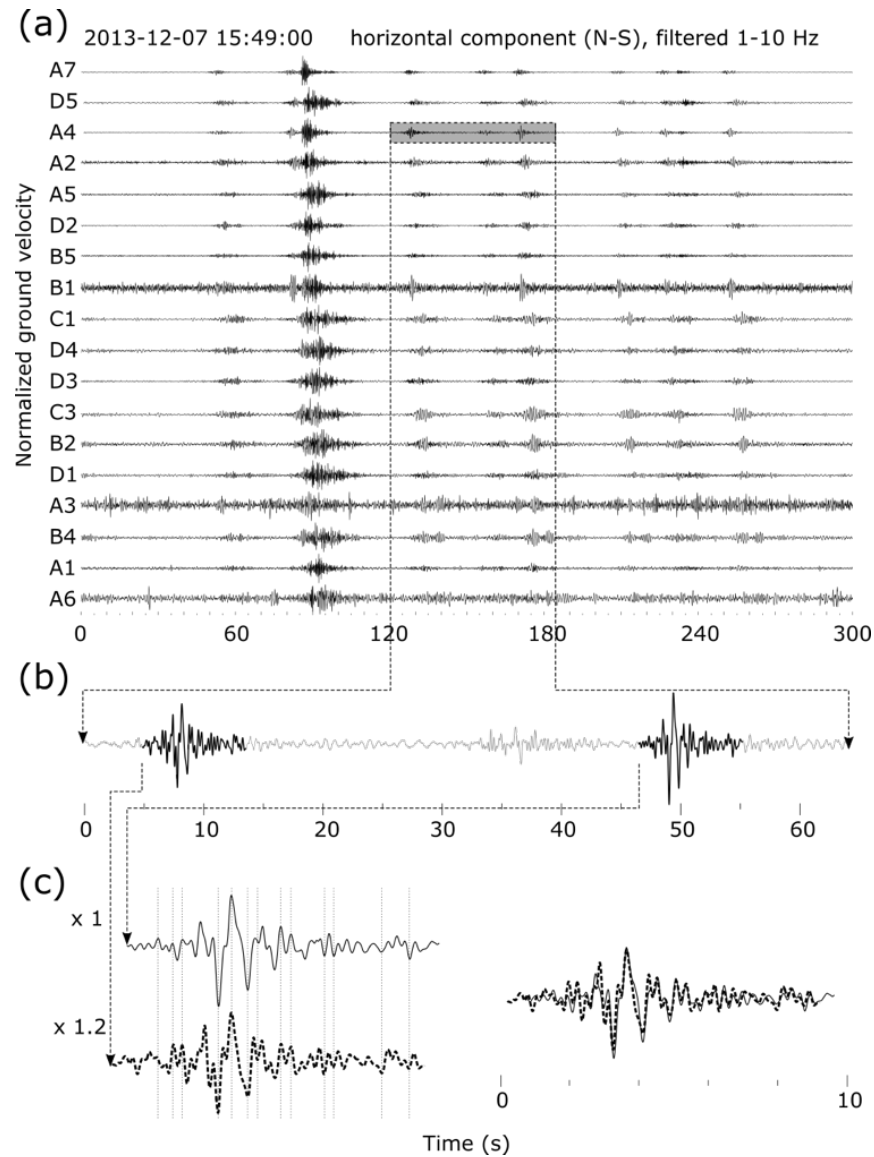


Figure 3.9 Example of the LPs swarm on Gorely during the late phase of degassing process: (a) 5-minute horizontal component records of 18 temporary stations; (b) zoom on representative LP signals at station A4; (c) close comparison of two waveforms.

PART II

STUDY CONTENT AND RESULTS

- *Are these results impressive? Is it enough for a research qualifying a PhD degree?*
 - *Yes, just write and publish it already!*
- A typical PhD student to supervisor conversation*

Chapter 4:

Compilation of Volcano-Seismic Catalog

Following the main goal of this thesis, this chapter opens second part of the manuscript by describing first of three methods used to– the Back-Projection method. The author applied significant efforts in pursuit to mathematically extract the core unifying principle from many modern approaches for automated detection and location of seismic events using networks or seismic arrays. Two closely interconnected sections of the chapter trying to answer this: *what is* back-projection method in essence and *how effective* it is for the compilation of extensive volcano-seismic catalog?

- Section 4.1 is designated to present the basic idea of shifting and stacking that amalgamate widely used seismology methods referred here as back-projection approach and to explain differences in their implementation.
- Section 4.2 is focused on application of the developed algorithm to different subsets of data obtained during Gorely seismic experiment.

4.1 Back-projection based detection and location

The *back-projection* (**BP**) method is a practical approach to detect and locate seismicity by taking advantage of multiple seismic stations organized in a network or array. It is a way to reconstruct seismic source distribution from the recorded wavefield assuming a velocity model defined *a priori*. The key idea is a stacking of seismic records shifted at precomputed travel-times to the theoretical origin points, followed by a grid-search for local maxima of the resulted spatio-temporal function. Several interrelated ‘shift-and-stack’ methodologies have been described in the literature including *semblance analysis* (Tchebotareva et al., 2000), *source scanning algorithm* (**SSA**, Grigoli et al., 2013; Kao & Shan, 2004, 2007; Liao et al., 2012), *coalescence microseismic mapping* (Drew et al., 2013), *beamformed network response* (Frank & Shapiro, 2014), *continuous kurtosis-based migration* (Langet et al., 2014) and even more sophisticated approaches, which lack such fancy naming (ex. Poiata et al., 2016).

4.1.1 General concept of back projection

Let t_* be origin moment of a single seismic event generated at location \mathbf{x}_* and recorded as a set of waveforms $\mathbf{y}(t)=[y_1(t) \ y_2(t) \ ... \ y_N(t)]^T$ by a seismic network¹ with N receivers situated in $\mathbf{R}=[\mathbf{r}_1 \ \mathbf{r}_2 \ ... \ \mathbf{r}_N]^T$. Assuming the correct velocity model $V(\mathbf{x})$ for the study region, one can compute theoretical travel-time $\tau(\mathbf{r}_i, \mathbf{x}_j)$ between each receiver \mathbf{r}_i and a trial source location \mathbf{x}_j , considered the variable (Figure 4.1b). The recorded wavefield $\mathbf{y}(t)$ may be **projected back** to this trial source point kinematically via two essential operations: shifting of seismograms back in time followed by stacking of the resulted traces. The obtained function $p^N(t, \mathbf{x}_j)$ is called the *back-projection intensity (BPI)* – it represents the theoretical potency of a location \mathbf{x}_j to produce seismic interference observed coherently across the network.

In practice, raw waveforms are rarely utilized directly in the procedure of shifting and stacking. Typically, a certain transformation² $\mathbf{u}=\mathcal{U}[\mathbf{y}]: \mathbb{R}^N \mapsto \mathbb{R}_+^N$ is applied beforehand to enhance the desired signal ‘characteristic’ (Figure 4.1a). For the actual source position, each enhanced trace $u_i(t)$ is correctly shifted – therefore, they stack constructively, forming a BPI maximum at the event’s origin time (Figure 4.1c). The same procedure will yield lower intensity values for a different point, with no source active (Figure 4.1d).

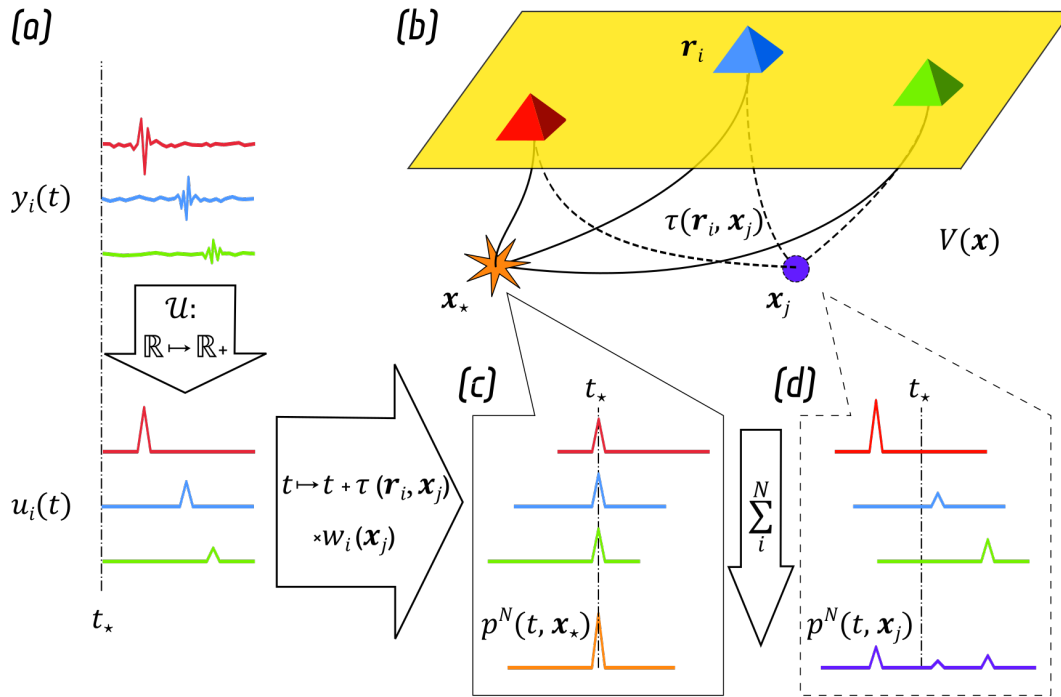


Figure 4.1 – General concept of the back-projection method: (a): characteristic functions calculation from raw seismic data (b): ray-scheme marking two points with precomputed travel-times $\tau(\mathbf{r}_i, \mathbf{x}_j)$ assuming the correct velocity model $V(\mathbf{x})$; (c): back-projection to the actual location of the seismic event; (d): back-projection to the incorrect trial source point.

¹Modern seismic networks and arrays usually consist of 3C instruments. The general concept of back projection is explained here on the example of a single-component network for the sake of simplicity. See the following section for the notes on signal pre-processing.

²More information about characteristic functions in the following subsection.

Performing BPI computations for a grid of trial source points $\mathbf{X} \ni \mathbf{x}_j$ will return a spatio-temporal distribution $p^N(\mathbf{t}, \mathbf{x})$ – an array of time-dependent functions $p^N(\mathbf{t}, \mathbf{x}_j)$. Alternatively, it may be viewed as a time series of *snapshots* (spatial images) $p^N(\mathbf{t}_k, \mathbf{x})$ defined on the grid \mathbf{X} . With assumptions on the correct velocity model and singularity of the event stated above, one may already deduce that the BPI distribution reaches its maximum at spacetime coordinates $(\mathbf{t}_k, \mathbf{x}_j) = (\mathbf{t}_*, \mathbf{x}_*)$. However, the practical efficiency of this approach unfolds in the presence of multiple seismic sources. In such a case, one may treat BPI distribution as a 4D image³, which represents the coherence of a defined wavefield characteristic. Thereby, each snapshot $p^N(\mathbf{t}_k, \mathbf{x})$ quantitatively depicts the likelihood of finding a seismic source inside the study region in a specific time moment \mathbf{t}_k .

It is crucial to summarize the presented concept of BP in a single equation before proceeding to the actual detection and location technique build on its basis. A simple time-dependent BPI definition for a trial point \mathbf{x}_j has the following form:

$$p^N(\mathbf{t}, \mathbf{x}_j) = \sum_{i=1}^N u_i(\mathbf{t} + \tau(\mathbf{r}_i, \mathbf{x}_j)) w_i(\mathbf{x}_j) \quad (4.1)$$

where \mathbf{u}_i represents the result of applied transformation and \mathbf{w}_i denotes the weighting function. Ultimately, the fundamental ‘shift-and-stack’ idea is embodied in two core ingredients of this equation: the substitution of \mathbf{t} by $\mathbf{t} + \tau(\mathbf{r}_i, \mathbf{x}_j)$ and the summation through i .

Incorporation of the BPI calculation inside a grid-search strategy is the final step necessary to build a technique for seismicity detection and location. At the same time, it is the first stage to think of when the developed tool is applied to the study object, as theoretical travel-times must be precomputed for the chosen grid beforehand. However, assuming no changes in seismic velocity disposition over the studying period, this procedure has to be done only once for a selected velocity model. Besides lowering computational cost, it also allows using BP detection and location in real-time monitoring applications.

Velocity model limitation

The main limitation of BP approach arises from a decisive assumption one has to make regarding correctness of the selected velocity model. In essence, BP is an attempt to solve the inverse problem in kinematic approximation. Since it recovers source parameters in a fixed velocity model, the inevitable trade-off between velocity and spacetime position affects results. One should treat obtained detection times and especially locations cautiously. Ultimately, the method provides a sufficient estimation with a cost of non-dynamic approach.

³The full BPI distribution have dimensions of the spatial coordinate $\mathbf{x} = (x_1, x_2, x_3)$ plus one (the time dimension \mathbf{t}), therefore it could be also 3D and 2D.

4.1.2 Implementation to earthquake detection and location

To implement the BP method as a tool for automatic earthquake detection one needs to design three major algorithmic blocks:

1. A way to obtain theoretical travel-times on a predefined grid of virtual source points for the selected velocity model (a solution to the forward kinematic problem of seismology)
2. An actual process of projection computation by determining the signal's transformation and the reasonable weighting factor (a solution to the inverse problem as one may see it)
3. A detection procedure to extract local maxima from the full BPI distribution

It was decided to use the **ray-bending** method (Figure 4.2) for travel-times computations because receivers and virtual sources are fixed in known positions. The corresponding part of the LOTOS code developed by Ivan Koulakov (2009b) is integrated inside the proposed algorithm, enabling a possibility to use complex 3D velocity models as well as less complicated 2D or 1D cases. Alternatively, considering the 'grid-like' task nature, solving the **eikonal equation** (ex. Jeong & Whitaker, 2008) might be an efficient analogue to ray-bending, as one has to perform it only once for each receiver. In the grid nodes representing virtual source points, obtained values would be sought-after times of seismic phase travelling from said sources to the selected receiver due to the equivalence principle.

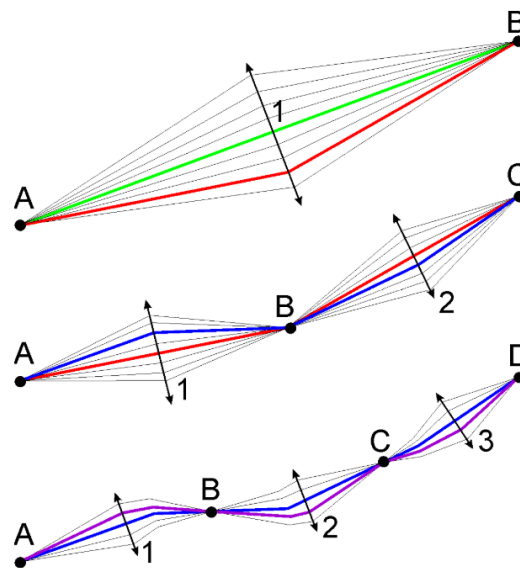


Figure 4.2 – Principle of the bending algorithm for the ray tracing [I. Koulakov, 2009a].

Next, for the BPI computation itself, several methodologies mentioned at the beginning of this section were carefully examined to decide two flavorful ingredients of Eq. (4.1). To a certain degree, the choice of specific $u(\dots)$ and $w(\dots)$ distinguishes one particular BP technique from another.

Characteristic functions

Approaches reviewed in Section 1.2 show that a seismic signal, even from a single one-component station, contains an immense amount of information. By simplifying the seismic activity overview on the appropriate timescale, one may focus on the specific parameter to investigate its dynamics. Even though the detailed seismogram analysis still must be done to understand an individual seismic event's nature, raw data are typically reduced via a single non-linear transformation aimed to highlight ‘character’ of a seismic trace, for example, increase abruptly at the arrival times of a seismic wave (Ludger Küperkoch et al., 2012). In the present study, *characteristic function (CF)* is a broad concept – not limited by a single station or component it can be applied at various seismic processing stages. The RSAM function defined in Eq. (1.1) is a simple instance of emphasizing signal energy while sacrificing information about its phase. Since an appropriate signal parameter choice is crucial for the BPI computation process, several CF candidates were studied. In fact, advanced BP approaches use various functions to deal with different types of seismicity (ex., Poiata et al., 2016).

Trigger algorithms for phase arrivals detection in the presence of stationary and non-stationary noise have a long history in seismology – the possibility to reduce data size was crucial for logging systems at the dawn of digital processing. In the era of immense computational power and inexpensive digital storage, many of these techniques are still used to flag signal segments of particular interest for the subsequent automatic or expert interpretation system (Withers et al., 1998). A generated data stream may be viewed as a CF suitable for the BPI calculation. Implementing such algorithms in various forms is limitless, but the following discussion focuses on only two examples widely used in BP approaches, comparing it to the RSAM and raw seismic records.

Variations of the *short-term average to long-term average ratio (STA/LTA)*, Allen, 1978, 1982) are traditionally used for the auto-picking procedure and phase identification of teleseismic events. Moreover, this detector type was proven to be efficient on a different scale – as part of a convoluted CF in the BP approach used for mining-induced seismicity (Grigoli et al., 2013). In term consistent for CF throughout the manuscript, the simplest version of STA/LTA function may be defined as follow:

$$u^{\text{stla}}(t) = \frac{T_{\text{lta}} \sum_{k=-T_{\text{sta}}/\Delta t}^0 |y(t + k\Delta t)|}{T_{\text{sta}} \sum_{k=-T_{\text{lta}}/\Delta t}^0 |y(t + k\Delta t)|} \quad (4.2)$$

where $T_{\text{sta}} < T_{\text{lta}}$ denote lengths of short and long averaging windows respectively for a seismic trace $y(t)$ with the Δt discretization step sampling. Such a simple representation of the STA/LTA concept is sufficient to discuss this CF's general applicability as intended in this section. One can further improve the statistical independence between STA and LTA by separating them at some delay and further reducing transient effects with the recursive algorithm (Withers et al., 1998).

Among numerous alternative characteristic functions developed since STA/LTA was introduced higher-order statistics claimed to be an effective solution that combines the simplicity of computation and sensitivity for noise-to-signal transitions in seismic data (Gentili & Michelini, 2006; L. Küperkoch et al., 2010; Saragiotis et al., 2002). In particular, *kurtosis* being the fourth statistical moment is another notable CF example used in BP approaches (Langet et al., 2014; Poiata et al., 2016) that measures the amplitude distribution's statistical property in a window relative to the normal distribution (Figure 4.3). Excess kurtosis is a rather controversial nondimensional quantity, which was constantly misrepresented in seismological literature as a measure of 'peakedness', while in fact it is a 'tailedness' of the distribution (Westfall, 2014). In essence, positive kurtosis values signify that amplitudes in the window lacking tail parts compare to a normal distribution (therefore appears to be peaked), while negatives express the opposite case – heavy contribution of tails compare to the central part

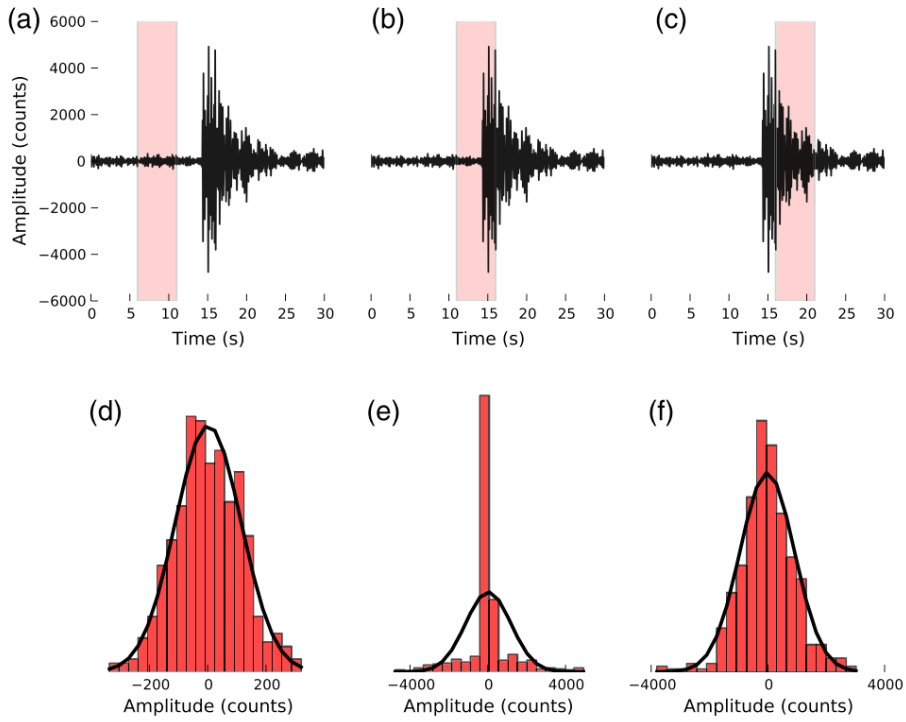


Figure 4.3 – General detection idea of kurtosis function (after Langet et al., 2014): [a–c]: a raw seismic record of an event; [d–f] normalized histograms of the amplitude distribution for each of the three highlighted time windows.

The kurtosis value of a Gaussian distribution equal to 3 is commonly subtracted from the definition itself. In the notation consistent throughout the manuscript kurtosis CF (Saragiotis et al., 2002, eq. 7) looks as follow:

$$u^{\text{kurt}}(t) = \frac{\Delta t}{T_{\text{kurt}}} \frac{\sum_{k=-T_{\text{kurt}}/\Delta t}^0 (y(t + k\Delta t) - \hat{m}_y[t - T_{\text{kurt}}, t])^4}{\hat{\sigma}_y^4[t - T_{\text{kurt}}, t]} - 3 \quad (4.3)$$

where \hat{m}_y represents the signal's mean and $\hat{\sigma}_y$ is its standard deviation in the sliding window of length T_{kurt} , and Δt is the discretization step of the signal – a sampled seismic trace $y(t)$.

Weighting factors

The second ingredient in equation 4.1 represents weighting factor $w_i(\mathbf{x}_j)$ different for each station/channel of a seismic network or array. In most cases, it includes the simplest possible normalization done by denomination on N , allowing comparison of $p^N(t_k, \mathbf{x})$ with a different number of traces used for summation. Similar to the traditional earthquake detection approach, $N \geq 3$ is necessary to get a rough estimation of source parameters. Essentially the recorded wavefield is sampled in receiver locations: therefore, a denser network or array will be preferable in terms of data coverage translating to a higher resolution of the resulted projection. However, in a situation where the assumed impact of different stations to the obtained value of BPI varies throughout trial source points, one should think about weighting in a more convoluted manner.

Contrary to the rather straightforward RSAM, the reduced displacement represents a more sophisticated CF combined with normalization across different source-receiver pairs. Similar to Eq. 1.2 one may define the nondimensional geometrical spreading correction terms as weighting factors for both spherical (w^{bgs} – body waves) and cylindrical (w^{sgs} – surface waves) wavefront propagation:

$$w_i^{\text{bgs}}(\mathbf{x}_j) = \frac{l(\mathbf{r}_i, \mathbf{x}_j)}{L} \quad (4.4)$$

$$w_i^{\text{sgs}}(\mathbf{x}_j) = \frac{\sqrt{l(\mathbf{r}_i, \mathbf{x}_j)}}{\sqrt{L}} \quad (4.5)$$

where $l(\mathbf{r}_i, \mathbf{x}_j)$ is the distance between virtual source point \mathbf{x}_j and receiver \mathbf{r}_i . The parameter L making this correction term nondimensional and should be treated with caution as it directly scales the resulted absolute value of BPI.

Algorithm structure

First, the trial source points grid \mathbf{X} is defined in 3D cartesian space containing the study region with margins of at least one point in each direction. These margin points are used to compensate for the artefacts during detection procedure as seismic sources active outside this region would focus BPI local maxima on the grid edges. In this preliminary stage, the selected velocity model is utilized once to compute travel-times from virtual source points to the network stations. The precomputed times are stored as vectors defined in grid nodes. Next, the chosen CF is computed for each channel/station from the pre-processed seismic records. The following computation of BPI values may be done simultaneously for each grid node – this fact allows parallelization of the most computationally heavy part on a multi-core CPU or GPU.

Finally, the compressed BPI $p^N(t)$ is arranged from the full spatio-temporal BPI distribution $p^N(t, \mathbf{x})$ as a maximum value in space for each time moment:

$$p^N(t) = \max_{\mathbf{x}_j \in \mathbf{X}} [p^N(t, \mathbf{x}_j)] \quad (0.6)$$

to operate as a simple detector function. By scanning through $p^N(t)$ in time for local maxima larger than a threshold value P^N , one can effectively obtain detections $\{\tilde{t}_k\}$ that correspond to the full BPI distribution local maxima. Computing the time interval between two nearest local minima for respective maximum returns an approximate value of the signal duration \tilde{t}_k . The snapshots of BPI distribution corresponding to the detection are used to estimate source location in 3D space. One should check if snapshot maxima are observed in margin grid nodes – it will signify that the real origin location for such an event is probably outside of the actual study region. In conjunction with the estimated signal duration, it may be used as a criterion to exclude ambiguous detections and focus on specific seismicity inside the study region.

4.2 Application to Gorely's temporary network data

Almost one year of seismic data recorded by the temporal network on Gorely contains numerous *long-period earthquakes* (**LPs**, see Subsection 3.2.3). Such dense seismicity making manual identification and analysis of individual events practically inefficient. The BP approach and its implementation for earthquake detection and location described in the previous section opened the possibility for the automated compilation of specific volcanic seismicity catalogue.

4.2.1 Algorithm parameters tuning

One must make necessary preparations and tune algorithm parameters for the particular study object, observation scheme, and the chosen type of seismicity before the whole dataset's processing. The synthetic testing can answer some questions on the approach applicability in general. However, only the close analysis of results obtained for the real dataset may prove the approach efficiency in a particular case. The chosen dataset may have a relatively short duration, but it must represent acquisition conditions and most importantly contain signals of the targeted seismicity type. The tuning process itself essentially requires setting up parameters for three major algorithmic blocks described in Section 4.1.2.

As the main limitation of the BP approach, the assumed velocity model choice is the most crucial preparational step of the proposed technique because it dramatically affects the resulting locations. Fortunately, even homogeneous velocity model seems to be sufficient for the detection purpose giving that the chosen grid size and velocity value provide the range of travel-times large enough to achieve BPI maxima in some trial source points. Obtained locations cannot be treated as the absolute position of detected sources, but rather must be viewed as rough relative estimations.

Selection of the characteristic function is directly linked to the type of detected earthquakes. Kurtosis and STA/LTA functions used in trigger algorithms have proven to be a compelling CF for seismic signals with sharp onsets and signals containing distinguishable seismic phases. Thus, it is a reasonable choice for VT earthquakes, for example. The lack of precise arrivals observed in LPs on Gorely making an energy-based CF like RSAM more preferable.

Similarly, the choice of weighting factor is partially dictated by the supposed type of waves that constitute targeted seismicity. Most importantly it depends on the observation scheme. For dense seismic array, one may be satisfied with simple normalization of BPI value via division on the number of receivers, giving that the interstation distance is substantially smaller than the distance to assumed

sources. However, the Gorely seismic network design coupled with the supposedly shallow nature of seismicity urges to use weighting factor depending on the trial source location.

Finally, the last algorithmic block requires two parameters to acquire actual detections automatically. Particular values for both parameters are decided subjectively during algorithm testing on a representative subset of data. The detection threshold defines a value of BPI maximum that must be reached for an event to be marked as ‘detection’. Thus, the test dataset must contain a wide amplitude range of signals for the targeted seismicity type, including those for the chosen minimum amplitude. For a typical regional tectonic earthquake located outside the study region, $\tilde{\tau}_k$ tend to be significantly larger than it is for targeted LPs. Therefore, setting a limit T^N on the event duration allows one to filter out unrelated seismicity. After multiple trials on the test subset of real data parameters for the algorithm were set as presented in Table 1. One may see an example of the detection process for the isolated high-energy LP earthquake in Figure 4.4.

Table 1 Parameters of the BP detection and location algorithm

Algorithm parameter		Chosen value/function
\mathbf{X}	Trial source points grid	20 km x 20 km x 10 km
$V(\mathbf{x})$	Velocity model	$V=1.5$ km/s
$u(\dots)$	Characteristic function	$u^{\text{rsam}}(t), T_{\text{rsam}}=3$ s
$w(\dots)$	Weighting factor	$w^{\text{sgs}}(\mathbf{x})$,
P^N	Detection threshold	$2 \mu\text{m/s}$
T^N	Duration limit	16 s

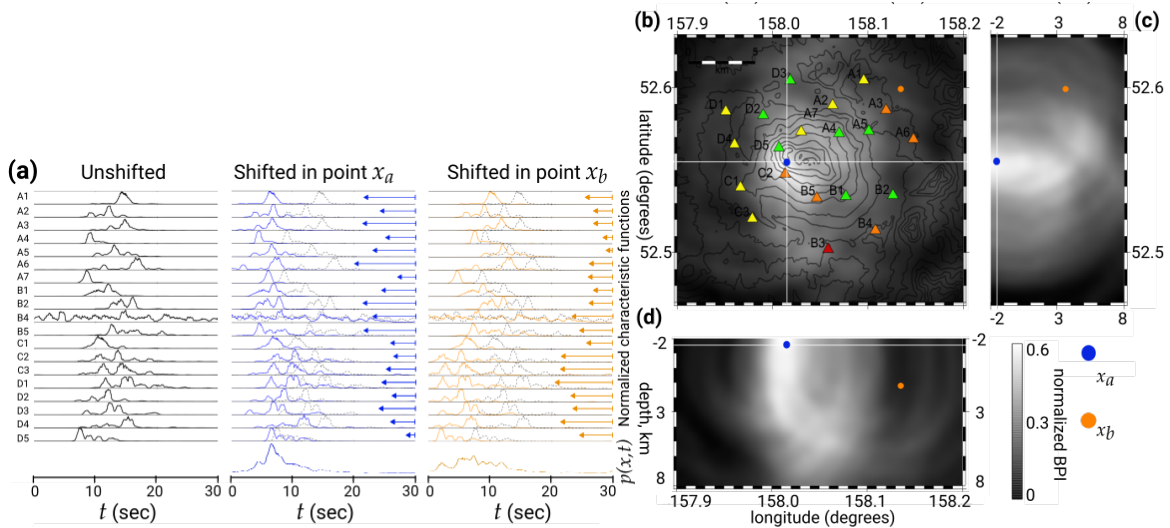


Figure 4.4 – Example of the BP detection procedure for a high-energy LP event on Gorely: (a) signal envelopes (CFs) shifted according to precomputed travel-times; (b) horizontal, and (c) (d) two vertical slices of 3-D BPI snapshot for a time of local maximum in detector function.

4.2.2 Results for different network conditions

Acquisition conditions on Gorely were changing throughout the year: the total number of functioning stations steadily decreased from eighteen in the first three months of observation to only five in the last two (Figure 3.6). However, the proposed BP-based technique treats the number of used stations as a constant for the chosen duration of data processing. In other words, the observational scheme is fixed for a single detection and location procedure. The solution to changing acquisition conditions on Gorely is to simply treat varying number of functioning stations as different observational schemes and compare results between them for the corresponding period.

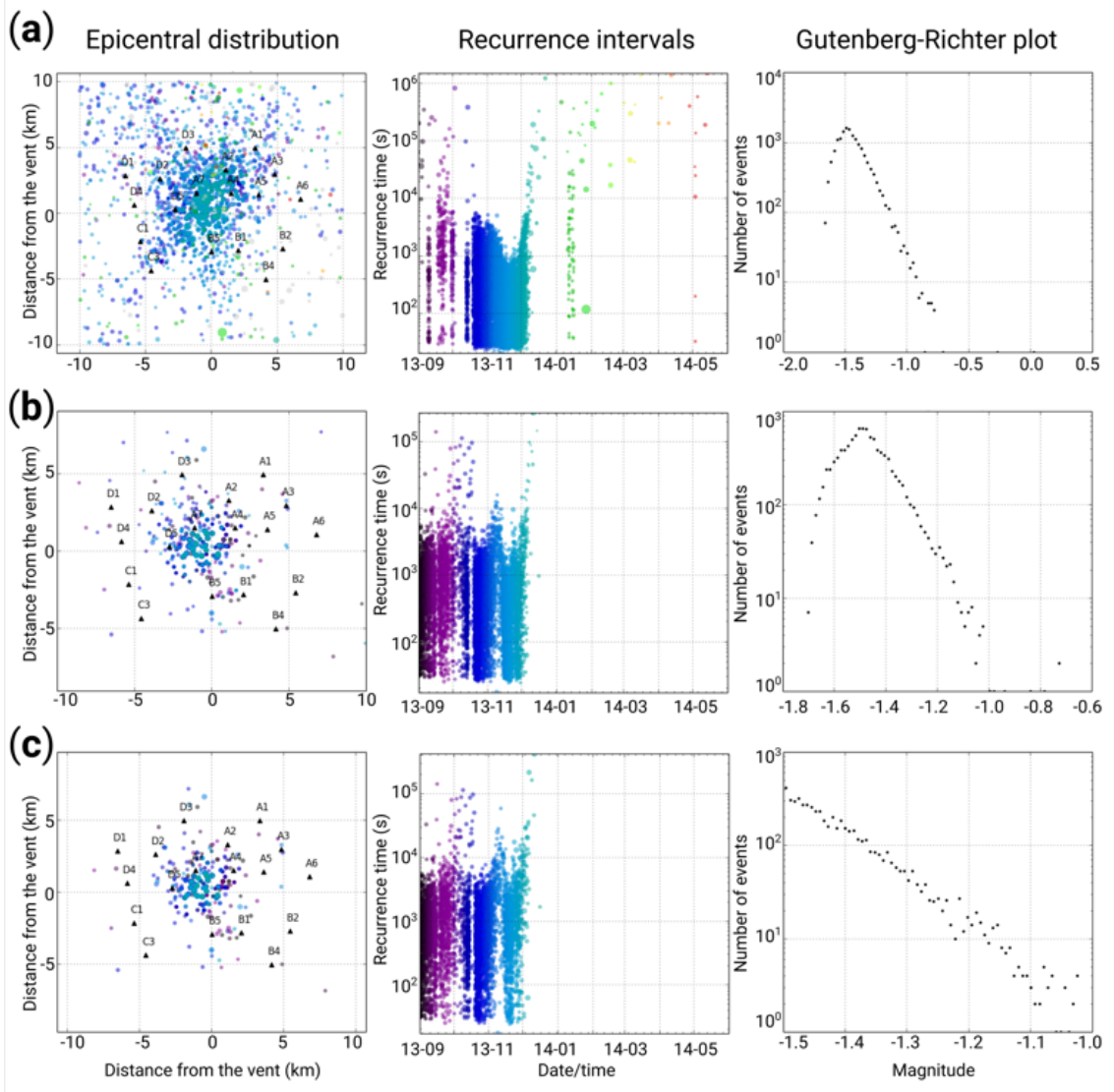


Figure 4.5 – Results of applying the BP detection algorithm to Gorely data: (a) detections acquired using records of 5 temporary stations which functioned 9 months; (b) same for 18 stations working during the four starting months, when degassing activity was exceptionally strong; (c) filtered detections obtained with 18 stations, which follow Gutenberg-Richter law and constitute BP-based catalogue.

The BP detection technique was implemented to build a catalogue of LP earthquakes beneath Gorely using two subsets of data. The detection procedure was performed for nine months of data available at five most consistent seismic stations with the event detection threshold $P^5=2 \mu\text{m/s}$ (Figure 4.5a). This result showed that the significant number of detections is condensed in first four months of the observation period, with only a minor activity after. For this period of intense degassing, the data from 18 stations was utilized to build a more robust catalogue of 9691 detections (Figure 4.5b). The BPI procedure with a more conservative threshold value $P^{18}=4 \mu\text{m/s}$ led to the catalogue size decreasing down to only 1741 most energetic events (Figure 4.5c). These results bear similar characteristics of seismicity in time for both low and high energy parts of the catalogue. It is also apparent that after December 7th, the activity on Gorely was rapidly decaying.

Chapter 5:

Waveform-similarity based cluster analysis

In general, cluster analysis is the task of grouping similar objects together. It could be also viewed as a way to divide initial dataset on several subsets in which data points are close to each other by some similarity measure. This technique is used in various applications throughout many scientific fields including bioinformatics, image analysis, machine learning, data compression and all sorts of data exploration. In the present study dataset is a catalogue obtained via back-projection detection and location algorithm. Naturally, a data point in this case contains all the information about a detected earthquake: origin time, BPI value, estimated location, duration and most importantly its waveforms.

5.1 Catalog inspection via correlation coefficient matrix

The catalogue obtained with BP detection and location algorithm for Gorely's degassing episode from 2013 August 28th to December 18th contains 1741 high-energy earthquakes (*Figure 5.1* in black corresponds to *Figure 4.5c*). It was further investigated via proposed cluster analysis technique based on earthquakes waveforms similarity.

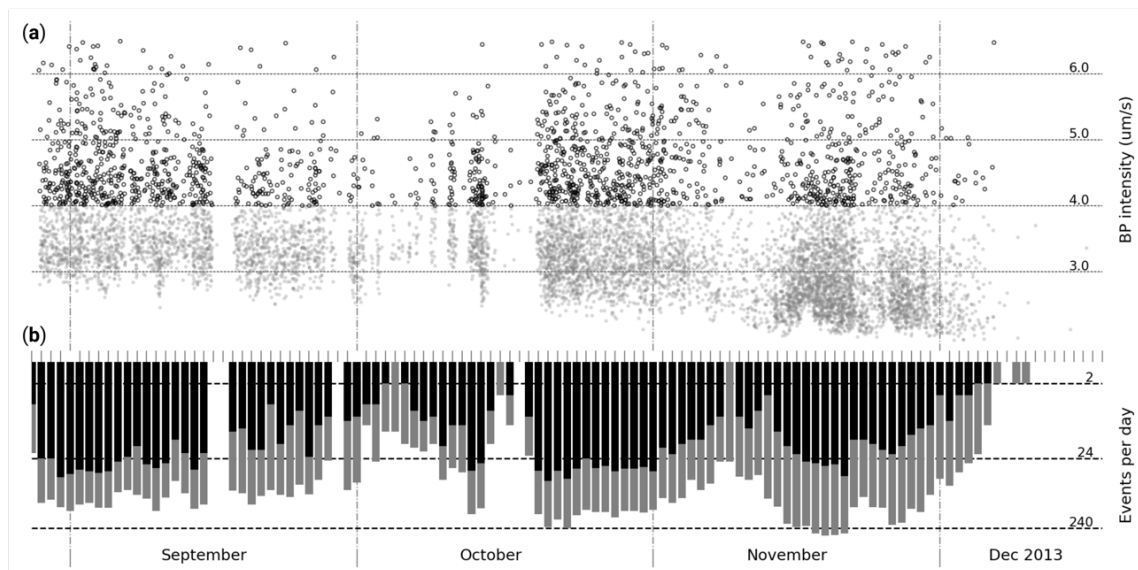


Figure 5.1 – The BP-based catalog of high-energy events (in black, $P^{18}=4 \mu\text{m/s.}$) and all initial detections (in grey $P^{18}=2 \mu\text{m/s.}$): (a) BPI values for each detection with a size proportional to magnitude; (b) daily rate of detections.

The waveforms extraction process and similarity quantification between pairs of detected earthquakes following the procedure proposed in the article dealing with swarms of repeating long-period earthquakes at Shishaldin Volcano in Alaska (Petersen, 2007). The process of cluster analysis itself was inspired by a version of *k-means* method (a centroid-based clustering) suggested for the seismic classification of volcanic tremors in Kamchatka (Soubestre et al., 2018).

For each pair of detected earthquakes in the catalogue corresponding waveforms for each station are cropped to a time window of length T^N after the respective origin time. The similarity of two earthquakes j and k is defined as a *correlation coefficient (CC)* computed for each pair of their waveforms recorded by the same station averaged through the whole network allowing for the time shift to reach maximum averaged CC value across network. To see the relationships between all events, one may plot these coefficients as a matrix, where each row or column reflects how similar the selected earthquake to the other ones in the catalogue.

Despite the general similarity of all detections in the BP-based catalogue, some subgroups of earthquakes can be distinguished from the visual analysis of the CC matrix (*Figure 5.2a*). It is possible to distinguish from four to six square patterns of high CC values along the main diagonal. Such squares indicate a group of similar events localized in time because detections are sorted sequentially in time by default. Some of the ‘squares’ are prolonged to off-diagonal part, also suggesting the existence of subgroups inside a bigger class. The number of groups with different properties can be approximately identified by estimating the degree of complexity that CC matrix possesses, which can be done by computing its eigenvalues. The resulted distribution of eigenvalues ranged in the decreasing order (*Figure 5.2b*) appears to have only a small part of the first eigenvalues large enough, while the rest is close to zero. Taking into account only eigenvalues that are larger than 5 % of the maximum one, it is estimated that there are five meaningful earthquake groups in the catalogue.

Figure 5.2c presents the average CC of a detected earthquake with all other 1740 detected events. The majority of them have the CC between 0.3 and 0.4 showing relatively high similarity within the whole catalogue. At the same time, there are four outlier detections having the correlation of around 0.1. Manual inspection of event waveforms identified that these are relatively short-duration VT earthquakes, which have completely different waveforms compared to those of LPs that constitutes the catalogue main bulk. It does not mean that no other VT events occurred during the studied period but rather that used parameters of the BP detection and location algorithm were specially adapted for LPs searching (reference velocity, time window, frequency of filtering). Thus, after excluding these four VT events, a verified initial catalogue of the LP earthquakes contained 1737 LPs with the highest energy.

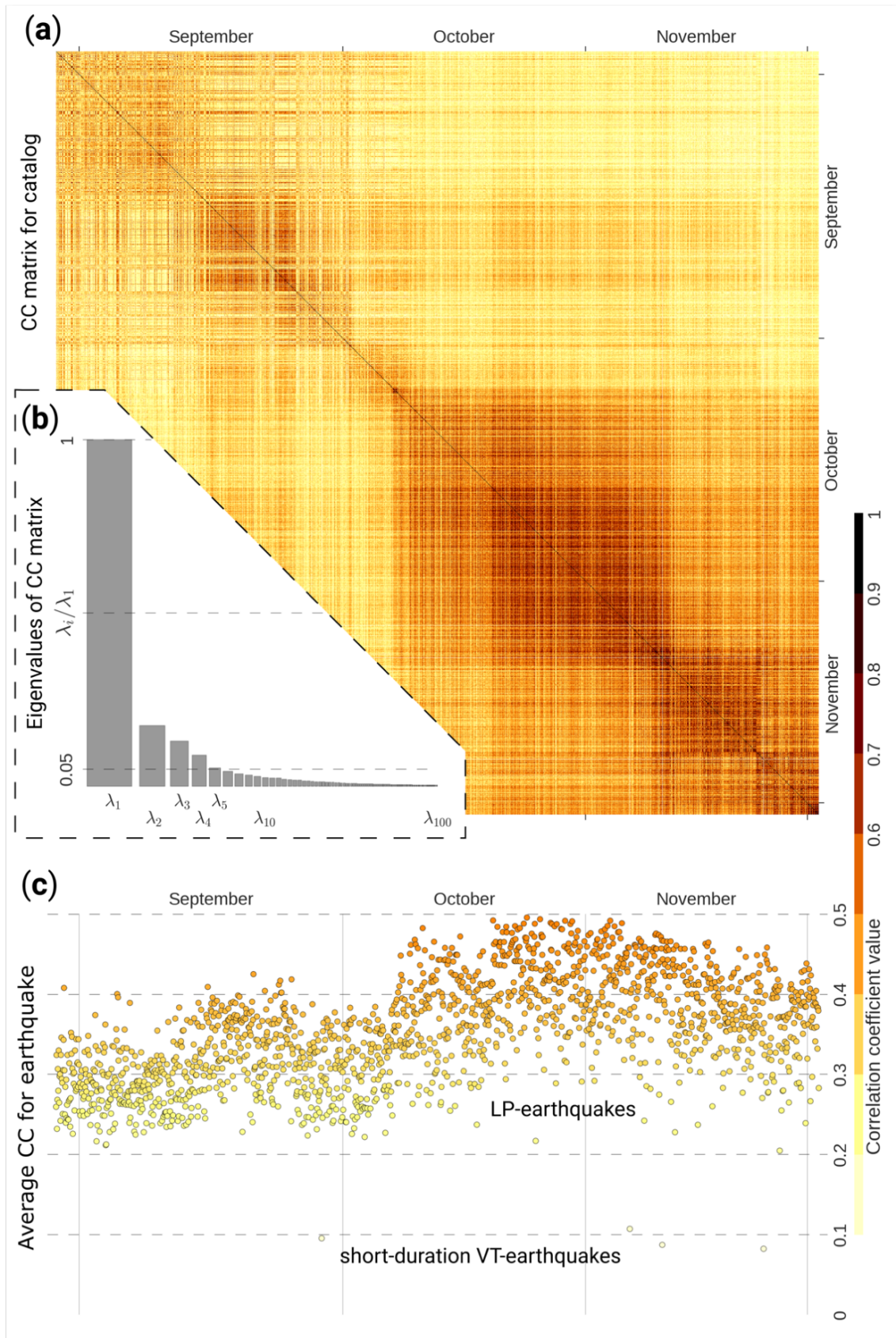


Figure 5.2 – Similarity assessment of earthquakes from the BP based catalog: (a) waveform-based CC matrix; (b) first 100 eigenvalues of the matrix - sorted and normalized; (c) the average similarity for each earthquake inside the catalogue. Note that there are four average CC outliers - verification of the waveforms confirmed that these are VT earthquakes with similar to LP duration and amplitude.

5.2 Clustering process

To separate all detected LPs in five groups, we followed the iterative approach described in (Soubestre et al., 2018). To find out a reasonable partition of initial clusters, we consequently excluded groups of similar earthquakes from the catalogue. First, we calculate a mean average CC for every single earthquake with all other events across the whole catalogue, as shown in *Figure 5.2c*. Next, an earthquake with the maximum average CC is taken as a master event for the first group. All events having the CC with the master event larger than a particular threshold are excluded from the catalogue to form the first cluster. The procedure is repeated for the rest of the catalogue: on each step earthquake with maximum average correlation is taken to form the next initial cluster that is excluded from the catalogue until we get all N_c clusters.

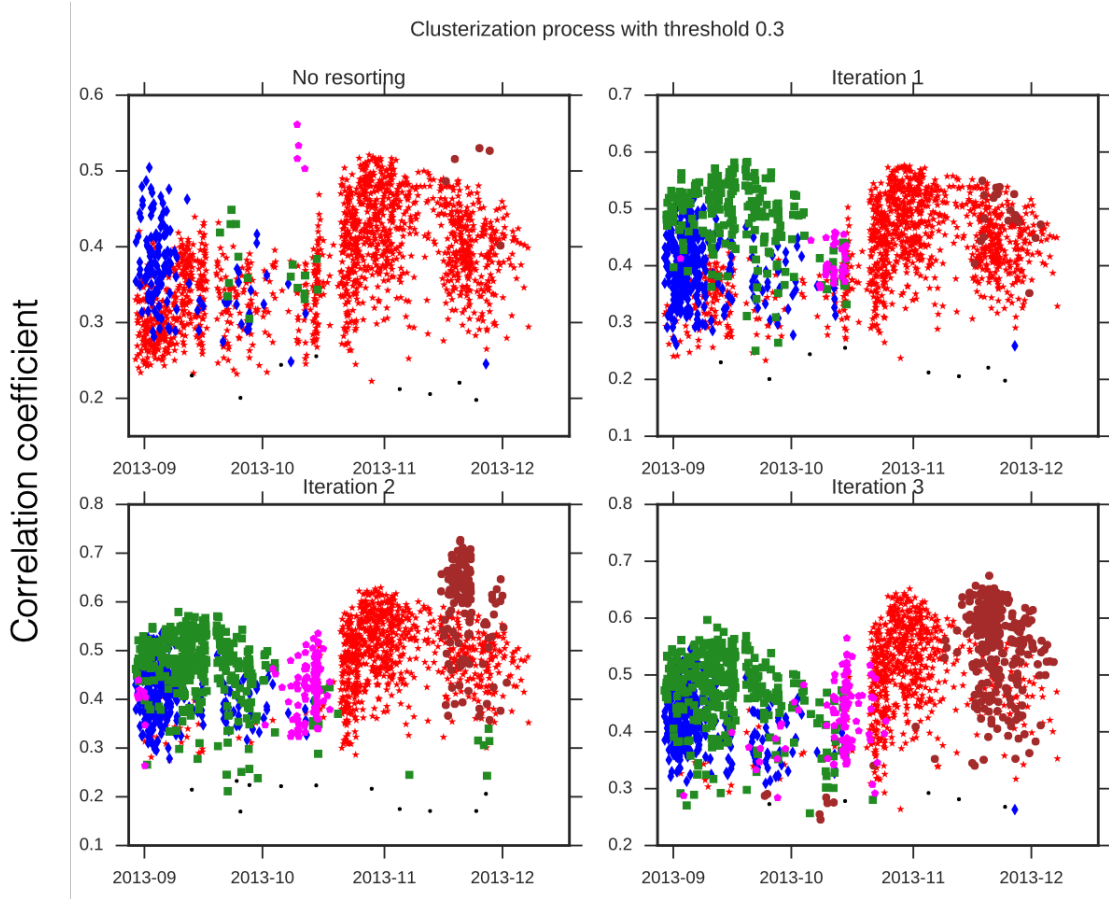


Figure 5.3 – Clustering process for 1741 high-energy earthquakes of BP-based catalog with threshold of 0.3 converges to five stable clusters (marked by colors) after three resorting iterations.

After initial selection of clusters, master events are close enough to the earthquakes in their respective groups while staying far from the other master events. Depending on the chosen threshold, the entire catalogue may be completely divided into N_c clusters, or some earthquakes may still stay ungrouped. The defined clusters iteratively resorted in accordance with the CC matrix which acts as

matrix of inverted distances between data points in terminology of K-means approach. On each iteration, we first asking every grouped event for its CC to all current master events and place it in the group where it has the highest similarity to the corresponding master event. After that, the new master event for each cluster is determined by computing a new vector of the mean similarity from its cluster and picking the one with the maximum value. As a result, a stable cluster distribution is reached after several iterations. Because this method converges to a local minimum, the final result depends on the initial cluster's starting 'centers' (master events). Reasonable choice of the starting cluster composition via excluding them from the catalogue helps form highly diverse clusters.

We performed described cluster analysis with the CC threshold of 0.3 and found that it converges to the stable distribution after the 3rd iteration (*Figure 5.3*). The CC values within the five groups and their time distributions are shown in *Figure 5.4a*. It can be seen that the CC values within distinct groups are higher than CCs with all events shown in *Figure 5.2c*, which demonstrate the adequacy of such classification of events. Final clusters are sequentially arranged in time that may indicate the possible evolution of seismic source properties or changes in the seismic velocity structure of the volcano.

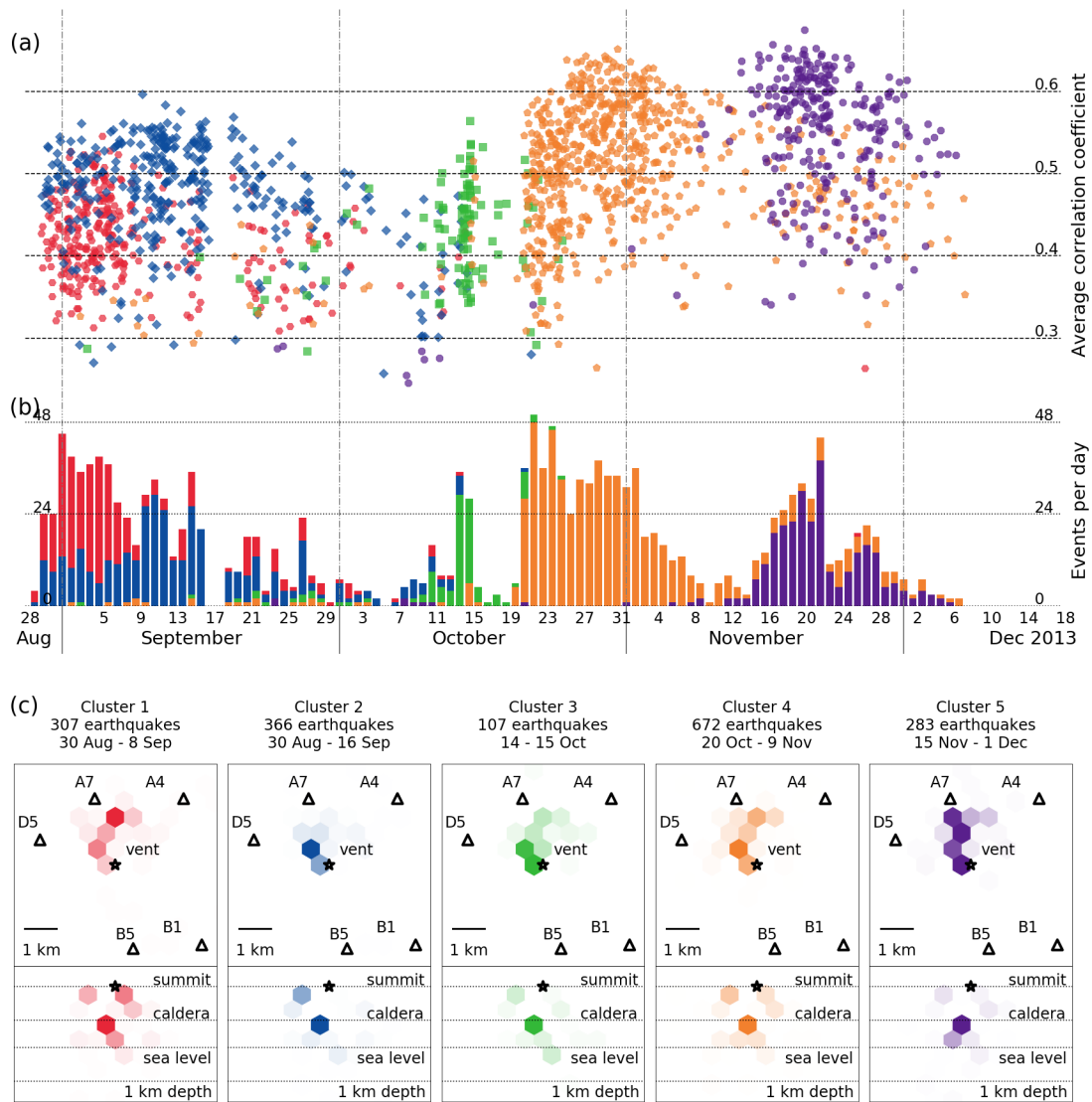


Figure 5.4 – Cluster analysis results for the BP based catalog. In all panels, the different colors indicate five identified clusters. **(a)** Average correlation coefficients for the final distribution after the 3rd iteration with five sequential clusters. **(b)** A daily number of events for different clusters. **(c)** Hexagonal plots of the events space distribution for each cluster projected to map view (upper row) and to vertical section oriented in west-east direction (lower row). Each hexagon presents confidence area of the location, while color intensity reflects normalized number of the events in this location.

Chapter 6:

Catalog extension via template matching

The closing chapter is focused on presenting final result of the study an extensive verified catalog of long-period earthquakes on Gorely and the proposed interpretation for the observed seismicity behavior.

- Section 6.1 describes the template matching method to detect events with the waveforms similar to 5 discovered clusters of LP earthquakes.
- Section 6.2 presents results of this method application to Gorely continuous data for the active degassing phase.
- Section 6.3 contains discussion about possible physical mechanisms explaining the observed character of seismicity and suggested interpretation of the resulted catalog.

6.1 Template matching method

The results of the cluster analysis allow us to create a set of templates that reflect common waveform features for all earthquakes in a certain group of the catalogue. We create the cluster templates by stacking waveforms with the weights equal to their correlation coefficients. Thus, for the i^{th} receiver, the resulting template waveform of the k^{th} cluster is computed as follow:

$$z_i^k(t) = \frac{\sum_{j=1}^{N_c} c_j^k y_i^j(t)}{\sum_{j=1}^{N_c} c_j^k} \quad (6.1)$$

where $y_i^j(t)$ is a waveform of the j^{th} event inside the cluster, c_j^k denotes event-to-master CC, and N_c stands for the cluster size. Stacking increases signal-to-noise ratio so that we may treat the template as a fingerprint of a composite event with the common source mechanism for all events in the corresponding cluster. Because a template represents a generalized image of a cluster, we can compare it to another one visually and numerically by calculating CCs between them. In *Figure 6.1*, we show examples of the composite waveforms in some stations corresponding to the selected five groups of events.

We can use the constructed templates to search for other earthquakes, similar to ones selected for the corresponding clusters. The template matching (TM), which we use to detect multiplets (Gibbons & Ringdal, 2006), has become the standard way to identify families of tectonic low-frequency earthquakes (Bostock et al., 2012; Frank et al., 2013, 2014; Shelly, 2009; Shelly et al., 2006) and volcanic LP earthquakes (Shapiro et al., 2017). The algorithm essentially matches a defined template of seismic event with continuous seismograms by computing CCs between the template and waveforms in a sliding window. Comparing the derived time-dependent CC with a predefined threshold, one can identify all events with the waveforms similar to the template, which creates a more extensive catalogue. Depending on the template-to-template similarity and chosen threshold, the same event can be detected with different templates. In these cases, we attribute such events to the template group having the highest CC. Unlike the BP technique, the TM approach is sensitive to the shape of seismic signals rather than its amplitude so that we can form a complementary catalogue of low-energy LPs.

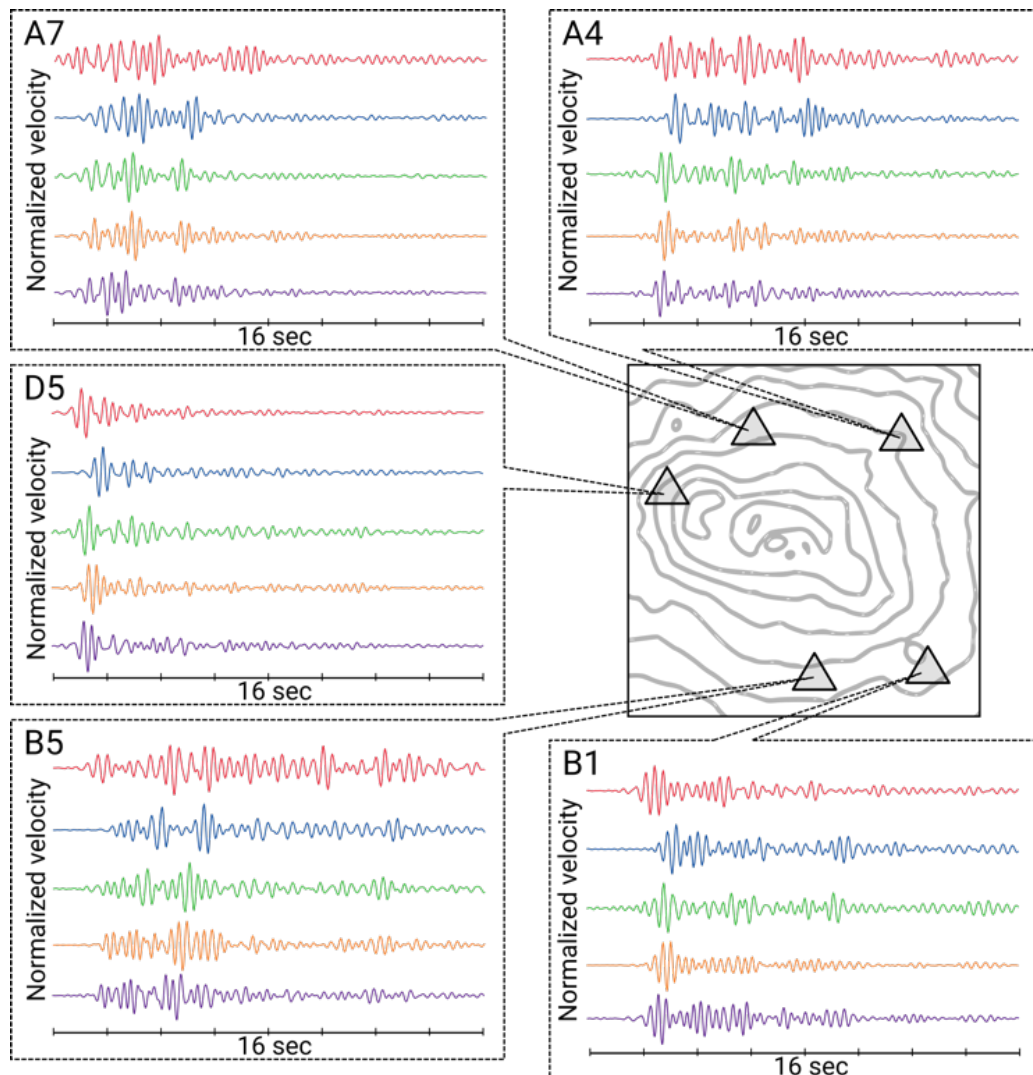


Figure 6.1 – Template waveforms for five closest to summit stations. Colors as on Figure 5.3 show evolution of the template waveform for 5 well-defined clusters.

6.2 Seismic characteristic of the degassing episode

For more than 3 months of Gorely's degassing episode, we were able to identify 80,615 LP earthquakes divided into five clusters. The time distributions of these events can be compared with high-energy events of the initial catalogue in *Figure 6.2*. Cluster analysis of the BP-based catalogue has demonstrated the limited variety and high repetitiveness of LP seismicity that was taking place beneath Gorely in the observation period. In total, we have identified five distinguishable families of LP earthquakes, which were sequentially arranged in time. In *Figure 5.3*, one can see the final distribution of high-energy LP earthquakes that gives us insight into the development of the conduit structure over time.

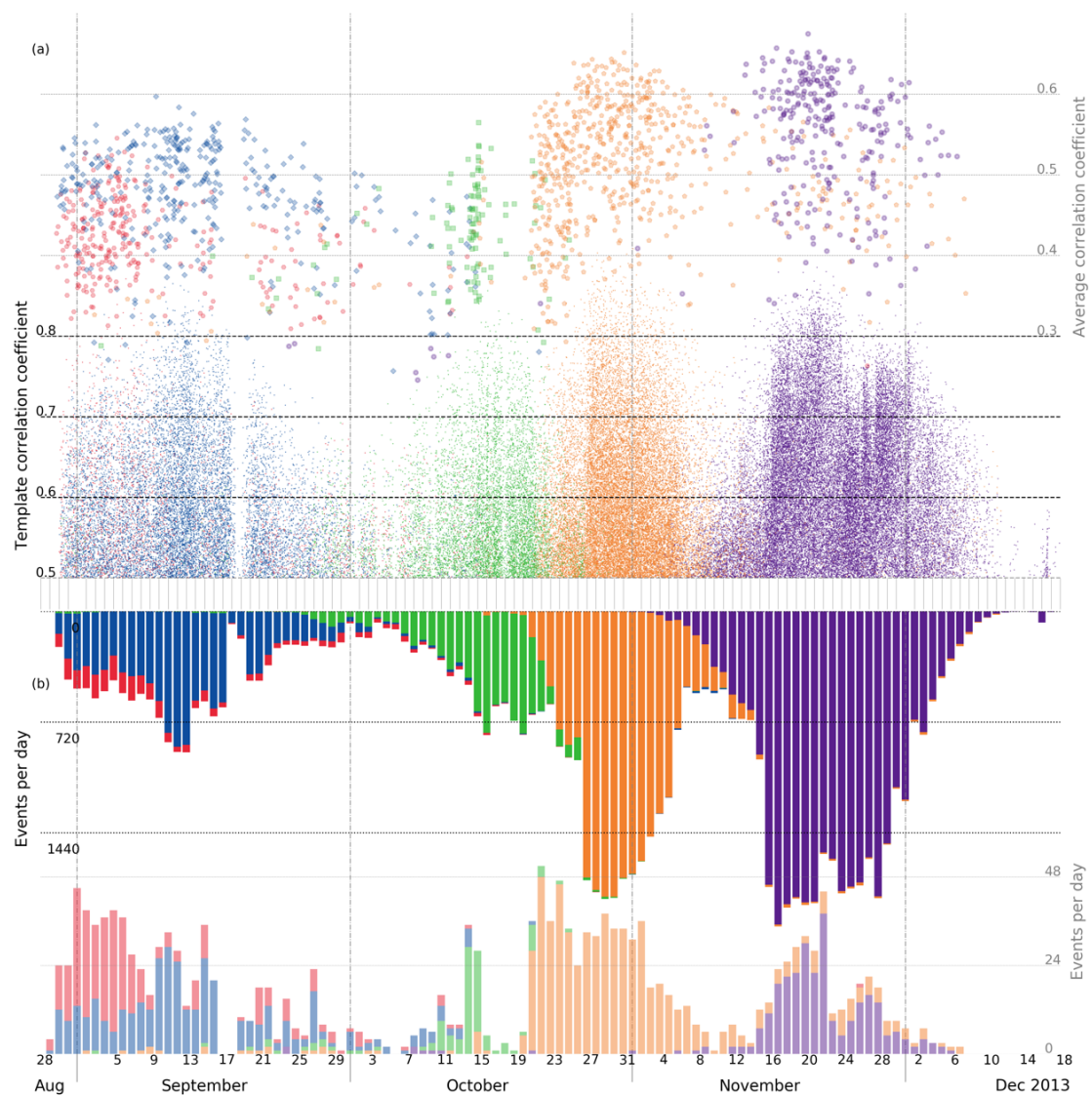


Figure 6.2 – The MF-based catalogue of lower-energy events in comparison with cluster analysis results for the BP-based catalog containing most-energetic earthquakes (in pale colors): (a) CCs for both catalogs (note that these are not the same type); (b) time distribution of the events daily amount. Colors again indicate cluster to which detection correspond (as on Figure 5.3).

At the beginning of the observation on August 28th, we see that the “red” family was dominating. By September 9th, its intensity has incrementally decreased, as it was gradually replaced by the “blue” family, which in turn reached the maximum on September 10th and then weakened during a couple of weeks in the same manner. Between October 3rd and 7th, there is a gap in the LP seismic activity. Between October 9th and 16th, a short-lived peak of the “green” family activity was followed by another gap on October 16-18. On October 20th, the “orange” family abruptly started to produce the largest group of the LP events, whose activity gradually increased until November 9th. After another short gap, the last “violet” family started on November 13th, reached its peak on November 22nd, and then completely decayed by December 6th. After this moment, LP activity only occurred infrequently.

The extensive TM-based catalogue provides additional information about the evolution of Gorely’s degassing system. As one may see in *Figure 6.2*, lower-energy events are repeating the same pattern as their high-energy counterpart. However, there are fewer gaps in the activity, and the transitions between LP earthquake families are much smoother. Other differences are the domination of the “blue” family over the “red” one, considerably prolonged duration of the “green” period and the minor burst of detections on December 16th.

6.3 Interpretation

Each LP earthquake family produced a series of nearly similar signals emitted from a localized source region. These source regions were located beneath the volcano summit at depths of less than 1 km below the surface. In the recent tomography study of Gorely (Kuznetsov et al., 2017), the top of the prominent anomaly, representing the magma chamber, was located at ~2.5 km below the surface. The interface between very high Vp/Vs in the magma chamber and low Vp/Vs in the overlying carapace is interpreted as a level of the phase transition in the molten magma. We suppose that dissolved fluids were degassing at this stage due to lower pressure in the shallower part of the magma reservoir. The LP earthquakes identified in our study may indicate the following pathway of ascending high-pressure gases. The rapid degassing and fast dynamic propagation of gas bubbles through the conduit root may lead to self-sustained oscillations within the magmatic channel (Julian, 1994), generating the LP radiation recorded by seismic stations. It is possible that at some moment, the conduit structure changes, resulting in new oscillation parameters and characteristics of repeated LP events. Therefore, the observed evolution of LP earthquakes may reflect the structural changes in the shallow part of the volcano-magmatic system.

Alternatively, given generally shallow levels of LP radiation on Gorely, groundwaters may be involved in two-phase ‘steam and water’ resonator system in a similar way that was proposed for

Ngauruhoe volcano in New Zealand (Jolly et al., 2012; Park et al., 2019). The climate of Kamchatka with a heavy snow cover of volcanoes over a half-year and the glaciation of Pra-Gorely caldera both support this version. However, the chemical content of gases and the rate of Gorely degassing implies that the proposed bubble-dynamic mechanism of LP is primarily caused by dissolving magmatic fluids in the conduit root.

We see that only at the beginning of the observation period, two of LP earthquake families (the “red” and “blue” one) functioned at the same moments with about similar intensity of the high-energy events. In other periods, only a sole family is dominating at the time, which is apparent in the MF-based detection distribution (*Figure 6.2*). It probably means that the preferable degassing regime of Gorely requires only one conduit acting at a time. Smooth transitions in the number of detected events between families (*Figure 6.2*) and the structure of CC matrix (*Figure 5.2a*) imply that each dominant family gradually evolves into the next one. This may be interpreted as the slow migration of the source along a constricted pathway of magmatic gasses ascent. Close likelihood of template waveforms for master events of “blue”, “green”, “orange” and “purple” families also support this point, while “red” one represents alternative explanation. The co-existence of two LP families acting in the same period (but not simultaneously) may be interpreted as the balancing stage of the gas ascent process. In such conditions, the pressure gradient allows only a portion of gas bubbles to overcome constriction in the “blue” family origin point, while the rest of the gasses have to proceed laterally (*Figure 5.3c*) to the “red” family origin point.

Finally, combining information about physical models presented in Section 2.2, we propose an interpretation of the observed seismicity linked to the degassing process. First, the flow-induced oscillation model requires incompressible fluid, which is likely not the case for the Gorely gas eruption. While both fluid-filled crack model and cylindrical conduit resonance model may explain observed features of LP seismicity, we decided that conduit resonance is more plausible case because locations of all five LP clusters are below active volcanic vent. Moreover, we think that conduit resonance model is viable exactly because it requires pressure trigger at top of the pipe – this again correspond to the shallow depth of observed LPs. The core idea of our interpretation is in the proposed nature of the trigger that causes whole magmatic conduit to resonate. Essentially, we factor forced bubble coalescence model with the support of the laboratory experiments into the simple yet sufficient conduit resonance model that requires that sort of trigger at the top of resonating pipe.

Such interpretation (*Figure 6.3*) proposes a driving mechanism itself – magma degassing, while simultaneously explaining LP seismicity specific features as a resonance process that follows each bubble coalescence. The high-energy earthquakes in catalog therefore correspond to large gas pockets able to produce strong initial shock, while numerous weak detections depicting smaller bubbles that

trigger the same resonance system but with a very subtle amplitude. In this interpretation temporal clustering may be viewed as an evolution of the magmatic conduit losing gasses trapped inside. The smooth transitions between clusters in extended catalog suggest that parameters of this LP-generating system may change gradually. While in the beginning the whole column was rich with gas phase, with time it probably slightly altered its geometry or wave velocities due to the fact that emitting gas was not replenished instantly. Thus, after 4 months of active degassing Gorely likely lost main portion of the gases in that current magma column and activity had stopped.

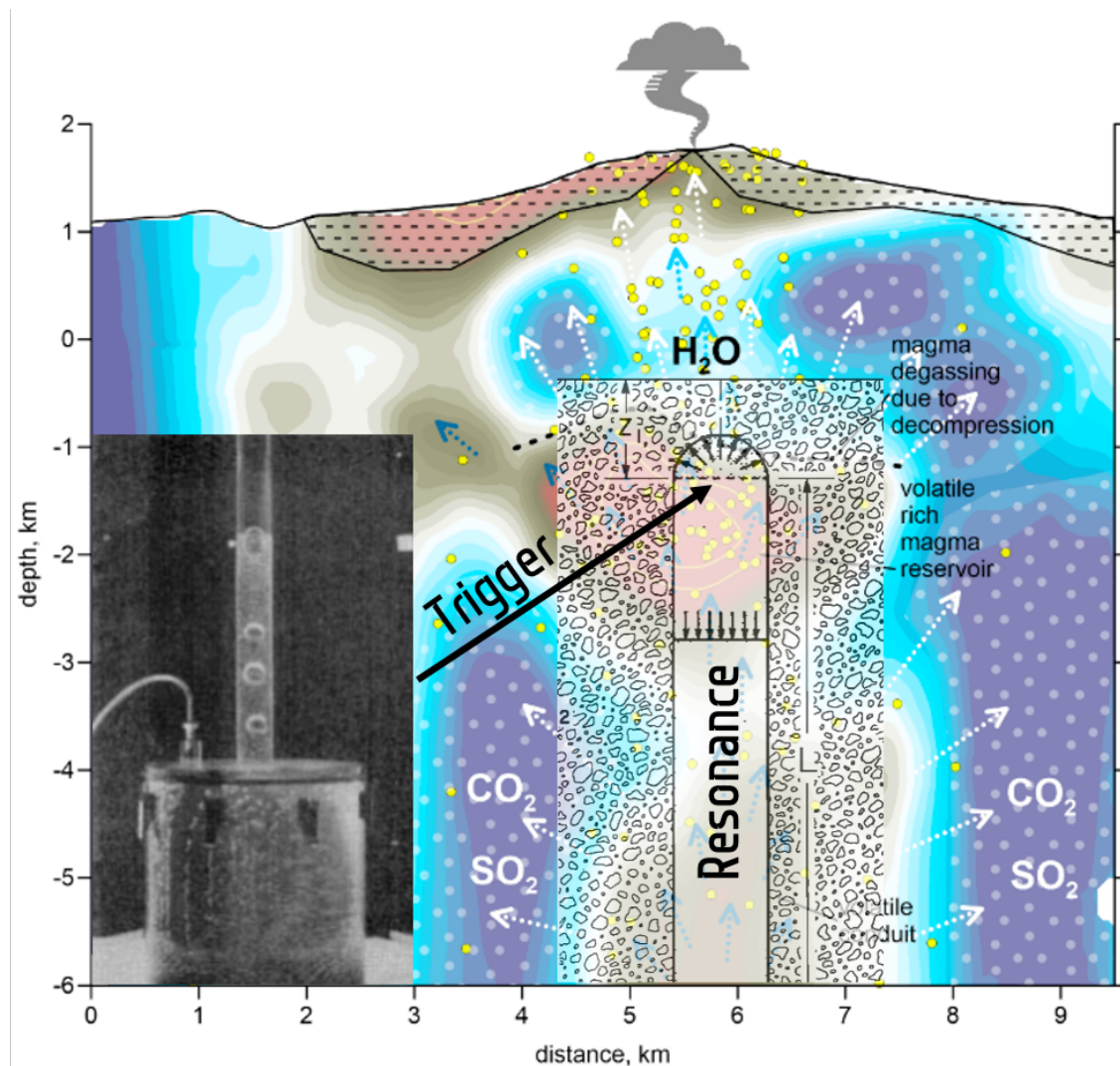


Figure 6.3 – Suggested interpretation of Gorely degassing episode based on the model of conduit resonance triggered by intermittent gas bubble coalescence. Background – tomography interpretation made by (Kuznetsov et al., 2017). Left – example of laboratory modelling done by (Jaupart & Vergnolle, 1988). Center transparent – cylindrical conduit resonance model suggested by (Chouet, 1985).

Conclusions

*A modest finished work is valued higher
than a remarkable incomplete one*

A robust catalogue of specific-type earthquakes is something highly desirable in seismology because it can give a valuable insight to the underlying mechanism of an originating phenomenon and its evolution in time. In case of long-period seismicity, one may expect a large number of events to be identified in swarms. Along with the massive size of continuous seismic records it urges a researcher to develop an automated approach for compiling and analyzing the catalogue of long-period earthquakes (LPs). Thus, the primary objective of this thesis was set as **develop an approach to successively built, investigate, verify, and enhance a catalogue of the long-period earthquakes**. To build the first catalogue with the most energetic events, an automatic detection algorithm based on back-projection technique was implemented. The acquired catalogue was investigated via cluster analysis that yield a set of templates for families of LPs and also served as a verification tool. Finally, applying a template-matching technique to continuously search for waveforms similar to those of constructed templates, which allow to compile the complementary extended catalogue of low-energy events. This catalogue, however, should be treated as a supplementary one in the analysis, because it could be noise contaminated and manual checking of more than 80 thousand detections seem practically impossible.

The developed algorithm was applied to study seismicity beneath the Gorely volcano, where the temporal seismic network of 20 stations was operating during the period of one year in 2013 – 2014. As a result, two complementary catalogues of repetitive LP earthquakes were obtained with 1737 high-energy events and 80,615 low-energy events, respectively. Cluster analysis revealed that the entire variety of LPs in these catalogues could be regrouped into five families, which are sequentially organized in time. The long-term occurrence of highly repetitive LPs in the same location may correspond to resonating conduits behaving in response to the high-pressure gases flowing from the decompressed magma chamber up to the volcano's crater.

Bibliography

- Abramnikov, S., Shapiro, N. M., Koulakov, I., & Abkadyrov, I. (2020). Clustering of Long-Period Earthquakes Beneath Gorely Volcano (Kamchatka) during a Degassing Episode in 2013. *Geosciences*, 10(6), 230. <https://doi.org/10.3390/geosciences10060230>
- Aiuppa, A., Giudice, G., Liuzzo, M., Tamburello, G., Allard, P., Calabrese, S., et al. (2012). First volatile inventory for Gorely volcano, Kamchatka. *Geophysical Research Letters*, 39(6), n/a-n/a. <https://doi.org/10.1029/2012GL051177>
- Aki, K., & Koyanagi, R. (1981). Deep volcanic tremor and magma ascent mechanism under Kilauea, Hawaii. *Journal of Geophysical Research*, 86(B8), 7095. <https://doi.org/10.1029/JB086iB08p07095>
- Aki, K., & Lee, W. H. K. (2003). Appendix 1 glossary of interest to earthquake and engineering seismologists (Vol. 81, pp. 1793–1856). [https://doi.org/10.1016/S0074-6142\(03\)80303-0](https://doi.org/10.1016/S0074-6142(03)80303-0)
- Aki, K., & Richards, P. G. (1980). *Quantitative Seismology: Theory and Methods*. W. H. Freeman. Retrieved from <https://books.google.ru/books?id=iYEWQQAACAAJ>
- Aki, K., Fehler, M., & Das, S. (1977). Source mechanism of volcanic tremor: fluid-driven crack models and their application to the 1963 kilauea eruption. *Journal of Volcanology and Geothermal Research*, 2(3), 259–287. [https://doi.org/10.1016/0377-0273\(77\)90003-8](https://doi.org/10.1016/0377-0273(77)90003-8)
- Allen, R. (1978). Automatic earthquake recognition and timing from single traces. *Bulletin of the Seismological Society of America*, 68(5), 1521–1532.
- Allen, R. (1982). Automatic phase pickers: Their present use and future prospects. *Bulletin of the Seismological Society of America*, 72(6B), S225–S242.
- Allstadt, K. E., Matoza, R. S., Lockhart, A. B., Moran, S. C., Caplan-Auerbach, J., Haney, M. M., et al. (2018). Seismic and acoustic signatures of surficial mass movements at volcanoes. *Journal of Volcanology and Geothermal Research*, 364, 76–106. <https://doi.org/10.1016/j.jvolgeores.2018.09.007>
- Apel, E. V., Bürgmann, R., Steblov, G. M., Vasilenko, N., King, R., & Prytkov, A. (2006). Independent active microplate tectonics of northeast Asia from GPS velocities and block modeling. *Geophysical Research Letters*, 33(11), L11303. <https://doi.org/10.1029/2006GL026077>
- Arámbula-Mendoza, R., Valdés-González, C., Varley, N., Reyes-Pimentel, T. A., & Juárez-García, B. (2016). Tremor and its duration-amplitude distribution at Popocatepetl volcano, Mexico. *Geophysical Research Letters*, 43(17), 8994–9001. <https://doi.org/10.1002/2016GL070227>
- Avdeiko, G. P., Savelyev, D. P., Palueva, A. A., & Popruzhenko, S. V. (2007). Evolution of the Kurile-Kamchatkan volcanic arcs and dynamics of the Kamchatka-Aleutian junction. *Geophysical Monograph Series*, 172, 37–55. <https://doi.org/10.1029/172GM04>
- Bartosch, T., & Seidl, D. (1999). Spectrogram analysis of selected tremor signals using short-time Fourier transform and continuous wavelet transform. *Annali Di Geofisica*. <https://doi.org/10.4401/ag-3733>
- Battaglia, M., Troise, C., Obrizzo, F., Pingue, F., & De Natale, G. (2006). Evidence for fluid migration as the source of deformation at Campi Flegrei caldera (Italy). *Geophysical Research Letters*, 33(1), n/a-n/a. <https://doi.org/10.1029/2005GL024904>
- Ben-Menahem, A. (1995). A concise history of mainstream seismology: origins, legacy, and perspectives. *Bulletin - Seismological Society of America*, 85(4), 1202–1225. [https://doi.org/10.1016/0148-9062\(96\)81706-2](https://doi.org/10.1016/0148-9062(96)81706-2)
- Bevis, J., & Royal Academy, O. B. (1757). *The History and Philosophy of Earthquakes, from the remotest to the present times: collected from the best writers on the subject. With a particular account of The Phenomena of the great one of November the 1st 1755, in various parts of the Globe.* (J. Bevis, Ed.). London: J. Nourse. Retrieved from <https://wellcomecollection.org/works/cucwuugz>
- Bindeman, I. N., Leonov, V. L., Izbekov, P. E., Ponomareva, V. V., Watts, K. E., Shipley, N. K., et al. (2010). Large-volume silicic volcanism in Kamchatka: Ar–Ar and U–Pb ages, isotopic, and geochemical characteristics of major pre-Holocene caldera-forming eruptions. *Journal of Volcanology and Geothermal Research*, 189(1–2), 57–80. <https://doi.org/10.1016/j.jvolgeores.2009.10.009>
- Bostock, M. G., Royer, A. A., Hearn, E. H., & Peacock, S. M. (2012). Low frequency earthquakes below southern Vancouver Island. *Geochemistry, Geophysics, Geosystems*, 13(11), 2012GC004391. <https://doi.org/10.1029/2012GC004391>
- Bowman, D. C., & Lees, J. M. (2013). The Hilbert-Huang Transform: A High Resolution Spectral Method for Nonlinear and Nonstationary Time Series. *Seismological Research Letters*, 84(6), 1074–1080. <https://doi.org/10.1785/0220130025>
- Brantley, S. R. (1990). *The eruption of Redoubt Volcano, Alaska, December 14, 1989-August 31, 1990. Circular.*

<https://doi.org/10.3133/cir1061>

- Caplan-Auerbach, J., & McNutt, S. R. (2003). New insights into the 1999 eruption of Shishaldin volcano, Alaska, based on acoustic data. *Bulletin of Volcanology*, 65(6), 405–417. <https://doi.org/10.1007/s00445-002-0267-5>
- Chakraborty, A., & Okaya, D. (1995). Frequency-time decomposition of seismic data using wavelet-based methods. *GEOPHYSICS*, 60(6), 1906–1916. <https://doi.org/10.1190/1.1443922>
- Chebrov, V. N., Droznin, D. V., Kugaenko, Y. A., Levina, V. I., Senyukov, S. L., Sergeev, V. A., et al. (2013). The system of detailed seismological observations in Kamchatka in 2011. *Journal of Volcanology and Seismology*, 7(1), 16–36. <https://doi.org/10.1134/S0742046313010028>
- Chouet, B. A. (1985). Excitation of a buried magmatic pipe: A seismic source model for volcanic tremor. *Journal of Geophysical Research*, 90(B2), 1881. <https://doi.org/10.1029/JB090iB02p01881>
- Chouet, B. A. (1986). Dynamics of a fluid-driven crack in three dimensions by the finite difference method. *Journal of Geophysical Research*, 91(B14), 13967. <https://doi.org/10.1029/JB091iB14p13967>
- Chouet, B. A. (1988). Resonance of a fluid-driven crack: Radiation properties and implications for the source of long-period events and harmonic tremor. *Journal of Geophysical Research: Solid Earth*, 93(B5), 4375–4400. <https://doi.org/10.1029/JB093iB05p04375>
- Chouet, B. A. (1996). Long-period volcano seismicity: its source and use in eruption forecasting. *Nature*, 380(6572), 309–316. <https://doi.org/10.1038/380309a0>
- Chouet, B. A. (2003). Volcano seismology. *Pure and Applied Physics*, 160, 739–788.
- Chouet, B. A., & Matoza, R. S. (2013). A multi-decadal view of seismic methods for detecting precursors of magma movement and eruption. *Journal of Volcanology and Geothermal Research*, 252, 108–175. <https://doi.org/10.1016/j.jvolgeores.2012.11.013>
- Chouet, B. A., Page, R. A., Stephens, C. D., Lahr, J. C., & Power, J. A. (1994). Precursory swarms of long-period events at Redoubt Volcano (1989–1990), Alaska: Their origin and use as a forecasting tool. *Journal of Volcanology and Geothermal Research*, 62(1–4), 95–135. [https://doi.org/10.1016/0377-0273\(94\)90030-2](https://doi.org/10.1016/0377-0273(94)90030-2)
- Chouet, B. A., Saccorotti, G., Martini, M., Dawson, P., De Luca, G., Milana, G., & Scarpa, R. (1997). Source and path effects in the wave fields of tremor and explosions at Stromboli Volcano, Italy. *Journal of Geophysical Research: Solid Earth*, 102(B7), 15129–15150. <https://doi.org/10.1029/97JB00953>
- Condie, K. C. (1997). *Plate Tectonics and Crustal Evolution*. Elsevier. <https://doi.org/10.1016/B978-0-7506-3386-4.X5000-9>
- Cooley, J. W., & Tukey, J. W. (1965). An algorithm for the machine calculation of complex Fourier series. *Mathematics of Computation*, 19(90), 297–297. <https://doi.org/10.1090/S0025-5718-1965-0178586-1>
- Crosson, R. S., & Bame, D. A. (1985). A spherical source model for low frequency volcanic earthquakes. *Journal of Geophysical Research*, 90(B12), 10237. <https://doi.org/10.1029/JB090iB12p10237>
- Cruz, Gil, F., Gil-Cruz, F., & Gil-Cruz, F. (1999). Observations of two special kinds of tremor at Galeras volcano, Colombia (1989 – 1991). *Annals of Geophysics*, 42(3), 437–449. <https://doi.org/10.4401/ag-3727>
- Daubechies, I. (1992). *Ten Lectures on Wavelets*. *The Mathematical Gazette* (Vol. 79). Society for Industrial and Applied Mathematics. <https://doi.org/10.1137/1.9781611970104>
- Dewey, J., & Byerly, P. (1969). The early history of seismometry (to 1900). *Bulletin of the Seismological Society of America*, 59(1), 183–227.
- Drew, J., White, R. S., Tilmann, F., & Tarasewicz, J. (2013). Coalescence microseismic mapping. *Geophysical Journal International*, 195(3), 1773–1785. <https://doi.org/10.1093/gji/ggt331>
- Duggen, S., Portnyagin, M., Baker, J., Ulfsbeck, D., Hoernle, K., Garbe-Schönberg, D., & Grassineau, N. (2007). Drastic shift in lava geochemistry in the volcanic-front to rear-arc region of the Southern Kamchatkan subduction zone: Evidence for the transition from slab surface dehydration to sediment melting. *Geochimica et Cosmochimica Acta*, 71(2), 452–480. <https://doi.org/10.1016/j.gca.2006.09.018>
- Dziewonski, A. M., & Anderson, D. L. (1981). Preliminary reference Earth model. *Physics of the Earth and Planetary Interiors*, 25(4), 297–356. [https://doi.org/10.1016/0031-9201\(81\)90046-7](https://doi.org/10.1016/0031-9201(81)90046-7)
- Endo, E. T., & Murray, T. (1991). Real-time Seismic Amplitude Measurement (RSAM): a volcano monitoring and prediction tool. *Bulletin of Volcanology*, 53(7), 533–545. <https://doi.org/10.1007/BF00298154>
- Flinn, E. A. (1965). Signal analysis using rectilinearity and direction of particle motion. *Proceedings of the IEEE*, 53(12), 1874–1876. <https://doi.org/10.1109/PROC.1965.4462>
- Frank, W. B., & Shapiro, N. M. (2014). Automatic detection of low-frequency earthquakes (LFEs) based on a beamformed network response. *Geophysical Journal International*, 197(2), 1215–1223. <https://doi.org/10.1093/gji/ggu058>
- Frank, W. B., Shapiro, N. M., Kostoglodov, V., Husker, A. L., Campillo, M., Payero, J. S., & Prieto, G. A. (2013). Low-frequency earthquakes in the Mexican Sweet Spot. *Geophysical Research Letters*, 40(11), 2661–2666.

<https://doi.org/10.1002/grl.50561>

- Frank, W. B., Shapiro, N. M., Husker, A. L., Kostoglodov, V., Romanenko, A., & Campillo, M. (2014). Using systematically characterized low-frequency earthquakes as a fault probe in Guerrero, Mexico. *Journal of Geophysical Research: Solid Earth*, 119(10), 7686–7700. <https://doi.org/10.1002/2014JB011457>
- Gavrilenko, M. G., Ozerov, A. Y., Kyle, P. R., Carr, M. J., Nikulin, A., Vidito, C., & Danyushevsky, L. (2016). Abrupt transition from fractional crystallization to magma mixing at Gorely volcano (Kamchatka) after caldera collapse. *Bulletin of Volcanology*, 78(7), 47. <https://doi.org/10.1007/s00445-016-1038-z>
- Gentili, S., & Michelini, A. (2006). Automatic picking of P and S phases using a neural tree. *Journal of Seismology*, 10(1), 39–63. <https://doi.org/10.1007/s10950-006-2296-6>
- Gibbons, S. J., & Ringdal, F. (2006). The detection of low magnitude seismic events using array-based waveform correlation. *Geophysical Journal International*, 165(1), 149–166. <https://doi.org/10.1111/j.1365-246X.2006.02865.x>
- Goldstein, P., & Chouet, B. A. (1994). Array measurements and modeling of sources of shallow volcanic tremor at Kilauea Volcano, Hawaii. *Journal of Geophysical Research: Solid Earth*, 99(B2), 2637–2652. <https://doi.org/10.1029/93JB02639>
- Gorbatov, A., Kostoglodov, V., Suárez, G., & Gordeev, E. (1997). Seismicity and structure of the Kamchatka Subduction Zone. *Journal of Geophysical Research: Solid Earth*, 102(B8), 17883–17898. <https://doi.org/10.1029/96JB03491>
- Goupillaud, P., Grossmann, A., & Morlet, J. (1984). Cycle-octave and related transforms in seismic signal analysis. *Geophysical Research Letters*, 11(1), 85–102. <https://doi.org/10.1029/1983GL01888>
- Grigoli, F., Cesca, S., Vassallo, M., & Dahm, T. (2013). Automated Seismic Event Location by Travel-Time Stacking: An Application to Mining Induced Seismicity. *Seismological Research Letters*, 84(4), 666–677. <https://doi.org/10.1785/0220120191>
- Grossmann, A., & Morlet, J. (1984). Decomposition of Hardy Functions into Square Integrable Wavelets of Constant Shape. *SIAM Journal on Mathematical Analysis*, 15(4), 723–736. <https://doi.org/10.1137/0515056>
- Grotzinger, J. P. (2007). *Understanding Earth*. Earth. W.H. Freeman. Retrieved from <https://books.google.ru/books?id=NYi0QgAACAAJ>
- Hardin, C. L. (1966). The scientific work of the reverend John Michell. *Annals of Science*, 22(1), 27–47. <https://doi.org/10.1080/00033796600203015>
- Harrington, R. M., & Brodsky, E. E. (2007). Volcanic hybrid earthquakes that are brittle-failure events. *Geophysical Research Letters*, 34(6), L06308. <https://doi.org/10.1029/2006GL028714>
- Havens, S., Marshall, H.-P., Johnson, J. B., & Nicholson, B. (2014). Calculating the velocity of a fast-moving snow avalanche using an infrasound array. *Geophysical Research Letters*, 41(17), 6191–6198. <https://doi.org/10.1002/2014GL061254>
- Hibert, C., Mangeney, A., Grandjean, G., & Shapiro, N. M. (2011). Slope instabilities in Dolomieu crater, Réunion Island: From seismic signals to rockfall characteristics. *Journal of Geophysical Research: Earth Surface*, 116(4). <https://doi.org/10.1029/2011JF002038>
- Hidayat, D., Voight, B., Langston, C., Ratdomopurbo, A., & Ebeling, C. (2000). Broadband seismic experiment at Merapi Volcano, Java, Indonesia: very-long-period pulses embedded in multiphase earthquakes. *Journal of Volcanology and Geothermal Research*, 100(1–4), 215–231. [https://doi.org/10.1016/S0377-0273\(00\)00138-4](https://doi.org/10.1016/S0377-0273(00)00138-4)
- Hill, D. P. (1977). A model for earthquake swarms. *Journal of Geophysical Research*, 82(8), 1347–1352. <https://doi.org/10.1029/JB082i008p01347>
- Iverson, R. M., Dzurisin, D., Gardner, C. A., Gerlach, T. M., LaHusen, R. G., Lisowski, M., et al. (2006). Dynamics of seismogenic volcanic extrusion at Mount St Helens in 2004–05. *Nature*, 444(7118), 439–443. <https://doi.org/10.1038/nature05322>
- Jaupart, C., & Vergnolle, S. (1988). Laboratory models of Hawaiian and Strombolian eruptions. *Nature*, 331(6151), 58–60. <https://doi.org/10.1038/331058a0>
- Jaxybulatov, K., Shapiro, N. M., Koulakov, I., Mordret, A., Landes, M., & Sens-Schonfelder, C. (2014). A large magmatic sill complex beneath the Toba caldera. *Science*, 346(6209), 617–619. <https://doi.org/10.1126/science.1258582>
- Jeong, W.-K., & Whitaker, R. T. (2008). A Fast Iterative Method for Eikonal Equations. *SIAM Journal on Scientific Computing*, 30(5), 2512–2534. <https://doi.org/10.1137/060670298>
- Jolly, A. D., Neuberg, J., Jousset, P., & Sherburn, S. (2012). A new source process for evolving repetitive earthquakes at Ngauruhoe volcano, New Zealand. *Journal of Volcanology and Geothermal Research*, 215–216, 26–39. <https://doi.org/10.1016/j.jvolgeores.2011.11.010>
- Julian, B. R. (1994). Volcanic tremor: Nonlinear excitation by fluid flow. *Journal of Geophysical Research: Solid Earth*, 99(B6), 11859–11877. <https://doi.org/10.1029/93JB03129>
- Kao, H., & Shan, S.-J. (2004). The Source-Scanning Algorithm: mapping the distribution of seismic sources in time and space. *Geophysical Journal International*, 157(2), 589–594. <https://doi.org/10.1111/j.1365-246X.2004.02276.x>

- Kao, H., & Shan, S.-J. (2007). Rapid identification of earthquake rupture plane using Source-Scanning Algorithm. *Geophysical Journal International*, 168(3), 1011–1020. <https://doi.org/10.1111/j.1365-246X.2006.03271.x>
- Kawakatsu, H., & Yamamoto, M. (2015). Volcano Seismology. In *Treatise on Geophysics* (Vol. 4, pp. 389–419). Elsevier. <https://doi.org/10.1016/B978-0-444-53802-4.00081-6>
- Kendrick, J. E., Lavallée, Y., Hirose, T., Di Toro, G., Hornby, A. J., De Angelis, S., & Dingwell, D. B. (2014). Volcanic drumbeat seismicity caused by stick-slip motion and magmatic frictional melting. *Nature Geoscience*, 7(6), 438–442. <https://doi.org/10.1038/ngeo2146>
- Kirchdörfer, M. (1999). Analysis and quasistatic FE modeling of long period impulsive events associated with explosions at Stromboli volcano (Italy). *Annals of Geophysics*, 42(3), 379–390. Retrieved from <http://hdl.handle.net/2122/1350>
- Kogan, M. G., Steblov, G. M., King, R. W., Herring, T. A., Frolov, D. I., Egorov, S. G., et al. (2000). Geodetic constraints on the rigidity and relative motion of Eurasia and North America. *Geophysical Research Letters*, 27(14), 2041–2044. <https://doi.org/10.1029/2000GL011422>
- Koulakov, I. (2009a). *Code LOTOS-10 for 3D tomographic inversion based on passive seismic data from local and regional events. User Manual*.
- Koulakov, I. (2009b). LOTOS Code for Local Earthquake Tomographic Inversion: Benchmarks for Testing Tomographic Algorithms. *Bulletin of the Seismological Society of America*, 99(1), 194–214. <https://doi.org/10.1785/0120080013>
- Koulakov, I., & Shapiro, N. (2021). Seismic Tomography of Volcanoes. In M. Beer, I. A. Kougioumtzoglou, E. Patelli, & I. S.-K. Au (Eds.), *Encyclopedia of Earthquake Engineering* (pp. 1–18). Berlin, Heidelberg: Springer Berlin Heidelberg. https://doi.org/10.1007/978-3-642-36197-5_51-1
- Koulakov, I. Y., Dobretsov, N. L., Bushenkova, N. A., & Yakovlev, A. V. (2011). Slab shape in subduction zones beneath the Kurile-Kamchatka and Aleutian arcs based on regional tomography results. *Russian Geology and Geophysics*, 52(6), 650–667. <https://doi.org/10.1016/j.rgg.2011.05.008>
- Kugaenko, Y. A., Nuzhdina, I. N., & Saltykov, V. A. (2011). Peculiarities of volcanic earthquakes spectral components for Kizimen, Koriaksky, Mutnovsky and Gorely volcanoes. *Vestnik KRAUNC*, 2(18).
- Kumagai, H., & Chouet, B. A. (1999). The complex frequencies of long-period seismic events as probes of fluid composition beneath volcanoes. *Geophysical Journal International*, 138(2), F7–F12. <https://doi.org/10.1046/j.1365-246X.1999.00911.x>
- Kumagai, H., & Chouet, B. A. (2000). Acoustic properties of a crack containing magmatic or hydrothermal fluids. *Journal of Geophysical Research: Solid Earth*, 105(B11), 25493–25512. <https://doi.org/10.1029/2000JB900273>
- Küperkoch, L., Meier, T., Lee, J., & Friederich, W. (2010). Automated determination of P-phase arrival times at regional and local distances using higher order statistics. *Geophysical Journal International*, 181(2), 1159–1170. <https://doi.org/10.1111/j.1365-246X.2010.04570.x>
- Küperkoch, Ludger, Meier, T., & Diehl, T. (2012). Automated Event and Phase Identification. In P. Bormann (Ed.), *New Manual of Seismological Observatory Practice 2 (NMSOP-2)* (Second, Vol. 1, pp. 1–52). Potsdam. https://doi.org/10.2312/GFZ.NMSOP-2_ch16
- Kuznetsov, P., Koulakov, I., Jakovlev, A., Abkadyrov, I., Deev, E., Gordeev, E. I., et al. (2017). Structure of Volatile Conduits beneath Gorely Volcano (Kamchatka) Revealed by Local Earthquake Tomography. *Geosciences*, 7(4), 111. <https://doi.org/10.3390/geosciences7040111>
- Lahr, J. C., Chouet, B. A., Stephens, C. D., Power, J. A., & Page, R. A. (1994). Earthquake classification, location, and error analysis in a volcanic environment: implications for the magmatic system of the 1989–1990 eruptions at Redoubt volcano, Alaska. *Journal of Volcanology and Geothermal Research*, 62(1–4), 137–151. [https://doi.org/10.1016/0377-0273\(94\)90031-0](https://doi.org/10.1016/0377-0273(94)90031-0)
- Langet, N., Maggi, A., Michelini, A., & Brenguier, F. (2014). Continuous Kurtosis-Based Migration for Seismic Event Detection and Location, with Application to Piton de la Fournaise Volcano, La Reunion. *Bulletin of the Seismological Society of America*, 104(1), 229–246. <https://doi.org/10.1785/0120130107>
- Lapins, S., Roman, D. C., Rougier, J., De Angelis, S., Cashman, K. V., & Kendall, J.-M. (2020). An examination of the continuous wavelet transform for volcano-seismic spectral analysis. *Journal of Volcanology and Geothermal Research*, 389, 106728. <https://doi.org/10.1016/j.jvolgeores.2019.106728>
- Lee, W. H. K. (1985). *HYP071PC : A Personal Computer Version of the HYP071 Earthquake Location*.
- Lees, J. M., & Ruiz, M. (2008). Non-linear explosion tremor at Sangay, Volcano, Ecuador. *Journal of Volcanology and Geothermal Research*, 176(1), 170–178. <https://doi.org/10.1016/j.jvolgeores.2007.08.012>
- Lesage, P., Mora, M. M., Alvarado, G. E., Pacheco, J., & Métaixian, J.-P. (2006). Complex behavior and source model of the tremor at Arenal volcano, Costa Rica. *Journal of Volcanology and Geothermal Research*, 157(1–3), 49–59. <https://doi.org/10.1016/j.jvolgeores.2006.03.047>
- Liao, Y.-C., Kao, H., Rosenberger, A., Hsu, S.-K., & Huang, B.-S. (2012). Delineating complex spatiotemporal distribution of earthquake aftershocks: an improved Source-Scanning Algorithm. *Geophysical Journal International*, 189(3), 1753–

1770. <https://doi.org/10.1111/j.1365-246X.2012.05457.x>
- Lomax, A., Virieux, J., Volant, P., & Berge-Thierry, C. (2000). Probabilistic Earthquake Location in 3D and Layered Models. In *Advances in Seismic Event Location. Modern Approches in Geophysics* (pp. 101–134). https://doi.org/10.1007/978-94-015-9536-0_5
- Mallet, R. (1848). On the Dynamics of Earthquakes. In *The Transactions of the Royal Irish Academy* (pp. 51–105). Academy. Retrieved from <https://archive.org/details/transactionsfro2liris/page/n63>
- Mallet, R., & Mallet, J. (1858). *The Earthquake Catalogue of the British Association: With the Discussion, Curves and Maps, Etc.* Taylor & Francis. Retrieved from https://books.google.ru/books?id=eId_nvF-i8EC
- Mangeney, A., Roche, O., Hungr, O., Mangold, N., Faccanoni, G., & Lucas, A. (2010). Erosion and mobility in granular collapse over sloping beds. *Journal of Geophysical Research*, 115(F3), F03040. <https://doi.org/10.1029/2009JF001462>
- Matoza, R. S., Chouet, B. A., Dawson, P. B., Shearer, P. M., Haney, M. M., Waite, G. P., et al. (2015). Source mechanism of small long-period events at Mount St. Helens in July 2005 using template matching, phase-weighted stacking, and full-waveform inversion. *Journal of Geophysical Research: Solid Earth*, 120(9), 6351–6364. <https://doi.org/10.1002/2015JB012279>
- McNutt, S. R. (1992). Volcanic Tremor. *Encyclopedia of Earth System Science*, 4, 417–425. Retrieved from <https://linkinghub.elsevier.com/retrieve/pii/B9780444636317000121>
- McNutt, S. R. (1996). Seismic Monitoring and Eruption Forecasting of Volcanoes: A Review of the State-of-the-Art and Case Histories. In *Monitoring and Mitigation of Volcano Hazards* (pp. 99–146). Berlin, Heidelberg: Springer Berlin Heidelberg. https://doi.org/10.1007/978-3-642-80087-0_3
- McNutt, S. R. (2005). Volcanic Seismology. *Annual Review of Earth and Planetary Sciences*, 33(1), 461–491. <https://doi.org/10.1146/annurev.earth.33.092203.122459>
- McNutt, S. R., & Nishimura, T. (2008). Volcanic tremor during eruptions: Temporal characteristics, scaling and constraints on conduit size and processes. *Journal of Volcanology and Geothermal Research*, 178(1), 10–18. <https://doi.org/10.1016/j.jvolgeores.2008.03.010>
- McNutt, S. R., & Roman, D. C. (2015). Volcanic Seismicity. In *The Encyclopedia of Volcanoes* (Second Edi, pp. 1011–1034). Elsevier. <https://doi.org/10.1016/B978-0-12-385938-9.00059-6>
- Melekescev, I. V., Braitseva, O. A., & Ponomareva, V. V. (1987). Activity dynamics of Mutnovsky and Gorely volcanos in Golocene and volcanic dangerous for surrounding regions. *Volcanology and Seismology*, 3, 3–18.
- Mertins, A. (1999). *Signal Analysis*. Chichester, UK: John Wiley & Sons, Ltd. <https://doi.org/10.1002/0470841834>
- Minakami, T. (1961). Study of eruptions and earthquakes originating from volcanoes (Part 1 of 3). *International Geology Review*, 3(8), 712–719. <https://doi.org/10.1080/00206816109473633>
- Minakami, T. (1974). Seismology of Volcanoes in Japan. In *Developments in Solid Earth Geophysics* (Vol. 6, pp. 1–27). Elsevier. <https://doi.org/10.1016/B978-0-444-41141-9.50007-3>
- Montalbetti, J. F., & Kanasevich, E. R. (1970). Enhancement of Teleseismic Body Phases with a Polarization Filter. *Geophysical Journal International*, 21(2), 119–129. <https://doi.org/10.1111/j.1365-246X.1970.tb01771.x>
- Morlet, J., Arens, G., Fourceau, E., & Glard, D. (1982). Wave propagation and sampling theory—Part I: Complex signal and scattering in multilayered media. *GEOPHYSICS*, 47(2), 203–221. <https://doi.org/10.1190/1.1441328>
- Morlet, J., Arens, G., Fourceau, E., & Giard, D. (1982). Wave propagation and sampling theory—Part II: Sampling theory and complex waves. *GEOPHYSICS*, 47(2), 222–236. <https://doi.org/10.1190/1.1441329>
- Moroz, Y. F., & Pospeev, A. V. (1995). Deep electrical conductivity of East Siberia and the Far East of Russia. *Tectonophysics*, 245(1–2), 85–92. [https://doi.org/10.1016/0040-1951\(94\)00143-W](https://doi.org/10.1016/0040-1951(94)00143-W)
- Nakamura, K. (1977). Volcanoes as possible indicators of tectonic stress orientation – principle and proposal. *Journal of Volcanology and Geothermal Research*, 2(1), 1–16. [https://doi.org/10.1016/0377-0273\(77\)90012-9](https://doi.org/10.1016/0377-0273(77)90012-9)
- Neuberg, J., & Pointer, T. (2000). Effects of volcano topography on seismic broad-band waveforms. *Geophysical Journal International*, 143(1), 239–248. <https://doi.org/10.1046/j.1365-246x.2000.00251.x>
- Newhall, C. G., & Self, S. (1982). The volcanic explosivity index (VEI) an estimate of explosive magnitude for historical volcanism. *Journal of Geophysical Research*, 87(C2), 1231. <https://doi.org/10.1029/JC087iC02p01231>
- Obara, K. (2002). Nonvolcanic Deep Tremor Associated with Subduction in Southwest Japan. *Science*, 296(5573), 1679–1681. <https://doi.org/10.1126/science.1070378>
- Omori, F. (1912). The eruption and earthquakes of the Asama-yama. *Bull. Imp. Earthquake Inv. Com.*, 6, 1–147.
- Park, I., Jolly, A., Kim, K. Y., & Kennedy, B. (2019). Temporal variations of repeating low frequency volcanic earthquakes at Ngauruhoe Volcano, New Zealand. *Journal of Volcanology and Geothermal Research*, 373, 108–119. <https://doi.org/10.1016/j.jvolgeores.2019.01.024>
- Petersen, T. (2007). Swarms of repeating long-period earthquakes at Shishaldin Volcano, Alaska, 2001–2004. *Journal of*

- Volcanology and Geothermal Research*, 166(3–4), 177–192. <https://doi.org/10.1016/j.jvolgeores.2007.07.014>
- Petersen, T., Caplan-Auerbach, J., & McNutt, S. R. (2006). Sustained long-period seismicity at Shishaldin Volcano, Alaska. *Journal of Volcanology and Geothermal Research*, 151(4), 365–381. <https://doi.org/10.1016/j.jvolgeores.2005.09.003>
- Poiata, N., Satriano, C., Vilotte, J.-P., Bernard, P., & Obara, K. (2016). Multiband array detection and location of seismic sources recorded by dense seismic networks. *Geophysical Journal International*, 205(3), 1548–1573. <https://doi.org/10.1093/gji/ggw071>
- Portnyagin, M., Hoernle, K., Avdeiko, G., Hauff, F., Werner, R., Bindeman, I., et al. (2005). Transition from arc to oceanic magmatism at the Kamchatka-Aleutian junction. *Geology*, 33(1), 25. <https://doi.org/10.1130/G20853.1>
- Power, J. A., Lahr, J. C., Page, R. A., Chouet, B. A., Stephens, C. D., Harlow, D. H., et al. (1994). Seismic evolution of the 1989–1990 eruption sequence of Redoubt Volcano, Alaska. *Journal of Volcanology and Geothermal Research*, 62(1–4), 69–94. [https://doi.org/10.1016/0377-0273\(94\)90029-9](https://doi.org/10.1016/0377-0273(94)90029-9)
- Qian, S., & Chen, D. (1996). *Joint Time-Frequency Analysis Qian.pdf*. PTR Prentice Hall. Retrieved from <http://sharif.edu/~mbshams/Joint Time-Frequency Analysis Qian.pdf>
- Ratdomopurbo, A., & Poupinet, G. (1995). Monitoring a temporal change of seismic velocity in a volcano: Application to the 1992 eruption of Mt. Merapi (Indonesia). *Geophysical Research Letters*, 22(7), 775–778. <https://doi.org/10.1029/95GL00302>
- Ripepe, M., & Gordeev, E. I. (1999). Gas bubble dynamics model for shallow volcanic tremor at Stromboli. *Journal of Geophysical Research: Solid Earth*, 104(B5), 10639–10654. <https://doi.org/10.1029/98JB02734>
- Rogers, J. A., & Stephens, C. D. (1995). SSAM: real-time seismic spectral amplitude measurement on a PC and its application to volcano monitoring. *Bulletin - Seismological Society of America*, 85(2), 632–639.
- Roman, D. C. (2005). Numerical models of volcanotectonic earthquake triggering on non-ideally oriented faults. *Geophysical Research Letters*, 32(2), L02304. <https://doi.org/10.1029/2004GL021549>
- Roman, D. C., & Cashman, K. V. (2006). The origin of volcano-tectonic earthquake swarms. *Geology*, 34(6), 457. <https://doi.org/10.1130/G22269.1>
- Roman, D. C., Moran, S. C., Power, J. A., & Cashman, K. V. (2004). Temporal and Spatial Variation of Local Stress Fields before and after the 1992 Eruptions of Crater Peak Vent, Mount Spurr Volcano, Alaska. *Bulletin of the Seismological Society of America*, 94(6), 2366–2379. <https://doi.org/10.1785/0120030259>
- Saragiotis, C. D., Hadjileontiadis, L. J., & Panas, S. M. (2002). PAI-S/K: A robust automatic seismic P phase arrival identification scheme. *IEEE Transactions on Geoscience and Remote Sensing*, 40(6), 1395–1404. <https://doi.org/10.1109/TGRS.2002.800438>
- Sassa, K. (1936). Volcanic Micro-Tremors and Eruption-Earthquakes (火山脈動及び爆發地震). Part 1 of the Geophysical Studies on the Volcano Aso. *Journal of the Meteorological Society of Japan. Ser. II*, 14(7), 376–377. https://doi.org/10.2151/jmsj1923.14.7_376
- Seligman, A., Bindeman, I., Jicha, B., Ellis, B., Ponomareva, V., & Leonov, V. (2014). Multi-Cyclic and Isotopically Diverse Silicic Magma Generation in an Arc Volcano: Gorely Eruptive Center, Kamchatka, Russia. *Journal of Petrology*, 55(8), 1561–1594. <https://doi.org/10.1093/petrology/egu034>
- Selyangin, O. B., & Ponomareva, V. V. (1999). Gorelovsky Volcanic Center, Southern Kamchatka: Structure and Evolution. *Journal of Volcanology and Seismology*, (2), 3–23.
- Shapiro, N. M., Droznin, D. V., Droznina, S. Y., Senyukov, S. L., Gusev, A. A., & Gordeev, E. I. (2017). Deep and shallow long-period volcanic seismicity linked by fluid-pressure transfer. *Nature Geoscience*, 10(6), 442–445. <https://doi.org/10.1038/ngeo2952>
- Shelly, D. R. (2009). Possible deep fault slip preceding the 2004 Parkfield earthquake, inferred from detailed observations of tectonic tremor. *Geophysical Research Letters*, 36(17), L17318. <https://doi.org/10.1029/2009GL039589>
- Shelly, D. R., Beroza, G. C., Ide, S., & Nakamura, S. (2006). Low-frequency earthquakes in Shikoku, Japan, and their relationship to episodic tremor and slip. *Nature*, 442(7099), 188–191. <https://doi.org/10.1038/nature04931>
- De Siena, L., Del Pezzo, E., & Bianco, F. (2010). Seismic attenuation imaging of Campi Flegrei: Evidence of gas reservoirs, hydrothermal basins, and feeding systems. *Journal of Geophysical Research*, 115(B9), B09312. <https://doi.org/10.1029/2009JB006938>
- Sobolevskaya, O. V. (2009). Seismicity of Gorely volcano 1984–2009. In *Regional Conference at KB GS RAS* (pp. 382–386). Petropavlovsk-Kamchatsky, Russia.
- Soubestre, J., Shapiro, N. M., Seydoux, L., de Rosny, J., Droznin, D. V., Droznina, S. Y., et al. (2018). Network-Based Detection and Classification of Seismovolcanic Tremors: Example From the Klyuchevskoy Volcanic Group in Kamchatka. *Journal of Geophysical Research: Solid Earth*, 123(1), 564–582. <https://doi.org/10.1002/2017JB014726>
- Suriñach, E., Sabot, F., Furdada, G., & Vilaplana, J. M. (2000). Study of seismic signals of artificially released snow avalanches for monitoring purposes. *Physics and Chemistry of the Earth, Part B: Hydrology, Oceans and Atmosphere*, 25(9), 721–

727. [https://doi.org/10.1016/S1464-1909\(00\)00092-7](https://doi.org/10.1016/S1464-1909(00)00092-7)
- Takei, Y. (2002). Effect of pore geometry on V P / V S : From equilibrium geometry to crack. *Journal of Geophysical Research*, 107(B2), 2043. <https://doi.org/10.1029/2001JB000522>
- Tary, J. B., Herrera, R. H., Han, J., & van der Baan, M. (2014). Spectral estimation-What is new? What is next? *Reviews of Geophysics*, 52(4), 723–749. <https://doi.org/10.1002/2014RG000461>
- Tchebotareva, I. I., Nikolaev, A. V., & Sato, H. (2000). Seismic emission activity of Earth's crust in Northern Kanto, Japan. *Physics of the Earth and Planetary Interiors*, 120(3), 167–182. [https://doi.org/10.1016/S0031-9201\(99\)00163-6](https://doi.org/10.1016/S0031-9201(99)00163-6)
- Timofeev, V. Y., Ardyukov, D. G., Solov'ev, V. M., Shibaev, S. V., Petrov, A. F., Gornov, P. Y., et al. (2012). Plate boundaries in the Far East region of Russia (from GPS measurement, seismic-prospecting, and seismological data). *Russian Geology and Geophysics*, 53(4), 376–391. <https://doi.org/10.1016/j.rgg.2012.03.002>
- Toda, S., Stein, R. S., & Sagiya, T. (2002). Evidence from the AD 2000 Izu islands earthquake swarm that stressing rate governs seismicity. *Nature*, 419(6902), 58–61. <https://doi.org/10.1038/nature00997>
- Tokarev, P. I. (1966). *Eruptions and Seismic Regime of Volcanoes of Klyuchevskaya Group*. Moscow (in Russian): Nauka.
- Tolstykh, M. L., Naumov, V. B., Gavrilenko, M. G., Ozerov, A. Y., & Kononkova, N. N. (2012). Chemical composition, volatile components, and trace elements in the melts of the Gorely volcanic center, southern Kamchatka: Evidence from inclusions in minerals. *Geochemistry International*, 50(6), 522–550. <https://doi.org/10.1134/S0016702912060079>
- Ukawa, M., & Tsukahara, H. (1996). Earthquake swarms and dike intrusions off the east coast of Izu Peninsula, central Japan. *Tectonophysics*, 253(3–4), 285–303. [https://doi.org/10.1016/0040-1951\(95\)00077-1](https://doi.org/10.1016/0040-1951(95)00077-1)
- Volynets, O. N., Patoka, M. G., Anoshin, G. N., & Ananiev, V. V. (1992). GEOCHEMISTRY OF LATE CENOZOIC BASALTS FROM EAST KAM- CHATKA AND IMPLICATIONS FOR GEODYNAMIC EVOLUTION OF MAGMA GENERATION, 12(5), 560–575.
- Waldhauser, F. (2000). A Double-Difference Earthquake Location Algorithm: Method and Application to the Northern Hayward Fault, California. *Bulletin of the Seismological Society of America*, 90(6), 1353–1368. <https://doi.org/10.1785/0120000006>
- Wassermann, J. (2012). Volcano Seismology. In P. Bormann (Ed.), *New Manual of Seismological Observatory Practice 2 (NMSOP-2)* (Second, pp. 1–77). Potsdam: Potsdam: Deutsches GeoForschungsZentrum GFZ. https://doi.org/10.2312/GFZ.NMSOP-2_ch13
- Westfall, P. H. (2014). Kurtosis as Peakedness, 1905–2014. R.I.P. *The American Statistician*, 68(3), 191–195. <https://doi.org/10.1080/00031305.2014.917055>
- Withers, M., Aster, R., Young, C., Beiriger, J., Harris, M., Moore, S., & Trujillo, J. (1998). A comparison of select trigger algorithms for automated global seismic phase and event detection. *Bulletin of the Seismological Society of America*, 88(1), 95–106.
- Yuan, K., & Romanowicz, B. (2017). Seismic evidence for partial melting at the root of major hot spot plumes. *Science*, 357(6349), 393–397. <https://doi.org/10.1126/science.aan0760>
- Zhao, J., Moretti, L., Mangeney, A., Stutzmann, E., Kanamori, H., Capdeville, Y., et al. (2015). Model space exploration for determining landslide source history from long-period seismic data. *Pure and Applied Geophysics*, 172(2), 389–413. <https://doi.org/10.1007/s00024-014-0852-5>
- Zobin, V. (2012). *Introduction to Volcanic Seismology*. *Introduction to Volcanic Seismology*. Elsevier. <https://doi.org/10.1016/C2011-0-06141-0>

Publications

2020:


Abramenkov, S., Shapiro, N. M., Koulakov, I., & Abkadyrov, I.

Clustering of Long-Period Earthquakes Beneath Gorely Volcano (Kamchatka) during a Degassing Episode in 2013.

Geosciences, 10 (6), 230. <https://doi.org/10.3390/geosciences10060230>

Article

Clustering of Long-Period Earthquakes Beneath Gorely Volcano (Kamchatka) during a Degassing Episode in 2013

Sergei Abramenkov ^{1,2,*}, Nikolai M. Shapiro ^{3,4}, Ivan Koulakov ^{2,5,6,*}  and Ilyas Abkadyrov ^{2,6}

¹ Institut de Physique du Globe de Paris, Université de Paris, CNRS UMR7154, 1 rue Jussieu, 75238 Paris, France

² Trofimuk Institute of Petroleum Geology and Geophysics SB RAS, Prospekt Koptyuga, 3, 630090 Novosibirsk, Russia; AbkadyrovIF@ipgg.sbras.ru

³ Institut des Sciences de la Terre (ISTERRE), UMR CNRS 5375, Université Grenoble-Alpes, 38058 Grenoble, France; nikolai.shapiro@univ-grenoble-alpes.fr

⁴ Schmidt Institute of Physics of the Earth, Russian Academy of Sciences, 119991 Moscow, Russia

⁵ Laboratory of Seismic Imaging of the Earth, Novosibirsk State University, Pirogova 2, 630090 Novosibirsk, Russia

⁶ Institute of Volcanology and Seismology FEB RAS, Piip Boulevard, 9, 693006 Petropavlovsk-Kamchatsky, Russia

* Correspondence: abram.science@gmail.com (S.A.); koulakoviy@ipgg.sbras.ru (I.K.); Tel.: +7-913-4538-987 (I.K.)

Received: 7 May 2020; Accepted: 12 June 2020; Published: 14 June 2020



Abstract: Gorely is one of the most active volcanoes in Kamchatka with a rich magmatic and eruptive history reflected in its composite structure. In 2013–2014, a temporary network of 20 seismic stations was installed on Gorely for one year. During the four months of its high degassing rate, seismic activity was mostly expressed in the form of a long-period (LP) seismic tremor. In this study, we have developed a workflow based on the combination of back-projection (BP), cluster analysis, and matched-filter (MF) methods. By applying it to continuous seismic records for the study period, we were able to identify discrete LP events within the tremor sequence automatically and individually investigate their properties. A catalog obtained using the BP detection algorithm consist of 1741 high-energy events. Cluster analysis revealed that the entire variety of LP earthquakes in this catalog could be grouped into five families, which are sequentially organized in time. Utilizing templates of these families in the MF search resulted in the complementary catalog of 80,615 low-energy events. The long-term occurrence of highly repetitive LP events in the same location may correspond to resonating conduits behaving in response to the high-pressure gases flowing from the decompressed magma chamber up to the volcano's crater.

Keywords: Gorely volcano; degassing; long-period seismicity; cluster analysis; back-projection; matched-filter

1. Introduction

Processes in active magma systems can set in motion different types of seismic sources occurring either through abrupt fractures of rocks, or oscillations of magma containing reservoirs, or as a combination of these two processes [1,2]. These sources generate seismic waves that can be recorded by seismic stations and used to monitor volcano activity and to diagnose the state of the magma plumbing system. Unlike purely tectonic earthquakes in non-volcanic areas, the volcano-related seismicity has a broad range of types starting from volcano-tectonic (VT) earthquakes with clear arrivals of the P

and S waves, to volcanic tremors, in which no distinct waves can be recognized [3]. If we factor the uniqueness of each volcanic region to such a specter of seismic signals produced even by a single volcano, one may see why the development of a unified classification is a genuine challenge for any seismologist.

This study is focused on long-period (LP) earthquakes. Among types of volcanic seismicity repeatedly described in the literature [2,4–6], these are troublemakers that make terminology confusing. Typically, LP events share a characteristic signature consisting of a brief high-frequency onset followed by decaying harmonic waveform that contains one or several dominant frequencies in the typical range of 0.5–5 Hz [7]. Such signal features are commonly interpreted as a broadband, time-localized pressure excitation mechanism (or trigger mechanism), followed by the response of a fluid-filled resonator [8]. In many cases, the LP volcanic earthquakes appear in swarms as a series of repetitive signals with almost identical waveform allowing to reconstruct the source geometry [9–16]. In Kamchatka, several clusters of deep and shallow repetitive LP events have been identified beneath the volcanoes of the Klyuchevskoy group that were activated synchronously with the occurrence of eruptions [17]. Studies of LP earthquakes precursory nature [18,19] have potentially immense importance for the public, especially in areas where volcanoes are located to close proximity of densely populated cities. An approach proposed in the present work allows us to detect individual LP events in continuous seismic records automatically. Furthermore, by using cluster analysis, we were able to reveal all possible variations of the LP seismicity occurred in the study region.

In the scope of this study, we investigate the LP earthquakes beneath the active Gorely Volcano in Kamchatka. Since 1984, the seismicity of Gorely is monitored by one permanent telemetered seismic station that was later supplemented with two other stations located on the neighboring Mutnovsky and Asacha volcanoes [20]. In 2013–2014, a temporary seismic network of 20 stations was installed on Gorely for one year. The analysis of data recorded by this network was used to obtain accurate locations of volcano-tectonic events beneath Gorely and to build a 3D seismic model [21]. A bright anomaly with a very high V_p/V_s ratio (up to 2) obtained in this study just below the summit of Gorely was interpreted as a shallow magma chamber. The upper limit of this anomaly at 2.6 km below the surface, followed beneath the topographic profile, might represent a level of the transition of fluids dissolved in the magma to gases due to decompression. This seismic velocity model also revealed a deeper anomaly of high V_p/V_s ratio located right below the shallow magma reservoir, which was interpreted as a conduit delivering the volatile-rich magma to the shallow reservoir from deeper sources. Both anomalies were surrounded by areas of low V_p/V_s ratio, with values reaching 1.4, which were interpreted as zones saturated with gases.

The primary purpose of this study is to further investigate the processes in the magmatic system beneath the Gorely volcano during the period of intense degassing activity in late 2013. In contrast to previously performed tomography study, here we use the continuous seismic records of the temporary network to study the distributions and properties of LP earthquakes beneath Gorely. Both the massive size of the dataset and the high expected occurrence-rate of these events urged us to develop the following three-step workflow: (1) identification of the most potent LP events by the back-projection detection technique, (2) cluster analysis of obtained catalog in order to group events with similar waveforms into several families, each represented by corresponding master event, (3) extension of the catalog to low-energy LP events by matched-filter detection technique using waveforms of the master events as a template. In the paper, we first give a concise overview of Gorely's geological context, followed by a brief description of available data. We describe each of the three steps mentioned above in the designated section and present the results of their implementation. Finally, we provide a possible interpretation of the resulting LP seismicity properties in terms of volcanic processes.

2. Gorely Volcano

Gorely is an active volcano located approximately 70 km away from Petropavlovsk-Kamchatsky, the most populated city on the Kamchatka Peninsula. Situated in the southern segment of Kamchatka's

Eastern Volcanic Front, 25 km from the Pacific coast, it is related to the ongoing subduction of the Pacific Plate, which is located at a depth of ~130 km below Gorely [22,23]. Morphologically Gorely is a compound shield-like stratovolcano with an altitude of ~1800 m above sea level and a relative elevation of ~850 m. Its upper part forms a linear northwest striking ridge of three merged primary cones and 11 superimposed summit craters complicated by more than 40 flank cones [24]. The modern Gorely edifice is located inside an ancient elliptic caldera with a size of 9×13 km, which is apparent on the topography map (Figure 1).

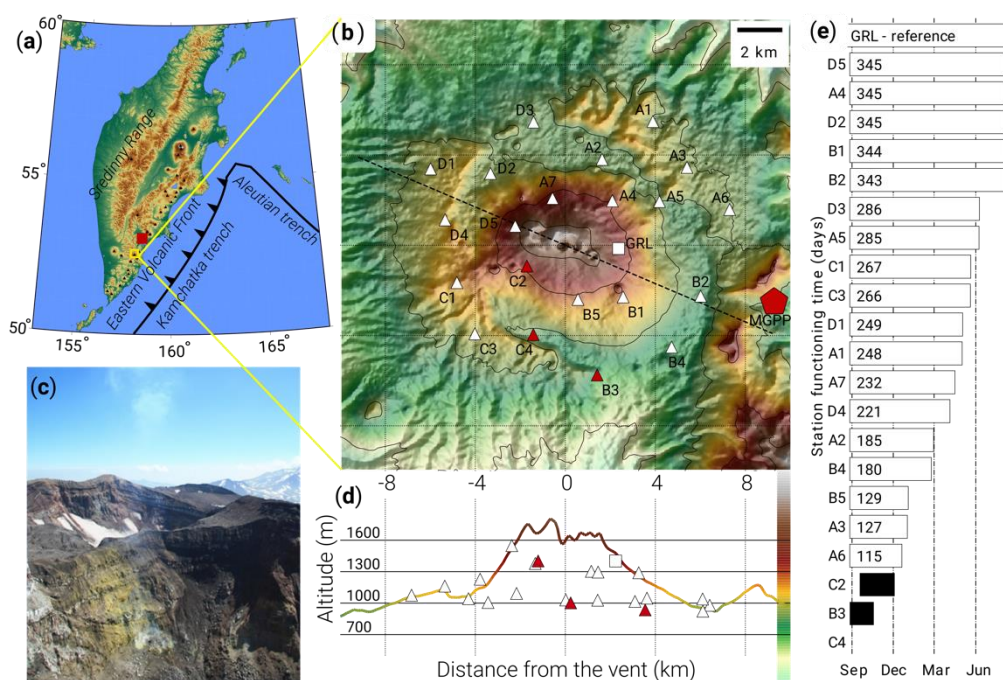


Figure 1. Gorely temporary seismic network (August 2013–August 2014) in the context of study region: (a) map of the Kamchatka peninsula with main tectonic features (red square indicates the city of Petropavlovsk-Kamchatsky, black triangles—active volcanoes and yellow square marks Gorely study region); (b) network geometry along with volcano topography (white triangles are stations used for analysis, white square—permanent GRL station, red triangles—nonfunctional stations, red pentagon—Mutnovsky Geothermal Power Plant); (c) photo of the volcanic vent taken during network installation process from the active crater edge; (d) projection of station locations on volcanic edifice along the dashed line; (e) data recovery chart sorted according to station functioning time.

The contemporary Gorely volcano represents the evolutionary development of an older volcanic center, followed by a radical transformation of its magma-feeding system [23]. Based on the age and composition of the erupted rocks, one can define three major stages of its formation [25,26]. The first (pre-caldera) stage is associated with the development of Pra-Gorely (also referred to as “Old Gorely”), which was an extensive (approximately 12×15 km in size) Middle-Pleistocene shield volcano stretched in the northeastern direction. Nowadays, the remnants of Pra-Gorely are mainly represented by peripheral parts of massive lava flows at the edges of the caldera and some relicts in the surrounding plateau [25]. The second stage led to the formation of a large caldera and massive felsic pyroclastic deposits in the surrounding area of 600 km^2 . There is debate about whether this thick ignimbrite and pumice complex with the total volume $>100 \text{ km}^3$ has been deposited during a single [25] or multiple caldera-forming eruptions ranging in age from 361 ka to 38 ka [27,28]. Regardless of the eruptions number, such depletion of a large magma chamber embedded in the Earth’s crust below Pra-Gorely caused its roof to collapse. Limited by steeply dipping arc faults, the Gorely volcano caldera is a typical collapse structure of the Krakatau type that is confirmed by magmatic permeability of individual sections in the caldera boundary [25]. The last (post-caldera) major stage started toward the end of Late

Pleistocene with monogenetic volcanism on the weakened zone of the caldera rim. It was continued by the formation and development of the modern edifice in the central part of the caldera [26]. During Holocene Gorely's activity mainly consists of a cyclic alternation between phases Vulcanian-style explosive eruptions, voluminous ($>0.1 \text{ km}^3$) lava flow eruptions, and intense degassing [25].

Having relatively high explosive eruption potential [29], Gorely may represent a significant hazard for aviation [30], tourists, and nearby infrastructures such as Mutnovsky Geothermal Power Plant (MGPP on Figure 1b) with a capacity of 50 MWt which provides a significant part of the electrical energy to the Petropavlovsk-Kamchatsky city and its surroundings. Therefore, the volcano has been thoroughly investigated by specialists in different disciplines of geosciences. The first robust data on the geological structure and development of Gorely volcano were published in [31,32], with the descriptions of the caldera, the associated pumice-ignimbrite deposits, the structural and material composition of the pre-caldera complex and the modern edifice. The comprehensive reconstruction of its Holocene activity via tephrochronological analysis was presented in [33]. In 1974–1977 a geological survey on a scale of 1:50,000 had resulted in a detailed geological map of the Gorely volcano [25]. In 20th century all eruptions (1921–1931; 1959–1960; 1980–1981; 1984–1986) were moderately explosive ($\text{VEI} < 3$) and occurred through the central summit with emission of basaltic-andesitic ash [24]. After the most recent one in 1986, a large fumarole was formed in the crater, through which an active emission of gases ensued. In the period of strongest degassing activity in 2010, the mass of gases emitted through this fumarole was estimated at 11,000 tons per day, with the outlet temperature reaching 900°C . It is determined that these gases were composed of water (93.5%), CO_2 (2.6%), SO_2 (2.2%), HCl (1.1%), HF (0.3%), H_2 (0.2%), as well as some bromine and iodine compounds. It was estimated that under this regime, Gorely emitted about 0.3% and 1.6% of the total global fluxes from arc volcanism for CO_2 and HCl , respectively [34].

3. Seismic Data

In 1980, the Kamchatka Branch of the Geophysical Survey (KBGS) installed one telemetric seismic station GRL on the eastern slope of Gorely volcano. Two more permanent stations were installed in the summer of 2008 on the neighboring Mutnovsky and Asacha volcanoes. All stations were equipped with three-component sets of short-period channels based on SM-3 seismometers for recording the ground displacement velocity in the frequency band of 0.8–20 Hz. These permanent stations were used to investigate the seismicity beneath Gorely since 1984 [20,35]. Note, however, that these studies could only provide count and energy estimates for the events, but not the information about their locations.

A dense temporal seismic network (Figure 1) consisting of 20 three-component broadband seismographs was deployed on the Gorely volcanic edifice and its surroundings in August 2013 by joint efforts of scientists from Trofimuk Institute of Petroleum Geology and Geophysics SB RAS (initiated this project), Department of Geology and Geophysics of Novosibirsk State University (provided seismic instruments) and Institute of Volcanology and Seismology FEB RAS (provided logistical support of the fieldwork). The network was removed in August 2014 and provided ~350 Gb of continuous seismic records in total. Each of the temporal stations consisted of a CME-4311 (R-sensors, Moscow, Russia) three-component broadband sensor and a digital recorded Baikal-ACN-87/88 (R-sensors, Novosibirsk, Russia) with power supply provided by one box of 10 high-capacity power batteries Baken VTs-1 (UralElement, Verchniy Ufaley, Russia), external GPS antenna and necessary ventilated protection against dust and moisture. Baikal-ACN series recorders are three-channel autonomous seismic stations of an extended frequency range with an internal or external GPS module, a USB 2.0 channel for communication with a laptop, and a memory slot for SD card supporting volumes up to 32 GB. The CME-4311 three-component broadband velocimeter is built of three orthogonally oriented molecular-electronic transducer, and an electronic board, placed in a protective outer casing. The manufacturer stated flat instrument response in the frequency band of 0.016 (60 s) to 50 Hz.

We use the seismic records from a single permanent station GRL located on the volcanic edifice and maintained by the Kamchatka Branch of the Geophysical Survey as a reference. Even though

ground waters eventually flooded some stations of the temporal array, overall data coverage remained consistent enough for more than eight months with maximal spatial density during the four starting months. It allows us to analyze the seismicity on Gorely during a significant period containing an episode of volcano's intense degassing. In this study, we consider the period from the 28th August till the 17th December, when the maximum seismic volcano-related activity occurred beneath Gorely. During this period, 18 stations of the temporary network were functioning, providing dense observation system on the volcano.

Preliminary analysis revealed that the dominant part of seismic energy was emitted by numerous LP earthquakes, which occurred on average twice per minute during most active phases of the degassing episode. Corresponding signals have a duration of about 10–15 s long, with an energy peak at 3 Hz. The strong similarity of these waveforms for consecutive events is the most notable feature of the dataset. Figure 2a presents an example of a five-minute seismogram of vertical components recorded by all available stations that clearly shows the LP swarm beneath Gorely. In this interval, at least eight events can be visually identified, and all of them have almost identical waveforms, as seen in an example in Figure 2b,c.

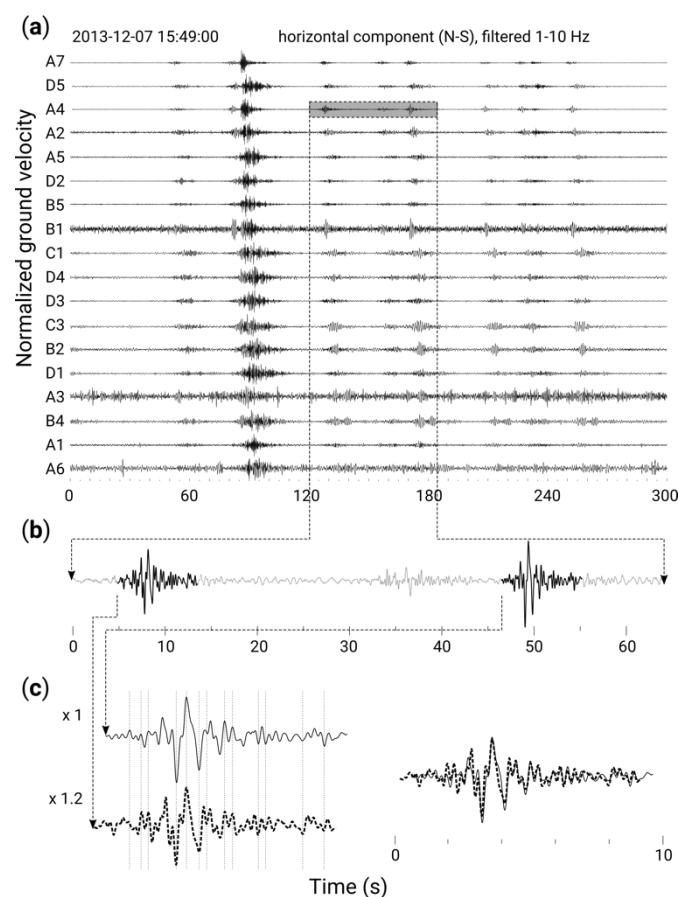


Figure 2. Example of LP swarm on Gorely: (a) 5-minute horizontal component records of 18 temporary stations; (b) zoom on representative LP signals at station A4; (c) close comparison of two waveforms.

A large number of events to be identified with a massive amount of the continuous seismic records urged us to develop a particular automated approach for compiling and analyzing the LP earthquakes. A robust catalog of specific type earthquakes is something highly desirable in seismology because it can give us valuable insights about the underlying mechanism and its evolution in time. We were trying to construct one by using three methods that successively built, investigate, verify, and enhance a catalog of the LP earthquakes. To build the first catalog with the most energetic events, we used

an automatic detection algorithm based on back-projection (BP) technique. We then investigated the acquired catalog via cluster analysis that gave us a set of templates for several LPs clusters and served as a verification tool. Finally, applying a matched-filter (MF) technique, we searched for less-energetic events with waveforms similar to the obtained templates, thus compiling the complementary extended catalog of low-energy LP events. This catalog, however, should be used as a supplementary one in the analysis since it could be noise-contaminated.

4. Back-Projection Detection and Location Algorithm

The back-projection (BP) method is a practical approach to detect and locate seismicity by taking advantages of a seismic network or array. The core idea of this method is a stacking of seismic records shifted by precomputed travel times to the theoretical origin points followed by a grid-search for the local maximum in space and time. Several shift-and-stack methodologies have been described in literature starting from “semblance analysis” [36] and “source scanning algorithm” [37,38]. In this paper, we use “beamforming” version of the BP method suggested for studying tectonic low-frequency earthquakes, which share many signal features with long-period volcanic earthquakes [39].

A seismic event originated in the location \vec{x}^* at the time moment t^* is recorded by a set of receivers located in \vec{r}_i ($i = 1, 2, \dots, N$) as a set of waveforms $u_i(t)$. Assuming velocity model v for a study region, we can compute theoretical travel-times $\tau(\vec{r}_i, \vec{x})$ between each receiver and some virtual source location \vec{x} . The BP technique, which general concept is schematically demonstrated in Figure 3, is based on the stacking of normalized signal envelopes shifted in accordance to these precomputed travel-times. Thus, the recorded wavefields are kinematically projected back to the point \vec{x} . We are using a bending algorithm from the Local Tomography Software (LOTOS) [40] for raytracing and calculating of travel times, which gives us the potential to improve results confidence by using a more realistic velocity model. In this study, our primary goal is the detection and only then relative location of LP seismicity, thus a simplified model with a constant velocity value equal to 2 km/s was used. For the case of Gorely, this appears to be suitable because the LP seismicity is generated at shallow depths within the volcanic edifice.

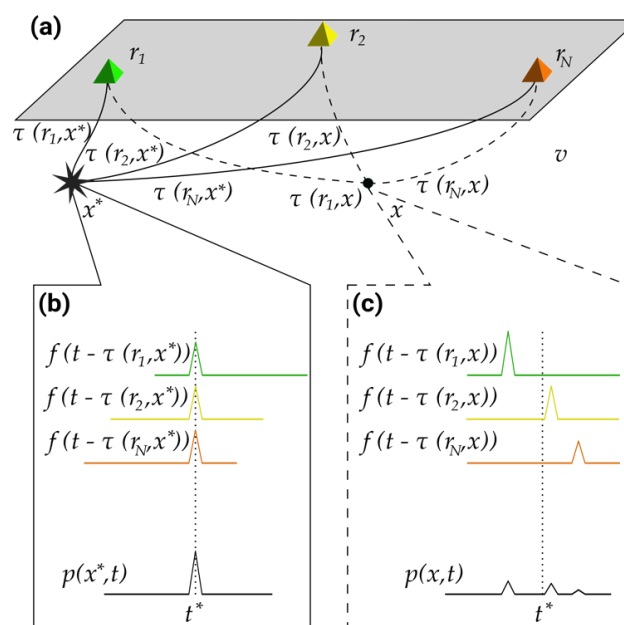


Figure 3. Back-projection general concept: (a) a simplified scheme of receivers and travel-times precomputed using ray-bending in the proper velocity model for two points of a study region; (b) back-projection to the actual location of the seismic event; (c) back-projection to the virtual source point with incorrect travel-times.

As described in the following paragraphs, for each point in the 3D space and time, we calculate a likelihood function that shows the coherency of the shifted waveforms across all receivers. Due to the small-scale media heterogeneity, the waveforms from an earthquake recorded at different stations are not coherent. That is why we ignore the signal phase and use a characteristic function (CF), $f_i(t)$, instead of raw records. Common examples of CF are high-order statistics of the seismic signal (Kurtosis, Skewness) [41], short-term average to long-term average (STA/LTA) ratio [42], and signal envelope [43]. After many trials with different types of CF, we found that in our case, the most optimal form is an energy envelope or an absolute values of seismogram smoothed in a moving window:

$$f_i(t) = \frac{1}{2h} \int_{-\tau_h}^{\tau_h} |u_i(t + \xi)| d\xi, \quad (1)$$

where $\tau_h = 3$ s is a half-size of the moving window for smoothing, and $u_i(t)$ is a horizontal component record of the i -th station.

We define back-projection intensity (BPI) function $p(\vec{x}, t)$, at point \vec{x} as a stack of CFs $f_i(t)$ normalized for geometrical spreading $A(\vec{r}_i, \vec{x})$ and shifted according to travel-times between this point and each receiver:

$$p(\vec{x}, t) = \frac{1}{N} \sum_{i=1}^N A(\vec{r}_i, \vec{x}) f_i(t - \tau(\vec{r}_i, \vec{x})), \quad (2)$$

where N is the number of used receivers. The geometrical spreading $A(\vec{r}_i, \vec{x})$ for a virtual source point \vec{x} and a receiver located in \vec{r}_i is calculated as follows:

$$A(\vec{r}_i, \vec{x}) = \frac{r_0}{d(\vec{r}_i, \vec{x})}, \quad (3)$$

where r_0 is the source size, which is approximated in our case by a unit sphere and $d(\vec{r}_i, \vec{x})$ is the length of the ray path in the reference model between the source and receiver.

For an actual source position (Figure 3b), the CFs calculated in Equation (2) are correctly shifted back in time and are stacked constructively, forming a maximum at the event's origin time. For any other points (Figure 3c), the same procedure will result in lower values of BPI. Computing BPI for a grid of virtual-source points $\vec{x}_j \in \vec{X}$ allows us to obtain an array of time-dependent functions $p(\vec{x}_j, t)$. Each of these functions represents a transformed wavefield kinematically projected back to a specific location inside the study region. They form a spatio-temporal distribution of BPI- $p(\vec{x}, t)$, which thereby may be considered as a time series of spatial images (snapshots) defined on the grid \vec{X} . Each snapshot $p(\vec{x}_j, t)$ depicts the likelihood of finding seismic source inside the study region at the specific time moment. In Figure 4, we present an example of a BPI snapshot corresponding to an average event based on the Gorely experimental data.

Incorporation of the BPI procedure inside a grid-search strategy is a core part of the BP detection technique. From full spatio-temporal BPI distribution $p(\vec{x}, t)$ we construct a compressed BPI:

$$p_c(t) = \max_{\vec{x}_j \in \vec{X}} [p(\vec{x}_j, t)], \quad (4)$$

and use it as a detecting function. By scanning through $p_c(t)$ in time for local maxima larger than a threshold value p_d , we can effectively obtain time moments t_{max} that correspond to the local maxima of the full BPI distribution. Then, we use a snapshot of BPI distribution at the t_{max} moment for estimation of source location in 3-D space. Computing the time interval τ_w between the absolute maximum to the nearest local minimum after the detected event gives us an approximate value of the signal duration. In the case illustrated in Figure 4, resulting length of the event's signal was approximately 16 s. For earthquakes located outside the study region, the snapshot maxima are usually observed on

edges of the grid. We use this criterion in conjunction with the limitation on a signal duration τ_w to exclude teleseismic and slab-related earthquakes out of the catalog.

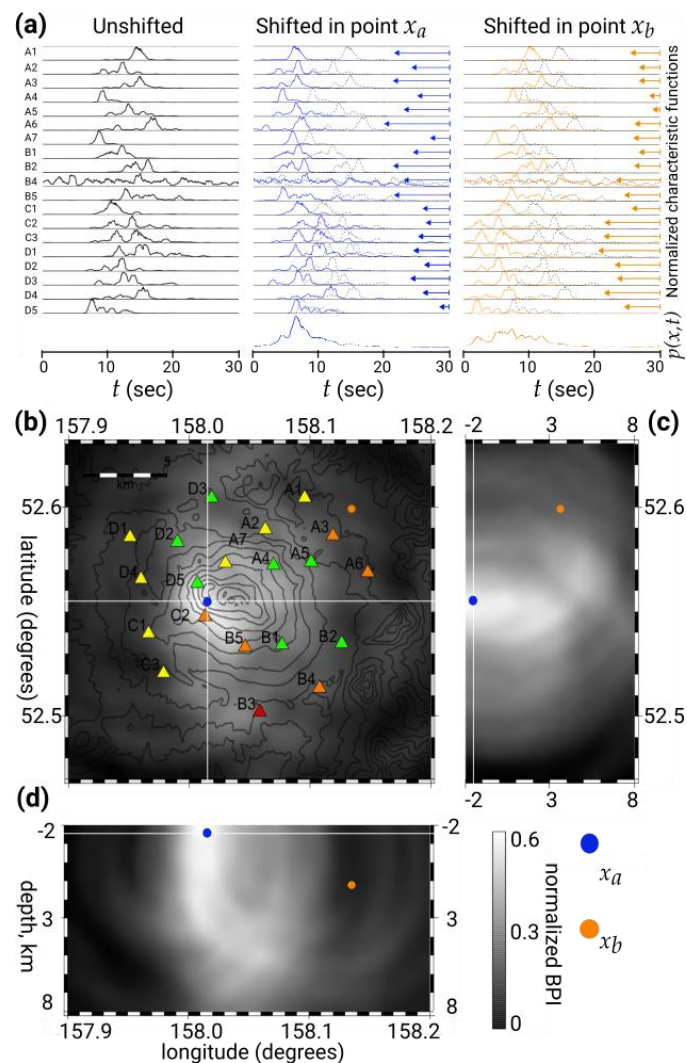


Figure 4. Example of the BP detection procedure for a high-energy LP event on Gorely: (a) signal envelopes (CFs) shifted according to precomputed travel-times; (b) horizontal, and (c,d) two vertical slices of 3-D BPI snapshot for a time of local maximum in detector function.

The BP detection technique was implemented to build a catalog of LP earthquakes beneath Gorely using two subsets of the whole data. Initially, with event detection threshold $p_d = 2 \mu\text{m/s}$, we performed detection for nine months of data available for five most consistent seismic stations (Figure 5a). This result showed that the significant of detections is condensed in the four starting months, with minor activity after middle December 2013. For this period of intense degassing, we were able to use data from 18 stations and obtain 9691 detections (Figure 5b). We then performed the BPI procedure with more conservative conditions presuming a more substantial value of the threshold equal to $4 \mu\text{m/s}$, which led to decreasing the catalog size to only 1741 most energetic events (Figure 5c). Spatial distributions of the detected events (third column in Figure 5) show that the significant part of the detected LP seismicity is located right beneath the volcano edifice. These results point out similar characteristics of seismicity in time for both low and high energy parts of the catalog. It is also apparent that after December 7th, the activity on Gorely is rapidly decaying.

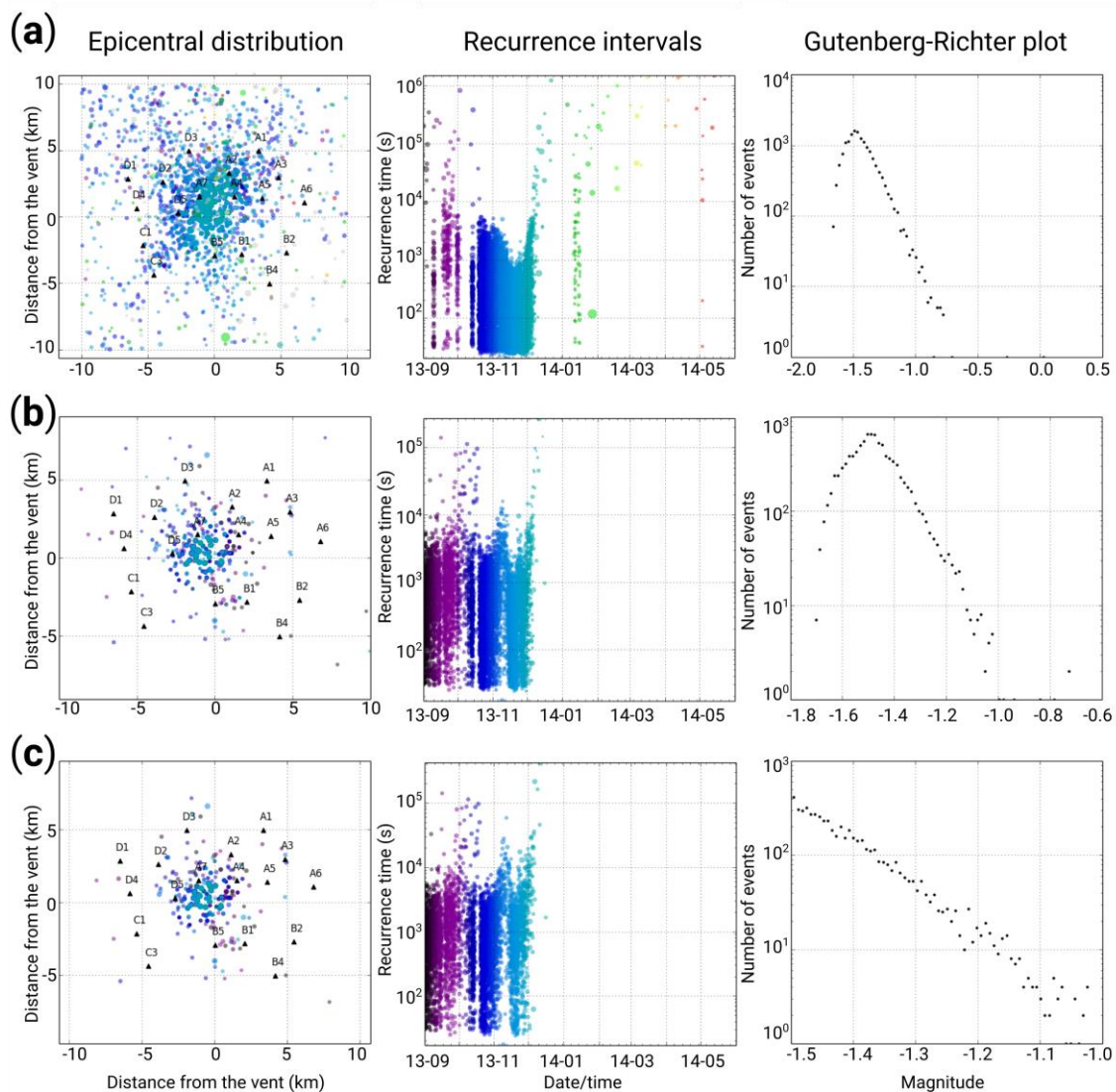


Figure 5. Results of applying the BP detection algorithm to Gorely data: (a) detections acquired using records of five temporary stations which functioned nine months; (b) same for 18 stations working during the four starting months, when degassing activity was exceptionally strong; (c) filtered detections obtained with 18 stations, which follow Gutenberg–Richter law and constitute BP-based catalog.

5. Cluster Analysis

The catalog of most-energetic events (Figure 6) derived from the implementation of the BP technique can be further investigated in detail via cluster analysis. By dividing earthquakes into groups, we can effectively reveal the overall seismicity structure that can be related to the characteristics of underlying processes. To do so, one needs a well-defined principle to group ‘similar’ earthquakes together. Our approach for similarity quantification between pairs of events, in general, resembles the one used for swarms of repeating long-period earthquakes at Shishaldin Volcano in Alaska [44].

For each pair of detected earthquakes, the corresponding waveforms of vertical components are cropped in a time window τ_w after the respective origin time ($\tau_w = 16$ s, in our case). We define the similarity of two earthquakes l and m as a correlation coefficient (CC) computed between the waveforms and mean averaged for all stations. To see the relationships between all events, one may plot these coefficients as a matrix, where each row or column reflects how similar the selected earthquake to the other ones in the catalog. Figure 7a shows the calculated CC matrix for the set of 1741 events identified for the Gorely volcano at the BP step with the higher threshold.

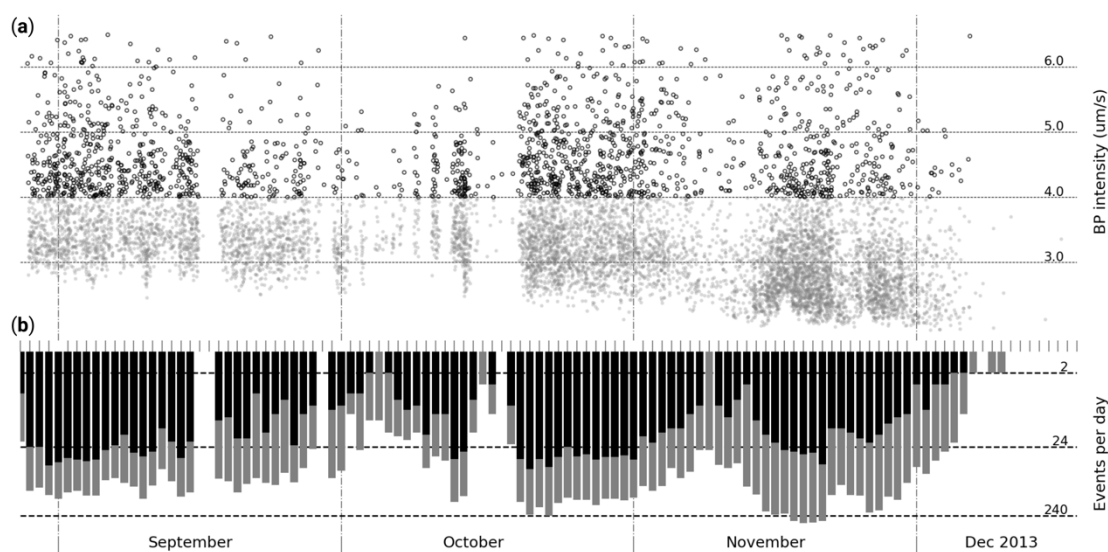


Figure 6. BP-based catalog of high-energy events (in black, correspond to Figure 4c) and indistinct detections (in grey, correspond to Figure 4b): (a) intensity and (b) daily rate of detection during the chosen period.

Despite the general similarity of all LP events in the BP-based catalog, some subgroups of events can be distinguished from the visual analysis of the CC matrix in Figure 7a. The diagonal of this matrix represents auto-correlations. We can see from four to six square patterns of high CCs along diagonal, that indicates a group of similar events localized in time. Some of the ‘squares’ are prolonged to off-diagonal part, suggesting the existence of subgroups inside. The number of groups of events with different properties can be approximately identified by estimating the rank of the CC matrix, which can be done by computing its eigenvalues. The resulted distribution of eigenvalues ranged in the decreasing order (Figure 7b) shows that only a small part of the first eigenvalues was large enough, while the rest is close to zero. We decided to take into account only five eigenvalues that are larger than 5% of the maximum one, thus estimating $N_c = 5$, the number of meaningful earthquake groups in the catalog.

Figure 7c presents the mean average CC of every detected LP earthquake with all other 1740 events in the catalog. The majority of them have the CC between 0.3 and 0.4 showing relatively high similarity of all events. At the same time, there are a few events having the correlation of around 0.1. We manually inspected all these events and identified that they are relatively short-duration VT earthquakes having completely different waveforms compared to the LP events. It does not mean that no other VT events occurred during the studied period because the used parameters of the BP method were specially adapted for searching the LP events (reference velocity, time window, frequency of filtering). Thus, after excluding these four VT events, a verified initial catalog of the LP earthquakes contained 1737 events with the highest energy.

To separate all detected LP earthquakes in five groups, we followed the iterative approach described in [45]. To find out a reasonable partition of initial clusters, we consequently excluded groups of similar earthquakes from the catalog. First, we calculate a mean average CC for every single earthquake with all other events across the whole catalog, as shown in Figure 7c. Next, an earthquake with the maximum average CC is taken as a master event for the first group. All events having the CC with the master event larger than a particular threshold h are excluded from the catalog to form the first cluster. The procedure is repeated for the rest of the catalog: on each step earthquake with maximum average correlation is taken to form the next initial cluster that is excluded from the catalog until we get all N_c clusters. After such selection, each master event is close to others in its group while staying far from the other master events. Depending on the chosen threshold, the entire catalog may be completely divided into N_c clusters, or some earthquakes may stay ungrouped. In the second step, the defined

clusters iteratively resorted in accordance with the CC matrix. On each iteration, we first check every grouped event and place it in the group where it has the highest similarity to the corresponding master event. After that, the new master event for each cluster is determined by computing a new vector of the mean similarity from a subsection of the CC matrix. As a result, stable cluster distributions are organized after several iterations. Since this method converges to a local minimum, the final result depends on the cluster's starting 'centers' (master events). Reasonable choice of the starting cluster composition via excluding them from the catalog helps us form highly diverse clusters.

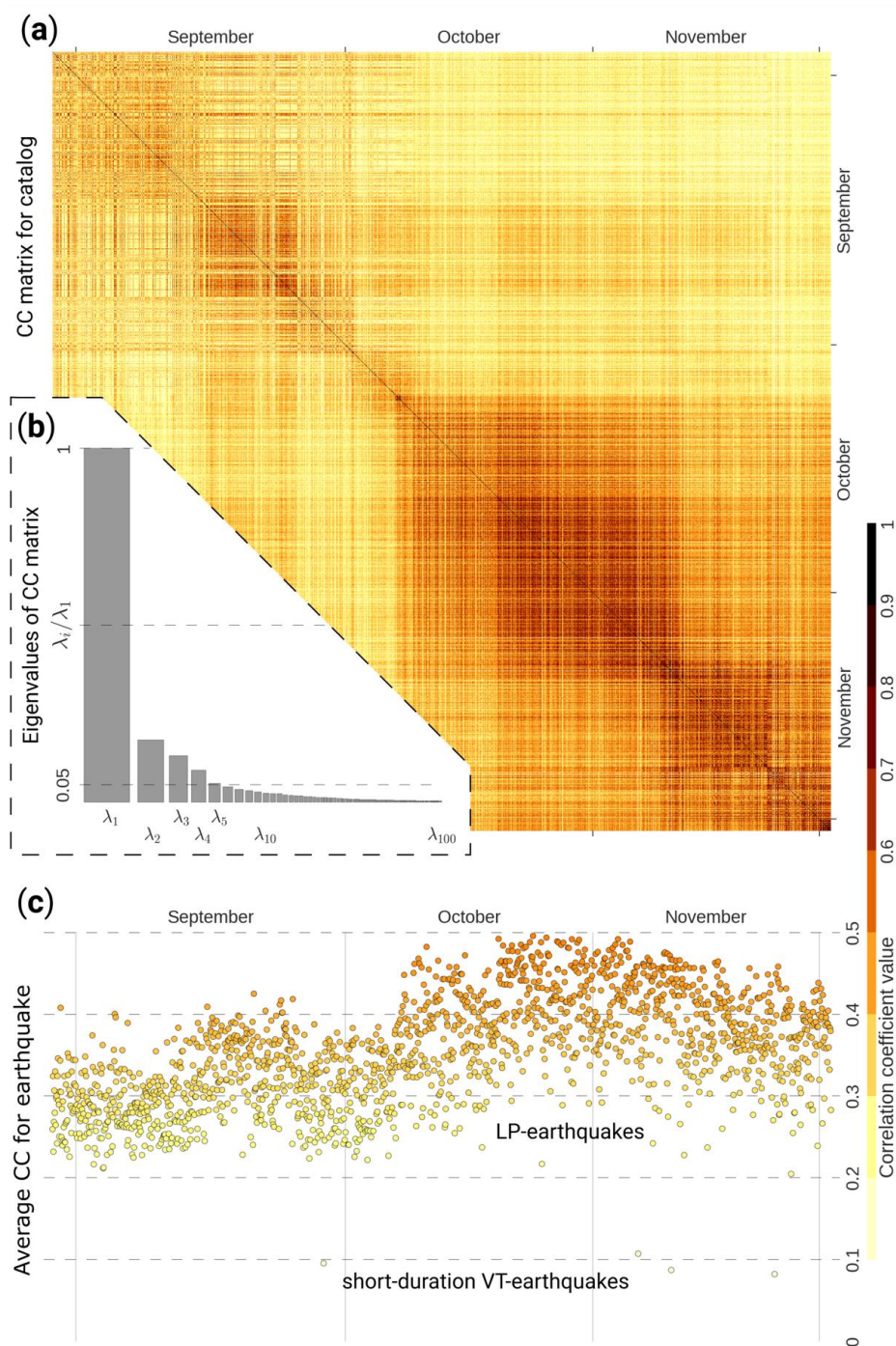


Figure 7. Similarity assessment of earthquakes from the BP based catalog: (a) waveform CC matrix; (b) first 100 eigenvalues of the matrix—sorted and normalized; (c) mean average similarity for each earthquake inside the catalog.

We performed described cluster analysis with the CC threshold of 0.3 and found that it converges to the stable distribution after the 3rd iteration. The CC values within the five groups and their time distributions are shown in Figure 8a,b. It can be seen that the CC values within distinct groups are higher than CCs with all events shown in Figure 7c, which demonstrate the adequacy of such classification of events. Final clusters are sequentially arranged in time that may indicate the possible evolution of seismic source properties or changes in the seismic velocity structure of the volcano.

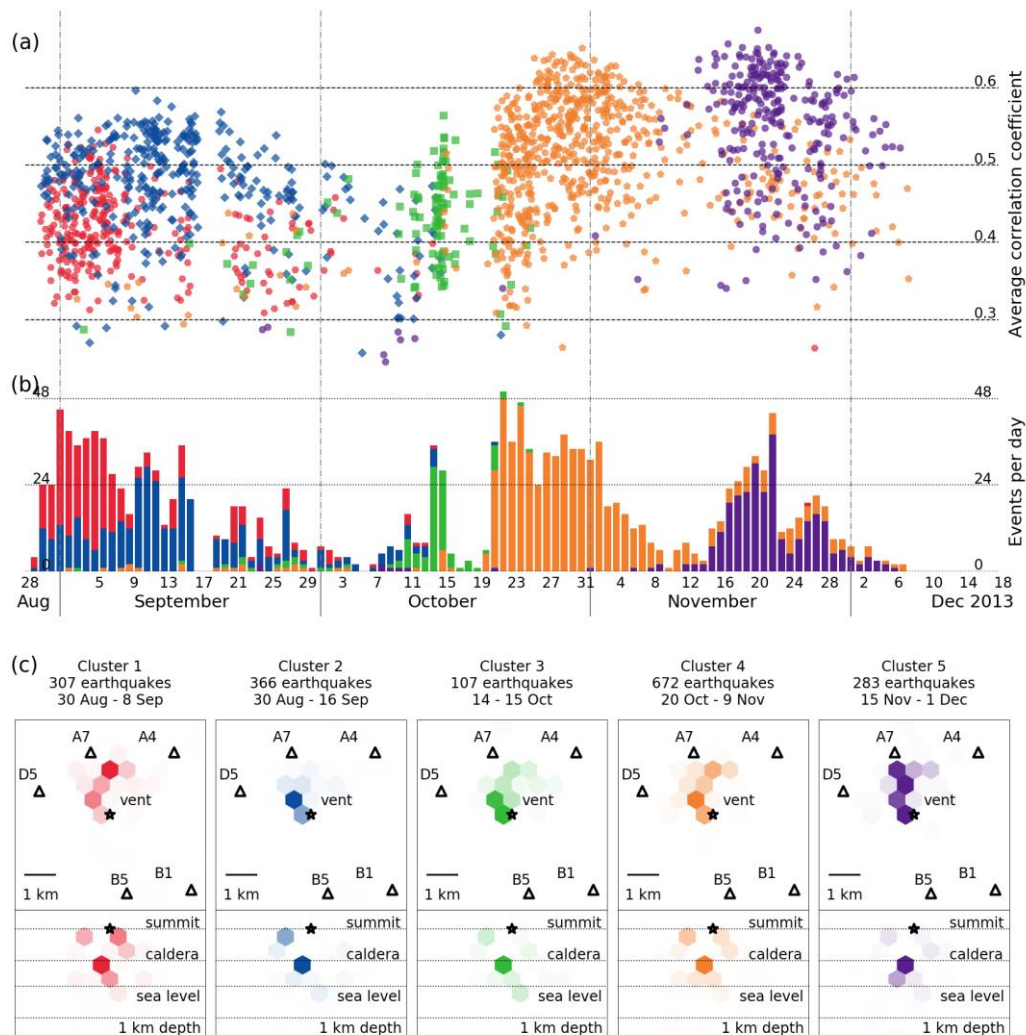


Figure 8. Cluster analysis results for BP based catalog. In all panels, the different colors indicate five identified clusters. (a) Average correlation coefficients for the final distribution after the 3rd iteration with five sequential clusters. (b) A daily number of events for different clusters. Note that each cluster has a dominant period with a maximum number of events per day. (c) Hexagonal plots of the events space distribution for each cluster projected to map view (upper row) and to vertical section oriented in west-east direction (lower row). Each hexagon presents confidence area of the location, while color intensity reflects normalized number of the events in this location.

6. Matched-Filter Detection Algorithm

The results of the cluster analysis allow us to create a set of templates that reflect common waveform features for all earthquakes in a certain group of the catalog. We create the cluster templates by stacking waveforms with the weights equal to their correlation coefficients. Thus, for the i -th receiver, the resulting template waveform $u_i^k(t)$ of the k -th cluster is computed as follow:

$$u_i^k(t) = \frac{\sum_{n=1}^{N_k} C_n^k u_i^n(t)}{\sum_{n=1}^{N_k} C_n^k}, \quad (5)$$

where $u_i^k(t)$ is a waveform of the j -th event inside the cluster, C_n^k denotes event-to-master CC, and N_k stands for the cluster size. Stacking increases signal-to-noise ratio so that we may treat the template as a fingerprint of a composite event with the common source mechanism for all events in the corresponding cluster. Since a template represents a generalized image of a cluster, we can compare it to another one visually and numerically by calculating CCs between them. In Figure 9, we show examples of the composite waveforms in some stations corresponding to the selected five groups of events.

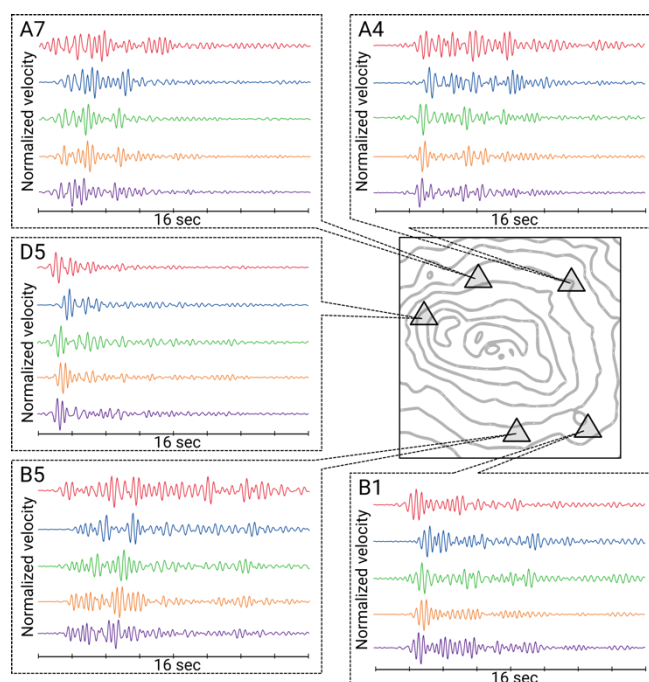


Figure 9. Template waveforms for five closest to summit stations (same colors as Figure 8).

We can use the constructed templates to search for other earthquakes, similar to ones selected for the corresponding clusters. The matched-filter (MF) search, which we use to detect multiplets [42], has become the standard way to identify families of tectonic low-frequency earthquakes [46–50] and volcanic LP earthquakes [17]. The MF algorithm consists of a matching template to continuous seismograms by computing CCs between the template and the waveforms in a sliding window. Comparing the derived time-dependent CC with a predefined threshold c_d , we can identify all events with the waveforms similar to the template, which creates a more extensive catalog than initially selected. Depending on the template-to-template similarity and chosen threshold, the same event can be detected with different templates. In these cases, we attribute such events to the template group having the highest CC. Unlike the BP technique, the MF approach is sensitive to the shape of seismic signals rather than its amplitude so that we can form a complementary catalog of weak LP-earthquakes. For the Gorely case, we were able to identify 80,615 LP earthquakes divided into five clusters. The time distributions of these events can be compared with high-energy events of the initial catalog in Figure 10.

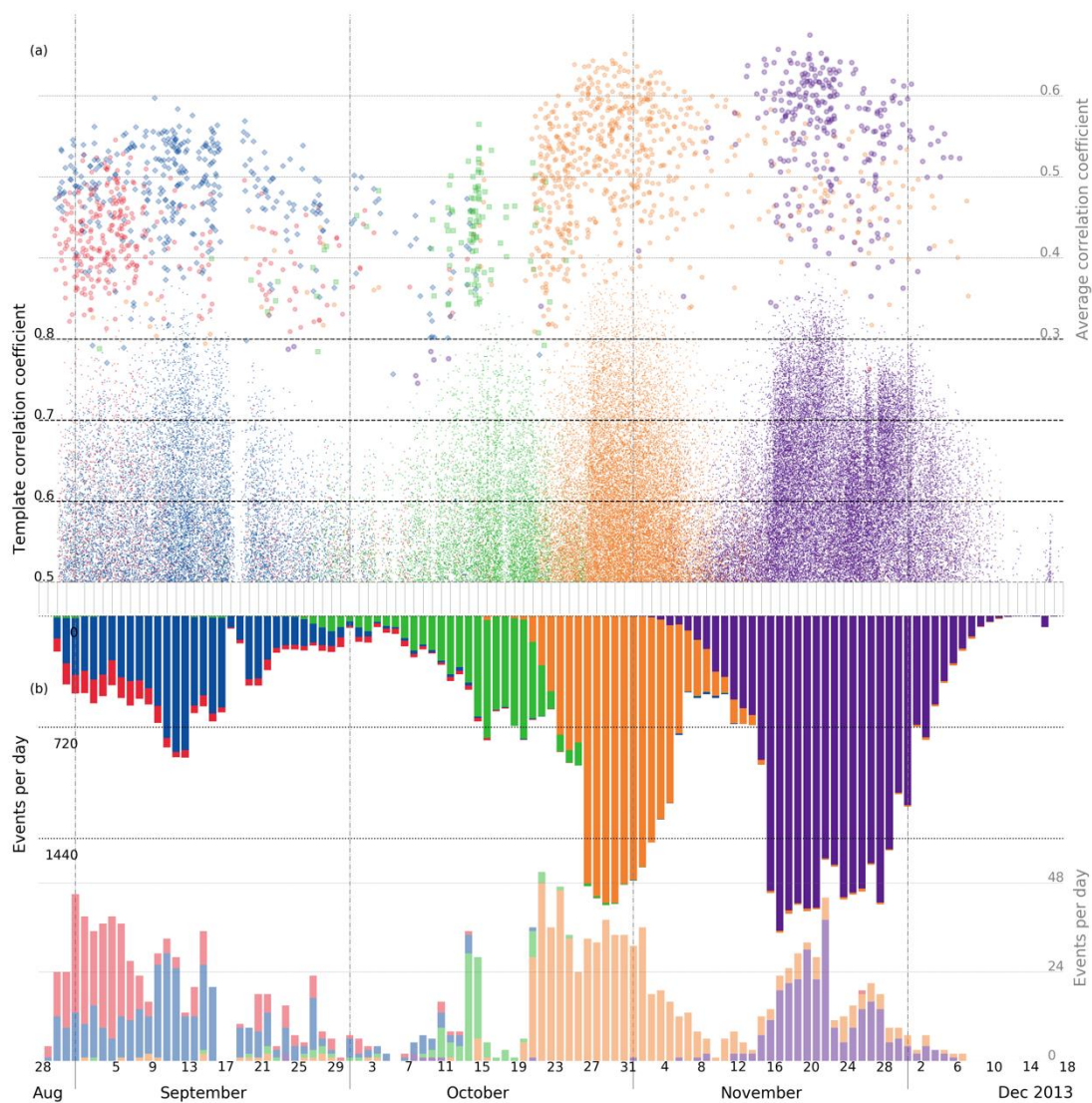


Figure 10. The MF-based catalog of lower-energy events in comparison with cluster analysis results for the BP-based catalog containing most-energetic earthquakes (in pale colors): **(a)** CCs for both catalogs (note that these are not the same type); **(b)** time distribution of the events' daily amount.

7. Discussion

Two implemented detection techniques gave us the possibility to carefully explore LP seismicity beneath Gorely volcano during a period of intense degassing. Our implementation of the BP approach is sensitive to the event energy, while the MF method is responsive to the waveform shape itself. By identifying signals of individual LP earthquakes in continuous seismic records of 18 temporary stations, we obtained the BP-based catalog containing 1737 high-energy events and the extensive MF-based list of 80,615 detections. It is important to note that the latter being complementary to the initial BP catalog is not entirely independent, as we are using templates constructed from the waveforms of identified events to obtain MF detections.

Cluster analysis of the BP-based catalog has demonstrated the limited variety and high repetitiveness of LP seismicity taking place beneath Gorely in the observation period. In total, we have identified five distinguishable families of LP earthquakes, which were sequentially arranged in time. In Figure 7, one can see the final distribution of high-energy LP earthquakes that gives us insight into the development of the conduit structure over time. At the beginning of the observation on August 28th, we see that the “red” family was dominating. By September 9th, its intensity has

incrementally decreased, as it was gradually replaced by the “blue” family, which in turn reached the maximum on September 10th and then weakened during a couple of weeks in the same manner. Between October 3rd and 7th, there is a gap in the LP seismic activity. Between October 9th and 16th, there was a short-lived peak of the “green” family activity followed by another gap on October 16–18. On October 20th, the “orange” family abruptly started and produced the largest group of the LP events, which gradually increased until November 9th. After another short gap, the last “violet” family started on November 13th, reached its peak on November 22nd, and then completely decayed to December 6th. After this moment, LP activity only occurred infrequently.

The extensive MF-based catalog provides additional information about the evolution of Gorely's degassing system. As one may see in Figure 10, lower-energy events are repeating the same pattern as their high-energy counterpart. However, there are fewer gaps in the activity, and the transitions between LP earthquake families are much smoother. Other differences are the domination of the “blue” family over the “red” one, considerably prolonged duration of the “green” period and the minor burst of detections on December 16th.

Each LP earthquake family produced a series of nearly similar signals emitted from a localized source region. These source regions were located beneath the volcano summit at depths of less than 1 km below the surface. In the recent tomography study of Gorely [21], the top of the prominent anomaly, representing the magma chamber, was located at ~2.5 km below the surface. The interface between very high Vp/Vs in the magma chamber and low Vp/Vs in the overlying carapace is interpreted as a level of the phase transition in the molten magma. We suppose that dissolved fluids were degassing at this stage due to lower pressure in the shallower part of the magma reservoir. The LP earthquakes identified in our study may indicate the following pathway of ascending high-pressure gases. The rapid degassing and fast dynamic propagation of gas bubbles through the conduit root may lead to self-sustained oscillations within the magmatic channel [51], generating the LP radiation recorded by seismic stations. It is possible that at some moment, the conduit structure changes, resulting in new oscillation parameters and characteristics of repeated LP events. Therefore, the observed evolution of LP earthquakes may reflect the structural changes in the shallow part of the volcano-magmatic system.

Alternatively, given generally shallow levels of LP radiation on Gorely, groundwaters may be involved in two-phase ‘steam and water’ resonator system in a similar way that was proposed for Ngauruhoe volcano in New Zealand [52,53]. The climate of Kamchatka with a heavy snow cover of volcanoes over a half-year and the glaciation of Pra-Gorely caldera both support this version. However, the chemical content of the and the rate of Gorely degassing implies that the proposed ‘bubble-dynamic’ mechanism of LP is primarily caused by dissolving magmatic fluids in the conduit root.

We see that only at the beginning of the observation period, two of LP earthquake families (the “red” and “blue” one) functioned at the same moments with about similar intensity of the high-energy events. In other periods, only a sole family is dominating at the time, which is apparent in the MF-based detection distribution (Figure 10). It probably means that the preferable degassing regime of Gorely requires only one conduit acting at a time. Smooth transitions in the number of detected events between families (Figure 10) and the structure of CC matrix (Figure 7a) imply that each dominant family gradually evolves into the next one. This may be interpreted as the slow migration of the source along a constricted pathway of magmatic gasses ascent. Close likelihood of template waveforms for master events of “blue”, “green”, “orange”, and “purple” families also support this point, while “red” one represents alternative explanation. The co-existence of two LP families acting in the same period (but not simultaneously) may be interpreted as the balancing stage of the gas ascent process. In such conditions, the pressure gradient allows only a portion of gas bubbles to overcome constriction in the “blue” family origin point, while the rest of the gasses have to proceed laterally (Figure 8c) to the “red” family origin point.

Author Contributions: I.K. and N.S. designed the field experiment; I.A. and S.A. performed the field experiment; S.A. analyzed the data; N.M.S. and I.K. contributed to interpretation of the results. All authors participated in discussions of the results and contributed in writing the manuscript and preparing figures. All authors have read and agreed to the published version of the manuscript.

Funding: This study was supported by the Russian Ministry of Education and Science (grant #14.W03.31.0033), and by the European Research Council (ERC) under the European Union Horizon 2020 Research and Innovation Programme (grant agreement 787399-SEISMAZE). I.K. is supported by the Russian Foundation for Basic Research Grant #18-55-52003.

Acknowledgments: We are grateful to William Frank, Natalia Poiata, and Jean Soubestre for the valuable discussions about methods used in this study. We also thank the field experiment team members: Andrey Jakovlev, Pavel Kuznetsov, Evgeny Deev, Arseny Ivanov, and Alejandro Diaz-Moreno, who helped during installation of the temporary seismic network. We also appreciate the support of KBGS staff, who contributed to the operation of the permanent seismic network in Kamchatka. We thank Geneviève Moguilny for the attentive assistance during numerical computations which were partly performed on the S-CAPAD platform, IPGP, France. Finally, we acknowledge anonymous reviewers for their valuable comments that not only improved this manuscript but also pointed out some prospective directions for future work.

Conflicts of Interest: The authors declare no conflict of interest.

References

1. Chouet, B.A.; Matoza, R.S. A multi-decadal view of seismic methods for detecting precursors of magma movement and eruption. *J. Volcanol. Geotherm. Res.* **2013**, *252*, 108–175. [\[CrossRef\]](#)
2. Lahr, J.C.; Chouet, B.A.; Stephens, C.D.; Power, J.A.; Page, R.A. Earthquake classification, location, and error analysis in a volcanic environment: Implications for the magmatic system of the 1989–1990 eruptions at Redoubt volcano, Alaska. *J. Volcanol. Geotherm. Res.* **1994**, *62*, 137–151. [\[CrossRef\]](#)
3. Roman, D.C.; Cashman, K.V. The origin of volcano-tectonic earthquake swarms. *Geology* **2006**, *34*, 457. [\[CrossRef\]](#)
4. Minakami, T. Study of eruptions and earthquakes originating from volcanoes (Part 1 of 3). *Int. Geol. Rev.* **1961**, *3*, 712–719. [\[CrossRef\]](#)
5. Minakami, T. Seismology of volcanoes in Japan. In *Developments in Solid Earth Geophysics*; Elsevier: Amsterdam, The Netherlands, 1974; Volume 6, pp. 1–27.
6. Zobin, V. *Introduction to Volcanic Seismology*; Elsevier: Amsterdam, The Netherlands, 2012; ISBN 9780444563750.
7. Chouet, B.A. Long-period volcano seismicity: Its source and use in eruption forecasting. *Nature* **1996**, *380*, 309–316. [\[CrossRef\]](#)
8. Kumagai, H.; Chouet, B.A. Acoustic properties of a crack containing magmatic or hydrothermal fluids. *J. Geophys. Res. Solid Earth* **2000**, *105*, 25493–25512. [\[CrossRef\]](#)
9. Iverson, R.M.; Dzurisin, D.; Gardner, C.A.; Gerlach, T.M.; LaHusen, R.G.; Lisowski, M.; Major, J.J.; Malone, S.D.; Messerich, J.A.; Moran, S.C.; et al. Dynamics of seismogenic volcanic extrusion at Mount St Helens in 2004–05. *Nature* **2006**, *444*, 439–443. [\[CrossRef\]](#) [\[PubMed\]](#)
10. Kendrick, J.E.; Lavallée, Y.; Hirose, T.; Di Toro, G.; Hornby, A.J.; De Angelis, S.; Dingwell, D.B. Volcanic drumbeat seismicity caused by stick-slip motion and magmatic frictional melting. *Nat. Geosci.* **2014**, *7*, 438–442. [\[CrossRef\]](#)
11. Matoza, R.S.; Chouet, B.A.; Dawson, P.B.; Shearer, P.M.; Haney, M.M.; Waite, G.P.; Moran, S.C.; Mikesell, T.D. Source mechanism of small long-period events at Mount St. Helens in July 2005 using template matching, phase-weighted stacking, and full-waveform inversion. *J. Geophys. Res. Solid Earth* **2015**, *120*, 6351–6364. [\[CrossRef\]](#)
12. Battaglia, J. Location of long-period events below Kilauea Volcano using seismic amplitudes and accurate relative relocation. *J. Geophys. Res.* **2003**, *108*, 2553. [\[CrossRef\]](#)
13. Rowe, C.; Thurber, C.; White, R. Dome growth behavior at Soufriere Hills Volcano, Montserrat, revealed by relocation of volcanic event swarms, 1995–1996. *J. Volcanol. Geotherm. Res.* **2004**, *134*, 199–221. [\[CrossRef\]](#)
14. Gambino, S. High precision locations of LP events on Mt. Etna: Reconstruction of the fluid-filled volume. *Stud. Geophys. Geod.* **2006**, *50*, 663–674. [\[CrossRef\]](#)
15. Green, D.N.; Neuberg, J. Waveform classification of volcanic low-frequency earthquake swarms and its implication at Soufrière Hills Volcano, Montserrat. *J. Volcanol. Geotherm. Res.* **2006**, *153*, 51–63. [\[CrossRef\]](#)

16. Gambino, S.; Cammarata, L.; Rapisarda, S. High precision locations of long-period events at La Fossa Crater (Vulcano Island, Italy). *Ann. Geophys.* **2009**, *52*, 137–147. [\[CrossRef\]](#)
17. Shapiro, N.M.; Droznin, D.V.; Droznina, S.Y.; Senyukov, S.L.; Gusev, A.A.; Gordeev, E.I. Deep and shallow long-period volcanic seismicity linked by fluid-pressure transfer. *Nat. Geosci.* **2017**, *10*, 442–445. [\[CrossRef\]](#)
18. Hurst, T.; Jolly, A.D.; Sherburn, S. Precursory characteristics of the seismicity before the 6 August 2012 eruption of Tongariro volcano, North Island, New Zealand. *J. Volcanol. Geotherm. Res.* **2014**, *286*, 294–302. [\[CrossRef\]](#)
19. Battaglia, J.; Métaxian, J.-P.; Garaebiti, E. Short term precursors of Strombolian explosions at Yasur volcano (Vanuatu). *Geophys. Res. Lett.* **2016**, *43*, 1960–1965. [\[CrossRef\]](#)
20. Chebrov, V.N.; Droznin, D.V.; Kugaenko, Y.A.; Levina, V.I.; Senyukov, S.L.; Sergeev, V.A.; Shevchenko, Y.V.; Yashchuk, V.V. The system of detailed seismological observations in Kamchatka in 2011. *J. Volcanol. Seismol.* **2013**, *7*, 16–36. [\[CrossRef\]](#)
21. Kuznetsov, P.; Koulakov, I.; Jakovlev, A.; Abkadyrov, I.; Deev, E.; Gordeev, E.I.; Senyukov, S.L.; El Khrepy, S.; Al Arifi, N. Structure of Volatile Conduits beneath Gorely Volcano (Kamchatka) Revealed by Local Earthquake Tomography. *Geosciences* **2017**, *7*, 111. [\[CrossRef\]](#)
22. Koulakov, I.Y.U.; Dobretsov, N.L.; Bushenkova, N.A.; Yakovlev, A.V. Slab shape in subduction zones beneath the Kurile-Kamchatka and Aleutian arcs based on regional tomography results. *Russ. Geol. Geophys.* **2011**, *52*, 650–667. [\[CrossRef\]](#)
23. Gavrilenko, M.G.; Ozerov, A.Y.; Kyle, P.R.; Carr, M.J.; Nikulin, A.; Vidito, C.; Danyushevsky, L. Abrupt transition from fractional crystallization to magma mixing at Gorely volcano (Kamchatka) after caldera collapse. *Bull. Volcanol.* **2016**, *78*, 47. [\[CrossRef\]](#)
24. Kirsanov, I.T.; Melekestsev, I.V. Gorely Volcano. In *Active Volcanoes of Kamchatka*; Fedotov, S.A., Ed.; Nauka: Moscow, Russia, 1991; pp. 294–315.
25. Selyangin, O.B.; Ponomareva, V.V. Gorelovsky Volcanic Center, Southern Kamchatka: Structure and Evolution. *J. Volcanol. Seismol.* **1999**, *2*, 3–23.
26. Tolstykh, M.L.; Naumov, V.B.; Gavrilenko, M.G.; Ozerov, A.Y.; Kononkova, N.N. Chemical composition, volatile components, and trace elements in the melts of the Gorely volcanic center, southern Kamchatka: Evidence from inclusions in minerals. *Geochem. Int.* **2012**, *50*, 522–550. [\[CrossRef\]](#)
27. Bindeman, I.N.; Leonov, V.L.; Izbekov, P.E.; Ponomareva, V.V.; Watts, K.E.; Shipley, N.K.; Perepelov, A.B.; Bazanova, L.I.; Jicha, B.R.; Singer, B.S.; et al. Large-volume silicic volcanism in Kamchatka: Ar–Ar and U–Pb ages, isotopic, and geochemical characteristics of major pre-Holocene caldera-forming eruptions. *J. Volcanol. Geotherm. Res.* **2010**, *189*, 57–80. [\[CrossRef\]](#)
28. Seligman, A.; Bindeman, I.; Jicha, B.; Ellis, B.; Ponomareva, V.; Leonov, V. Multi-Cyclic and Isotopically Diverse Silicic Magma Generation in an Arc Volcano: Gorely Eruptive Center, Kamchatka, Russia. *J. Petrol.* **2014**, *55*, 1561–1594. [\[CrossRef\]](#)
29. Gusev, A.A.; Ponomareva, V.V.; Braitseva, O.A.; Melekestsev, I.V.; Sulerzhitsky, L.D. Great explosive eruptions on Kamchatka during the last 10,000 years: Self-similar irregularity of the output of volcanic products. *J. Geophys. Res. Solid Earth* **2003**, *108*. [\[CrossRef\]](#)
30. Kirianov, V.Y. Volcanic ash in Kamchatka as a source of potential hazard to air traffic. In *Volcanic Ash and Aviation Safety: Proceedings of the First International Symposium on Volcanic Ash and Aviation Safety*; Casadevall, T.J., Ed.; U.S. Geological Survey: Reston, VA, USA, 1994.
31. Kirsanov, I.T.; Fedorov, M.V. Ignimbrites of Gorely volcano. In *Proceedings of the Problems of Volcanism. II USSR Volcanological Meeting, Petropavlovsk-Kamchatsky, Russia, 12 November 1964*; pp. 45–47.
32. Kirsanov, I.T. Gorely volcano, its geological structure, the last eruptions, and composition of the products. *Volcan. Act. Its Mech. Relat. Geodyn. Predict. Erupt. Earthq.* **1985**, *1*, 32–43.
33. Melekestsev, I.V.; Braitseva, O.A.; Ponomareva, V.V. Activity dynamics of Mutnovsky and Gorely volcanos in Golocene and volcanic dangerous for surrounding regions. *Volcanol. Seismol.* **1987**, *3*, 3–18.
34. Aiuppa, A.; Giudice, G.; Liuzzo, M.; Tamburello, G.; Allard, P.; Calabrese, S.; Chaplygin, I.; McGonigle, A.J.S.; Taran, Y. First volatile inventory for Gorely volcano, Kamchatka. *Geophys. Res. Lett.* **2012**, *39*. [\[CrossRef\]](#)
35. Sobolevskaya, O.V. Seismicity of Gorely volcano 1984–2009. In *Proceedings of the Regional Conference at KB GS RAS, Petropavlovsk-Kamchatsky, Russia, 11–17 October 2009*; pp. 382–386.
36. Tchegotareva, I.I.; Nikolaev, A.V.; Sato, H. Seismic emission activity of Earth's crust in Northern Kanto, Japan. *Phys. Earth Planet. Inter.* **2000**, *120*, 167–182. [\[CrossRef\]](#)

37. Kao, H.; Shan, S.-J. The Source-Scanning Algorithm: Mapping the distribution of seismic sources in time and space. *Geophys. J. Int.* **2004**, *157*, 589–594. [[CrossRef](#)]
38. Kao, H.; Shan, S.-J. Rapid identification of earthquake rupture plane using Source-Scanning Algorithm. *Geophys. J. Int.* **2007**, *168*, 1011–1020. [[CrossRef](#)]
39. Frank, W.B.; Shapiro, N.M. Automatic detection of low-frequency earthquakes (LFEs) based on a beamformed network response. *Geophys. J. Int.* **2014**, *197*, 1215–1223. [[CrossRef](#)]
40. Koulakov, I. LOTOS Code for Local Earthquake Tomographic Inversion: Benchmarks for Testing Tomographic Algorithms. *Bull. Seismol. Soc. Am.* **2009**, *99*, 194–214. [[CrossRef](#)]
41. Langet, N.; Maggi, A.; Michelini, A.; Brenguier, F. Continuous Kurtosis-Based Migration for Seismic Event Detection and Location, with Application to Piton de la Fournaise Volcano, La Reunion. *Bull. Seismol. Soc. Am.* **2014**, *104*, 229–246. [[CrossRef](#)]
42. Gibbons, S.J.; Ringdal, F. The detection of low magnitude seismic events using array-based waveform correlation. *Geophys. J. Int.* **2006**, *165*, 149–166. [[CrossRef](#)]
43. Poiata, N.; Satriano, C.; Vilotte, J.-P.; Bernard, P.; Obara, K. Multiband array detection and location of seismic sources recorded by dense seismic networks. *Geophys. J. Int.* **2016**, *205*, 1548–1573. [[CrossRef](#)]
44. Petersen, T. Swarms of repeating long-period earthquakes at Shishaldin Volcano, Alaska, 2001–2004. *J. Volcanol. Geotherm. Res.* **2007**, *166*, 177–192. [[CrossRef](#)]
45. Soubestre, J.; Shapiro, N.M.; Seydoux, L.; de Rosny, J.; Droznin, D.V.; Droznina, S.Y.; Senyukov, S.L.; Gordeev, E.I. Network-Based Detection and Classification of Seismovolcanic Tremors: Example From the Klyuchevskoy Volcanic Group in Kamchatka. *J. Geophys. Res. Solid Earth* **2018**, *123*, 564–582. [[CrossRef](#)]
46. Shelly, D.R.; Beroza, G.C.; Ide, S.; Nakamura, S. Low-frequency earthquakes in Shikoku, Japan, and their relationship to episodic tremor and slip. *Nature* **2006**, *442*, 188–191. [[CrossRef](#)]
47. Shelly, D.R. Possible deep fault slip preceding the 2004 Parkfield earthquake, inferred from detailed observations of tectonic tremor. *Geophys. Res. Lett.* **2009**, *36*, L17318. [[CrossRef](#)]
48. Bostock, M.G.; Royer, A.A.; Hearn, E.H.; Peacock, S.M. Low frequency earthquakes below southern Vancouver Island. *Geochem. Geophys. Geosyst.* **2012**, *13*. [[CrossRef](#)]
49. Frank, W.B.; Shapiro, N.M.; Kostoglodov, V.; Husker, A.L.; Campillo, M.; Payero, J.S.; Prieto, G.A. Low-frequency earthquakes in the Mexican Sweet Spot. *Geophys. Res. Lett.* **2013**, *40*, 2661–2666. [[CrossRef](#)]
50. Frank, W.B.; Shapiro, N.M.; Husker, A.L.; Kostoglodov, V.; Romanenko, A.; Campillo, M. Using systematically characterized low-frequency earthquakes as a fault probe in Guerrero, Mexico. *J. Geophys. Res. Solid Earth* **2014**, *119*, 7686–7700. [[CrossRef](#)]
51. Julian, B.R. Volcanic tremor: Nonlinear excitation by fluid flow. *J. Geophys. Res. Solid Earth* **1994**, *99*, 11859–11877. [[CrossRef](#)]
52. Jolly, A.D.; Neuberg, J.; Jousset, P.; Sherburn, S. A new source process for evolving repetitious earthquakes at Ngauruhoe volcano, New Zealand. *J. Volcanol. Geotherm. Res.* **2012**, *215–216*, 26–39. [[CrossRef](#)]
53. Park, I.; Jolly, A.; Kim, K.Y.; Kennedy, B. Temporal variations of repeating low frequency volcanic earthquakes at Ngauruhoe Volcano, New Zealand. *J. Volcanol. Geotherm. Res.* **2019**, *373*, 108–119. [[CrossRef](#)]

